

MRI safety of implants

Citation for published version (APA):

Stijnman, P. R. S. (2022). *MRI safety of implants: measurement and model-based tools for validation and calculation of RF field interactions*. [Phd Thesis 1 (Research TU/e / Graduation TU/e), Biomedical Engineering]. Eindhoven University of Technology.

Document status and date:

Published: 30/06/2022

Document Version:

Publisher's PDF, also known as Version of Record (includes final page, issue and volume numbers)

Please check the document version of this publication:

- A submitted manuscript is the version of the article upon submission and before peer-review. There can be important differences between the submitted version and the official published version of record. People interested in the research are advised to contact the author for the final version of the publication, or visit the DOI to the publisher's website.
- The final author version and the galley proof are versions of the publication after peer review.
- The final published version features the final layout of the paper including the volume, issue and page numbers.

[Link to publication](#)

General rights

Copyright and moral rights for the publications made accessible in the public portal are retained by the authors and/or other copyright owners and it is a condition of accessing publications that users recognise and abide by the legal requirements associated with these rights.

- Users may download and print one copy of any publication from the public portal for the purpose of private study or research.
- You may not further distribute the material or use it for any profit-making activity or commercial gain
- You may freely distribute the URL identifying the publication in the public portal.

If the publication is distributed under the terms of Article 25fa of the Dutch Copyright Act, indicated by the "Taverne" license above, please follow below link for the End User Agreement:

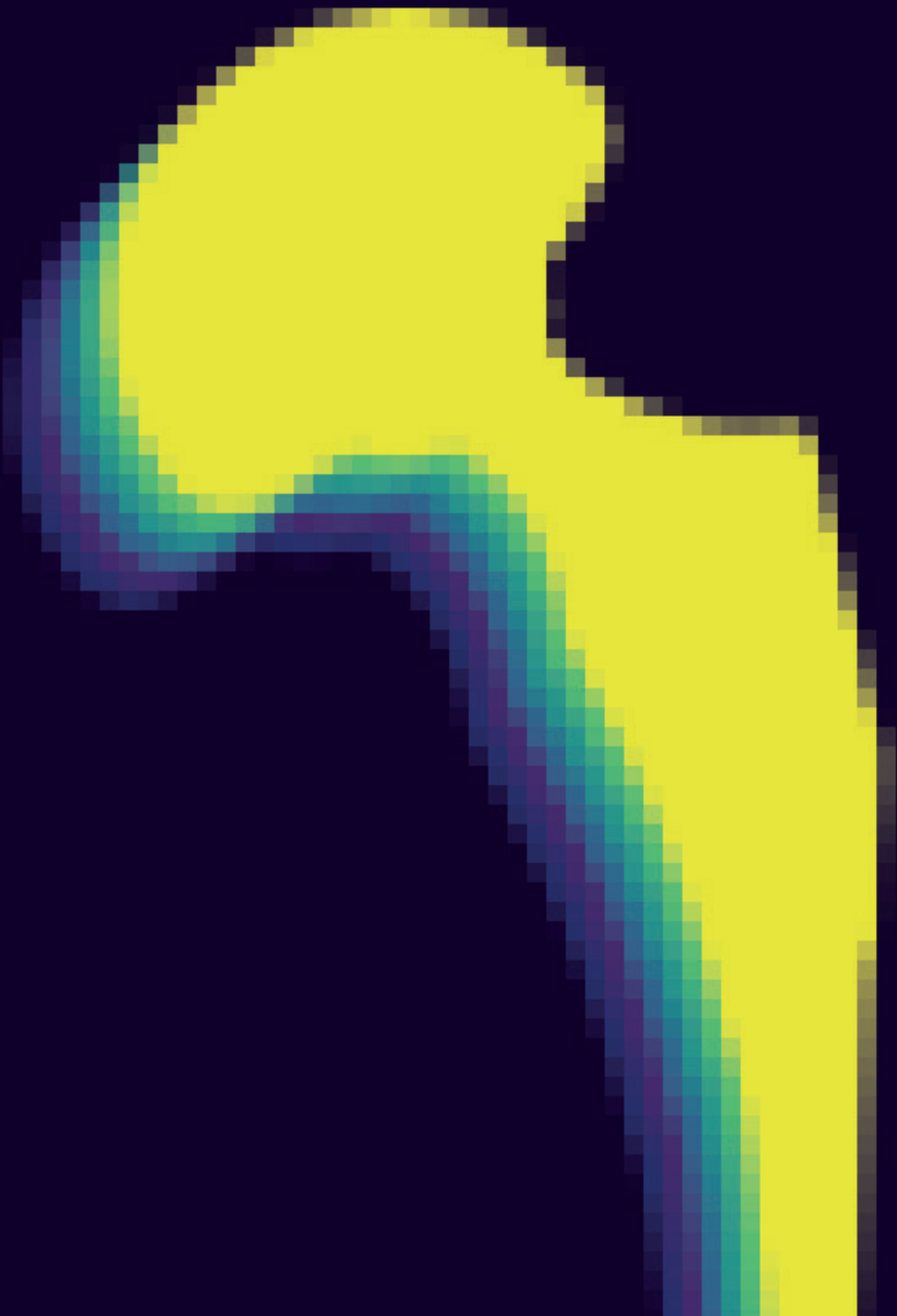
www.tue.nl/taverne

Take down policy

If you believe that this document breaches copyright please contact us at:

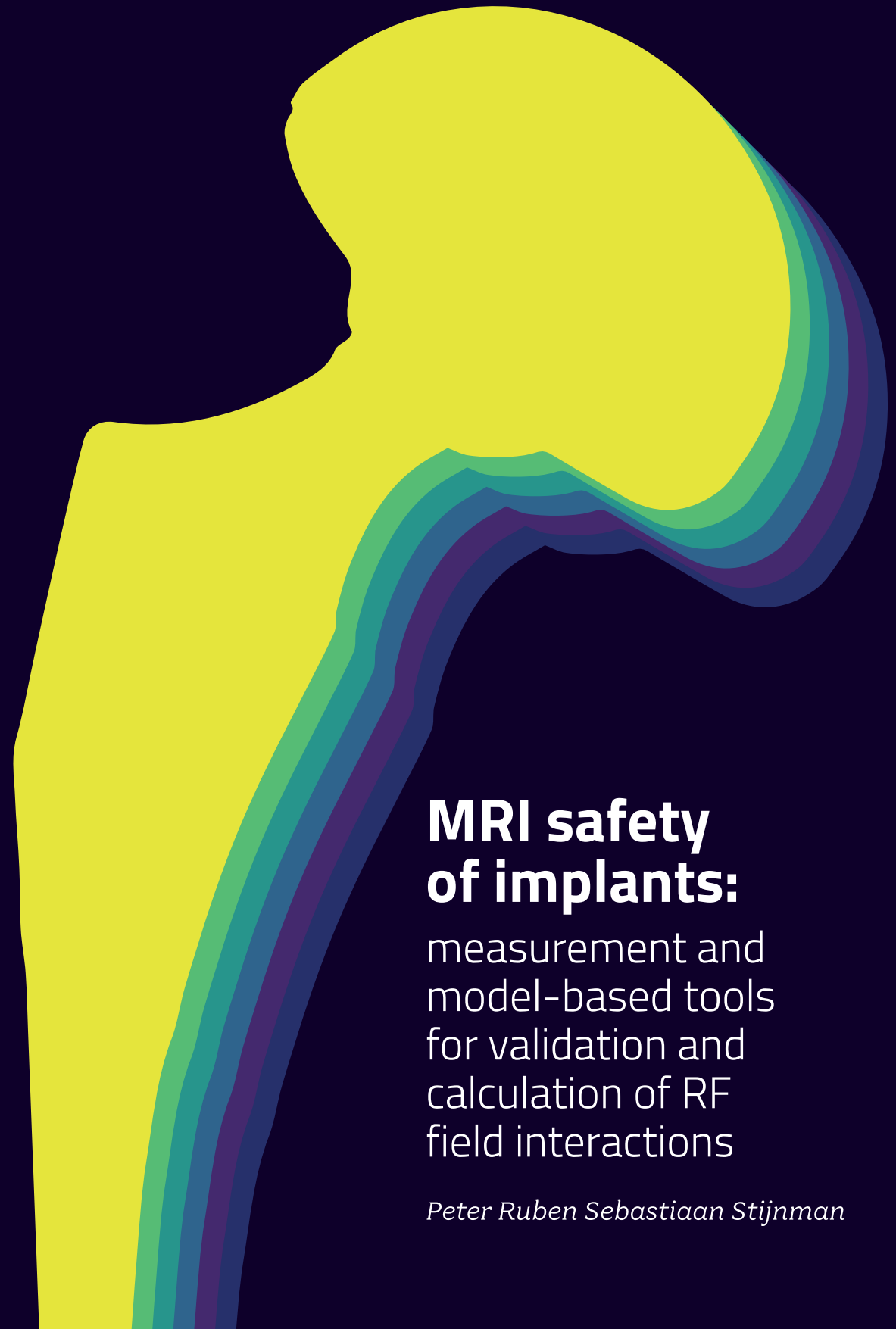
openaccess@tue.nl

providing details and we will investigate your claim.



MRI safety of implants: measurement and model-based tools for validation and calculation of RF field interactions

P.R.S. Stijnen



**MRI safety
of implants:**
measurement and
model-based tools
for validation and
calculation of RF
field interactions

Peter Ruben Sebastiaan Stijnen

MRI safety of implants: measurement and
model-based tools for validation and calculation
of RF field interactions

Peter Ruben Sebastiaan Stijnman

Cover design: Eva Stijnman

MRI safety of implants: measurement and model-based tools for validation and calculation of RF field interactions

PhD Thesis, Eindhoven University of Technology, The Netherlands

Manuscript

Layout: P.R.S. Stijnman
Typeset in: L^AT_EX
Printed by: Ridderprint
ISBN: 978-90-386-5526-0

Copyright

©Peter Ruben Sebastiaan Stijnman
©John Wiley & sons (Chapters 2, 3 and 6)
©Springer Nature (Chapter 4)

Funding

This work is part of the research programme "Safety threat or measurement device? Using the MRI scanner to assess RF safety of implanted medical devices" in MRI with project number 15739, which is (partly) financed by the Netherlands Organisation for Scientific Research (NWO).

MRI safety of implants: measurement and model-based tools for validation and calculation of RF field interactions

PROEFSCHRIFT

ter verkrijging van de graad van doctor aan de Technische Universiteit Eindhoven, op gezag van de rector magnificus prof.dr.ir. F.P.T. Baaijens, voor een commissie aangewezen door het College voor Promoties, in het openbaar te verdedigen op 30 juni 2022 om 16:00 uur.

door:
Peter Ruben Sebastiaan Stijnman
Geboren te Arnhem

Dit proefschrift is goedgekeurd door de promotoren en de samenstelling van de promotiecommissie is als volgt:

Voorzitter:	Prof.dr. M. Merkx	
Promotoren:	Prof.dr. J.P.W. Pluim	
	Prof.dr.ir. C.A.T. van den Berg	(Universitair Medisch Centrum Utrecht)
Copromotor:	Dr.ir. A.J.E. Raaijmakers	
Promotiecommissieleden:	Prof.dr. J.P.W. Pluim	
	Prof.dr.ir. C.A.T. van den Berg	(Universitair Medisch Centrum Utrecht)
	Dr.ir. A.J.E. Raaijmakers	
	Prof.dr. B.W. Raaymakers	(Universitair Medisch Centrum Utrecht)
	Prof.dr. A.G. Webb	(Leids Universitair Medisch Centrum)
	Prof.dr.ir. M.C. van Beurden	
	Dr.ir. R.F. Remis	(Technische Universiteit Delft)

Het onderzoek dat in dit proefschrift wordt beschreven is uitgevoerd in overeenstemming met de TU/e Gedragscode Wetenschapsbeoefening.

Contents

1	General introduction	1
1.1	Magnetic fields in MRI	2
1.2	Safety concerns	2
1.3	Safety assessment	3
1.3.1	Tier-based RF safety assessment	4
1.4	Thesis outline	6
2	A Single Setup Approach for the MRI-based Measurement and Validation of the Transfer Function of Elongated Medical Implants	9
2.1	Introduction	11
2.2	Methods	13
2.2.1	Simulation based investigation of potential validation methods	13
2.2.2	Validation Quality	15
2.2.3	Proof-of-principle validation study using the best performing MRI-setup validation method	16
2.2.4	MRI-based transfer function measurement	16
2.2.5	Transfer function simulation	18
2.2.6	Validation Method	18
2.2.7	Validation Measurement	19
2.2.8	Uncertainty analysis	19
2.3	Results	21
2.3.1	Simulation based investigation of potential validation methods	21
2.3.2	Proof-of-principle validation study using best performing MRI-setup validation method	24
2.4	Discussion	27
2.5	Conclusion	31
2.6	Acknowledgements	31
2.7	Supporting Figures	32

3	Accelerating Implant RF Safety Assessment Using a Low-Rank Inverse Update Method	35
3.1	Introduction	37
3.2	Theory	39
3.3	Methods	43
3.4	Results	45
3.5	Discussion	47
3.6	Conclusion	50
3.7	Generalized Transfer Matrix	50
3.8	Acknowledgement	51
4	A Perturbation Approach for Ultrafast Calculation of RF Field Enhancements near Medical Implants in MRI	57
4.1	Introduction	59
4.2	Results	63
	4.2.1 Theory to circumvent the offline calculation	63
	4.2.2 Simulation results for different medical implants	65
4.3	Discussion	70
4.4	Methods	74
	4.4.1 Simulation details	74
	4.4.2 Theory prior method	76
4.5	Acknowledgements	77
5	Workflow for Subject-Specific RF Safety Assessment of patients with Orthopedic Implants in MRI	81
5.1	Introduction	83
5.2	Methods	85
5.3	Results	90
5.4	Discussion	92
5.5	Conclusion	95
6	Transceive phase corrected 2D contrast source inversion-electrical properties tomography	97
6.1	Introduction	99
6.2	Theory	100
	6.2.1 Transceive Phase Correction	100
	6.2.2 Numerical Implementation Of The RF-Shield	103
6.3	Methods	104
	6.3.1 Simulations	104
	6.3.2 Measurement	107
6.4	Results	108
6.5	Discussion	113
6.6	Conclusion	117

7	Summary	119
8	General discussion	123
8.1	Transfer function validation	123
8.2	Accelerating RF simulations for implants	125
8.2.1	Applications	126
8.2.2	Further improvements	129
8.3	Electrical properties tomography	130
9	List of Publications	147
9.1	Journal publications	147
9.2	Conference Proceedings	148
10	Curriculum Vitae	149
11	Dankwoord	151

General introduction

*Peter R.S. Stijnman, Cornelis A.T. van den Berg and
Alexander J.E. Raaijmakers*

Magnetic resonance imaging (MRI) provides a non-invasive method to view the inner workings of a patient. One of the reasons that MRI is one of the main imaging modalities in modern hospitals is its superior soft-tissue contrast. This entails that clear distinctions between different tissue types can be made, particularly discerning healthy from unhealthy tissue. Furthermore, MRI can be used to create both anatomical and functional images. As a small selection, this includes different tissue contrasts, e.g. T_1 or T_2 weighted images, but it is also possible to do MRI-angiography or even monitor brain activity using fMRI. The wide variety of image types that can be acquired with MRI, therefore, provide valuable complementary diagnostic value.

Even though there are many benefits for using MRI as a diagnostic tool there are also a few disadvantages compared to other imaging modalities (e.g. CT or ultrasound). The biggest disadvantage of MRI is that it is a time-intensive and expensive imaging modality [1]. Another disadvantage of MRI is the safety concerns for a specific patient group, those with medical implants. MRI is a very safe imaging modality because it does not use ionizing radiation but rather magnetic fields. However, these same magnetic fields pose several safety issues concerning medical implants, e.g. orthopedic implants [2, 3, 4, 5, 6]. As a result of these safety concerns, patients with medical implants are often not eligible for an MRI examination.

1.1 Magnetic fields in MRI

To explain the safety concerns in more detail, we will explain briefly the different magnetic fields that are present inside the MRI system. In total three different magnetic fields are used. One magnetic field is static in time, the other two magnetic fields are time-varying magnetic fields. The static magnetic field will range from 0.5 T to 3 T for most clinical systems, for reference a typical refrigerator magnet will be in the order of 0.005 T. The second magnetic field is the gradient magnetic field, this magnetic field is used for the spatial localization of the signal. There is a gradient magnetic field generated for each of the three axes in the MRI, i.e. left-right, feet-head, and anterior-posterior. These gradient magnetic fields are in the order of mT. Finally, the third magnetic field is the radiofrequency field (RF), which is generated by the RF coil inside the MRI and is used to create and measure the MR signal. The RF field operates at what is called the Larmor frequency dictated by the static magnetic field, this frequency is given by

$$f_0 = \frac{\gamma}{2\pi} B_0. \quad (1.1)$$

Where f_0 indicates the frequency, $\frac{\gamma}{2\pi} = 42.577$ MHz/T for ^1H , and B_0 is the strength of the static magnetic field. The magnitude of the RF magnetic field is in the range of 1 to 20 μT .

1.2 Safety concerns

All three of the magnetic fields in MRI can interact with an implant potentially creating hazardous scenarios. The static magnetic field will attract magnetic materials potentially causing projectile events [7, 8]. For this reason ferromagnetic materials are not allowed inside the MRI scanner. If a patient has an implant consisting of a ferromagnetic material they are not eligible for MRI examination since the implant could be displaced inside the MRI. Other interactions of implants with the static magnetic field include rotational forces applied to the implant and interactions with magnets inside active implants (e.g. cochlear implants).

For the RF magnetic field there are multiple safety concerns for patients with an implant [3, 9, 10]. The most pressing safety concern is a result of the time-varying behaviour of the RF magnetic field that, as stated by Maxwell's equations, is accompanied with an RF electric field. This RF electric field induces currents inside the patient and implant. The induced currents in implants can result in charge accumulation, especially at the tip of electronic leads found in for example pacemakers and deep brain stimulators. These charge accumulations create RF electric fields in the tissue surrounding the

implant. This electric field will deposit energy in any tissue with a conductivity, σ , larger than 0.0 S/m. This energy deposition is expressed as the specific absorption rate (SAR)

$$SAR(\vec{r}) = \int \frac{\sigma(\vec{r})|E(\vec{r})|^2}{\rho(\vec{r})} dV. \quad (1.2)$$

Where \vec{r} is the position vector, the RF electric field E , the location within the MRI, ρ is the mass density, and dV is the volume of cube/voxel at each position in \vec{r} . The unit for the energy deposition is W/kg and causes the temperature increase of the subject in the MRI.

Most implants contain metallic parts that have a very high conductivity ($> 10^6$ S/m), compared to the conductivity of tissue which is between 0.0 and 2.0S/m. Because of these high conductivity values, the RF electric fields can be very localized near the boundaries of the implant resulting in temperature hotspots. Temperature increases upwards of 20°C have been reported for various types of implants. Tissues can be permanently damaged when exposed to these temperature increases for extended periods of time. Other safety concerns that are associated with the RF magnetic field for active implants are unwanted therapeutic dose delivery and damaging of the electronics.

For the gradient magnetic fields the same safety concerns exist as for the RF magnetic fields [11, 12]. However, as a result from the lower frequency of these magnetic fields the risk of significant temperature increases is lower.

1.3 Safety assessment

While there are extra safety concerns for patients that have medical implants, this patient group could greatly benefit from an MRI examination. As an example, it has been estimated that 50-75% of patients that have a pacemaker would benefit from an MRI scan within the lifetime of the medical implant [13]. Therefore, to enable patients with medical implants to still undergo an MRI examination the MRI implant safety community, consisting of researchers, hospitals, MRI manufacturers, and implant manufacturers, have designed a technical specification describing methods to test the safety of specific active medical implants [14]. There is also a technical standard for the MRI safety testing of passive implants (e.g. knee joints and hip replacement implants) [15].

Performing such a safety assessment as described in the technical specification will result in a document or label stating under which constraints, if any, the implant can be safely scanned. This is reviewed by the Food and Drug Administration or similar organisations. The label can either be MR safe, MR conditional, or MR unsafe specifying that the implant is allowed inside the MRI under any condition, given certain restrictions, or not at all, respectively. This

safety assessment is often done only for standardized implants such as pacemakers, deep brain stimulators, and spinal cord stimulators. However, there is a large number of implants that do not have such an MR label. These implants without a label include old implants for which there has not been a safety assessment and for most orthopedic implants, e.g. hip implants, there are no MR labels. For orthopedic implants this safety assessment is not performed because they are tailored specifically towards the patient, therefore, requiring a safety assessment for every variation of an orthopedic implant. While there are some MR safe orthopedic implants it is often unfeasible to perform the safety assessment as it is a time-intensive task. As a result, patients with non-labelled implants are not eligible for MRI examination.

The fact that there are non-labelled implants does not entail that these implants are inherently MR-unsafe. When these implants do not contain ferromagnetic materials they might be MR-safe. Based on the size of the implant and the tissue surrounding the implant the RF interaction of the implant can be estimated. For this reason there are some larger hospitals with the right expertise that do scan patients with non-labelled implants. While it would be possible, smaller hospitals without this expertise do not scan such patients, often for legal reasons.

For the safety assessment, there are more safety concerns taken into account than only the RF safety concern for high-temperature increases as mentioned above. Some examples include the interaction with the static magnetic field, which has the potential to create projectile events, and device malfunctioning resulting from the gradient and RF fields. However, in this work, we will focus on the safety assessment of the temperature increase resulting from the RF fields.

1.3.1 Tier-based RF safety assessment

In the technical specification, the RF safety assessment of an implant is split up into four different tiers, where a higher tier requires more accurate testing and simulations but will result in an MR label that has lower restrictions. Tier 1 and 2 are reserved for electrically short implants, i.e. much smaller than the wavelength of the RF fields inside a medium with tissue like electrical properties, and require little to no simulation work to be performed. Tier 3 and 4 both require a significant amount of simulation and measurement work to be performed [14].

The reason for there being multiple tiers in the RF safety assessment is that accurately simulating the RF field distribution is a difficult and computationally demanding task. The simulation domain is large compared to the very fine details of implants. Especially implants with leads are difficult to simulate because of the helical structure inside the leads. Therefore, all tiers with the exception of tier 4 simplify the problem in order to assess the RF safety

of an implant faster.

To enable the faster RF safety assessment the first three tiers use the transfer function (TF) of the implant. This TF describes, given an RF electric field inside a subject when the implant is not present how large the magnitude of the scattered RF electric field resulting from the implant will be. The TF is defined for electrically long implants where it is known where the temperature hotspot will occur. An example is a pacemaker, where we know that the temperature hotspot will occur where the therapeutic dose is delivered. This will be at the end of the electronic leads of the pacemaker since the rest of the lead is insulated but the tip is not. At this location charge accumulation will occur creating high RF electric fields in the surrounding tissue, depositing energy. The TF is defined as

$$E^{tip}(\vec{r}) = \hat{E}^{tip}(\vec{r}) \int_0^L TF(s) E_{tan}(s) ds. \quad (1.3)$$

Where E^{tip} is the scattered RF electric field at the tip of the lead, \hat{E}^{tip} is the scattered RF electric field at the tip for a unit exposure of the tangential incident RF electric field, E_{tan} , L is the length of the lead, and ds are the segments along the length of the lead [16].

For tier 1 of the RF safety assessment, the largest magnitude of the RF electric field simulated in a human body model is used as value for the E_{tan} . The difference between tier 1 and tier 2 is that the largest magnitude of the RF electric field inside a clinically relevant position of the implant inside the human body model is used, i.e. for deep brain stimulator the RF electric field outside of the torso and head is neglected for finding the largest magnitude. For the tier 3 RF safety assessment the E_{tan} along clinically relevant trajectories is used, RF electric field distributions in multiple human body models are simulated for different MRI scanning positions. Finally, in tier 4 every clinically relevant configuration of RF coil, patient position, and implant location is simulated, the TF is not used in this tier.

The TF can be measured in a phantom setup or it can be simulated using an electromagnetic solver. More recently an alternative measurement method for the TF has been developed by Tokaya et al [17, 18]. Unlike existing measurement methods this newly developed measurement method utilizes the MRI system. The current induced inside the implant by the RF coil creates an image artefact in the RF magnetic field. This image artefact can be measured using the MRI system itself. From the RF magnetic field artefact the induced current inside the implant can be calculated. Using the induced current and the incident tangential RF electric field the transfer matrix (TM) can be measured. The TM is an extension to the TF where the first column of the TM is equal to the TF.

The TF is measured inside a homogeneous dielectric, and the assumption is made that a heterogeneous dielectric will not change the TF. Furthermore, for

the measurement of the TF, the lead is in a straight trajectory, while *in-vivo* this is not the case and the lead can interact with itself, effectively altering the TF [19, 20, 21]. As a result, the tier 3 RF safety is not the highest tier, as it is more accurate to simulate (or measure when possible) the scattered RF electric field with the RF coil, human body model, and implant combined. Concurrently simulating all three aspects is required for a tier 4 RF safety assessment.

A tier 4 RF safety assessment is seldom performed as it would require millions of simulations for every possible configuration of RF coil, human body model, and implant position/trajectory. With each simulation requiring hours of computation time using standard electromagnetic solvers, this is an unfeasible task.

Even if a tier 4 RF safety assessment would be performed the MR label that will result from it will bear restrictions, similar to the other tiers, based on the worst-case scenario that is present within the millions of simulations. Thereby, for the majority of patients, the MR label will impose a restriction of the amount of power that can be used by the RF coil that is overly conservative. This entails that either the image quality will be lower and/or that the MR scan requires more time. Furthermore, there is still a group of patients that have a medical implant that has no label at all. Even when these patients are scanned at the select amount of hospitals that have the expertise to do so, the hospital will always scan with a very conservative amount of power to ensure safety.

To alleviate these overly conservative scanning restrictions, in this thesis, we present alternatives to the RF safety assessment of MRI-compatible implants. Ultimately, we want to have a set of tools that can predict the patient-specific local SAR increase near an implant. Thereby, allowing more patients with non-labelled implants to be eligible for MRI examination, both in hospitals with and without the expertise of scanning this patient group.

1.4 Thesis outline

The progress towards this goal is described in this thesis, where we start with **Chapter 2** that highlights a new validation method for the TF. Continuing the work of measuring the TF of an elongated medical implant using the MRI system, we show that it is also possible to validate this measurement with a separate method using the MRI system. The validation of the TF is an important step to correctly predict the eventual temperature increase. Especially since the measured TF is correct up to some arbitrary global scaling. This global scaling and the validity of the TF is determined with a validation procedure that uses an independent measurement technique.

The remaining chapters focus more on the simulation techniques rather

than measurement techniques for the RF safety assessment. In **Chapter 3**, we showcase that a very fast simulation technique, which was developed for RF field calculations of high permittivity pads can also be used for the RF safety assessment of medical implants. This simulation technique can calculate how the RF fields change as a result of a small change (i.e. a new dielectric scatterer) in the simulation setup. To perform this calculation a base simulation of the RF fields without the implant is required which is the so-called library matrix that describes the electromagnetic field response for every point within the domain where the new scatterer is present.

Chapter 4 continues with the same simulation technique. The main point is to make this technique more flexible and expand its applicability. In order to accomplish this, we reformulated the method to no longer require a large amount of data to be computed and stored beforehand, i.e. we no longer use the library matrix. This requirement limited the use of the method to small medical implants because the time required to calculate the data beforehand would be in the order of months for large medical implants. Moreover, the amount of memory necessary to store the results would be unfeasible for modern computers. Using a matrix-free minimization scheme and GPU hardware acceleration we retain the quick simulation times and remove most of the memory limitations.

Chapter 5 is a demonstration of the previously discussed simulation method. We show a workflow proof of concept where the implant location within patients is obtained from X-ray images. Using the implant location we can perform an RF safety assessment simulation study for each patient within 2 to 3 hours resulting in a patient-specific 1 g averaged SAR increase around the implant. This information can be used to better assess the risk for patients with non-labelled implants or it can be used to alleviate the worst-case scenario scanning restrictions for labelled implants.

Chapter 6 describes how the MRI system can be used to obtain the electromagnetic properties of tissue. For MRI the conductivity, as previously mentioned, and the permittivity of different tissues will determine the electric and magnetic RF fields that are generated by the RF coil of the MRI system. Therefore, having knowledge about these two quantities can provide valuable information about RF safety for patients with and without medical implants. Furthermore, information about the conductivity can be used as a different contrast mechanism compared to the other readily available image contrasts the MRI system can generate. One potential example is that conductivity may be used as a biomarker for cancerous tissue.

A Single Setup Approach for the MRI-based Measurement and Validation of the Transfer Function of Elongated Medical Implants

*Peter R.S. Stijnman, Cornelis A.T. van den Berg and
Alexander J.E. Raaijmakers*

Based on: P.R.S. Stijnman, M.A. Erturk, C.A.T. van den Berg and A.J.E. Raaijmakers. A single setup approach for the MRI-based measurement and validation of the transfer function of elongated medical implants. Magn Reson Med. 2021; 86: 2751– 2765. <https://doi.org/10.1002/mrm.28840>

Abstract

Purpose: To propose a single setup using the MRI to both measure and validate the transfer function (TF) of linear implants. Conventionally, the TF of an implant is measured in one bench setup and validated using another.

Methods: It has been shown that the TF can be measured using MRI. To validate this measurement the implant is exposed to different incident electric fields while the temperature increase at the tip is monitored. For a good validation, the incident electric fields that the implant is exposed to should be orthogonal. We perform a simulation study on six different methods that change the incident electric field. Afterward, a TF measurement and validation study using the best method from the simulations is performed. This is done with fiberoptic temperature probes at 1.5T for four linear implant structures using the proposed single setup.

Results: The simulation study showed that positioning local transmit coils at different locations along the lead trajectory has a similar validation quality compared to changing the implant trajectory (i.e. the conventional validation method). For the validation study that was performed an $R^2 \geq 0.91$ was found for the four investigated leads.

Conclusion: A single setup to both measure and validate the transfer function using local transmit coils has been shown to work. The benefits of using the proposed validation method are that there is only one setup required instead of two and the implant trajectory is not varied, therefore, the relative distance between the lead tip and the temperature probe is constant.

2.1 Introduction

Strong radio frequency (RF) fields emitted by MRI scanners may interact with active implantable medical devices (AIMDs) in patients. The AIMD is capable of enhancing the MRI radio frequency (RF) fields resulting in increased power deposition around the AIMD, potentially causing excessive tissue heating [22, 23, 24, 14, 5, 25]. As a result, patients with an AIMD could be deprived of a valuable imaging modality.

For this reason, implant manufacturers are striving to make their products MRI safe, at least within certain predefined MRI operational constraints. Therefore, a technical specification (TS), ISO/TS-10974, has been developed by implant manufacturers, major MRI vendors, and the MRI community to evaluate the safety of patients with AIMDs undergoing MRI examination [14]. Clause 8 in the TS describes simulation and measurement procedures that need to be performed to assess the RF heating response of AIMDs under MRI exposure conditions. One important implant characteristic described in the TS is the transfer function (TF) [16]. The TF decouples the scattered electric field created by the implant from the incident electric field created by the transmit RF-system. When the TF for an AIMD is known the local enhancement of the electric field can be evaluated quickly and can indicate the temperature increase that can be expected for a certain exposure condition.

The TF is especially relevant for electrically long implants (e.g. AIMDs containing electrodes/lead structures) and can be obtained through either simulation or measurement. When the TF is obtained it needs to be validated. In the conventional TF measurement setup, the electric field at the tip of the implant is monitored while the AIMD is exposed to a local tangential electric field moving along all locations of the lead trajectory [26, 27]. The electric field could be created with two sliding parallel plates, a loop coil or an antenna for example. During these measurements, the lead is submerged in saline water with tissue-like conductivity.

Recently, it was shown that the TF can also be measured using an MRI system [28, 17]. For this MRI-based methodology, the concept of the transfer matrix (TM) has been introduced. The TM relates the incident electric field to the induced current along the lead and can be obtained from MRI measurements through current mapping and a model that describes the TM with only a couple of parameters. The TF is by definition the first column of the TM.

Once the TF has been obtained, a validation step is required which can be performed through local temperature rise measurements. For the validation of the TF, the AIMD is typically placed in a phantom containing a high-viscosity gel (e.g. HEC) with the same dielectric properties the TF was initially measured in. At the tip of the lead structure, a temperature probe is placed to monitor the temperature increase. This setup is positioned inside a realistic

MRI RF transmit coil and the implant is exposed to the incident electric field generated by this RF transmit coil. In between temperature measurements, the trajectory of the lead is altered to obtain different, preferably orthogonal, exposure conditions. Afterward, the measured temperature increase is correlated with the temperature increase calculated using the TF and the known incident electric field. This approach to validate the TF has some drawbacks.

Firstly, to create a significantly different exposure along the lead, the lead trajectory needs to be changed in such a fashion that it may interact with itself. Therefore, the electric field created by the lead at one position can couple into the lead at another position. This effectively alters the TF of the lead which is unwanted since it is the quantity that needs to be validated [29]. Simply shifting the straight lead to a different location in the phantom is not sufficient to create a different exposure condition.

The second problem is the placement of the temperature probe at the tip of the lead. For the measurements to be effective the relative distance between the temperature probe and the lead tip needs to be consistent and preferably within a few millimeters of each other. Keeping the relative distance constant is important because the temperature hotspot that is created is highly localized and the temperature gradient is steep [30].

Therefore, an alternative method has been presented where instead of changing the trajectory of the lead within the phantom, a multi-transmit coil array is used to alter the incident electric field distribution using a large set of phase-amplitude drive settings [29]. This method could also be achieved with a dual-transmit birdcage body coil. The downside of using this method, however, is that the incident electric fields are often very similar. Such a setup can only generate a fixed potential maximum number of exposure conditions that are equal to the number of elements in the array. Of course, these systems have the ability to impose an infinite variation of field distributions on the implant using varying phase and amplitude settings. However, these field distributions are superpositions of the fields created by the independent elements of the array and are therefore linearly dependent.

There are also other options to create different exposures along the lead trajectory for the validation of the TF instead of altering the trajectory itself. Here, we will be aiming at validation methodologies that use an MRI setup which would enable the MRI-based measurement and subsequent validation in one session. The first alternative method would be to move the phantom with respect to the birdcage coil and with it, its associated electric field distribution.

The second option is to drive a dual-transmit birdcage body coil in various phase-amplitude combinations [31]. However, as discussed this will only provide a maximum of two orthogonal exposure conditions. This method could still be combined with one of the other methods described here.

The third option is to use passive scatterers to change the exposure. A

first example is dielectric padding [32, 33]. These dielectric pads have a high permittivity and are placed between the coil and the patient or phantom and change the incident RF fields. Similar effects may be observed for materials with high conductivity and resonant structures (e.g. a tuned loop). These passive scatterers could be placed at different positions along the lead to locally vary the incident electric field.

The final option, similar to the multi-transmit coil array, would be to use small local transmit RF coils to apply a localized exposure which could also be placed at different positions along the lead trajectory without moving the lead itself [34, 35, 36, 21]. In other words, moving the transmit coils rather than changing the lead trajectory, which facilitates a constant relative distance between the lead tip and the temperature probe. This entails that the birdcage transmit coil is used for the TF measurement and the local transmit coils would be used for the validation of that TF measurement.

In this study, we aim to develop a new validation procedure that is particularly suitable for validating MRI-measured TFs. The study consists of two parts: first, we will simulate the methods described above to identify the best validation methodology. Second, we use the best method to perform a complete experimental workflow of MRI-based TF measurement and validation for four elongated structures: two copper wires (i.e. one bare and one insulated), a realistic coaxial implant lead, and a spinal cord stimulator.

2.2 Methods

2.2.1 Simulation based investigation of potential validation methods

In this section, we will describe how the selected validation methods have been simulated and we define a metric to assess the different validation methods called the validation quality.

All methods are evaluated for the validation quality of a non-specified structure of 40 cm length that is placed within an ASTM phantom. The phantom is filled with hydroxyethylcellulose-gel (HEC) with a relative permittivity of 78 and a conductivity of 0.34 S/m.

The intended validation method setup is simulated using the numerical EM simulation package Sim4Life (v5.0, ZMT, Zurich, Switzerland). All methods except the local transmit method make use of the birdcage body coil of the MRI system. The dimensions of the birdcage coil, the ASTM phantom, and all other parts used for the validation methods are indicated in Figure 2.1.

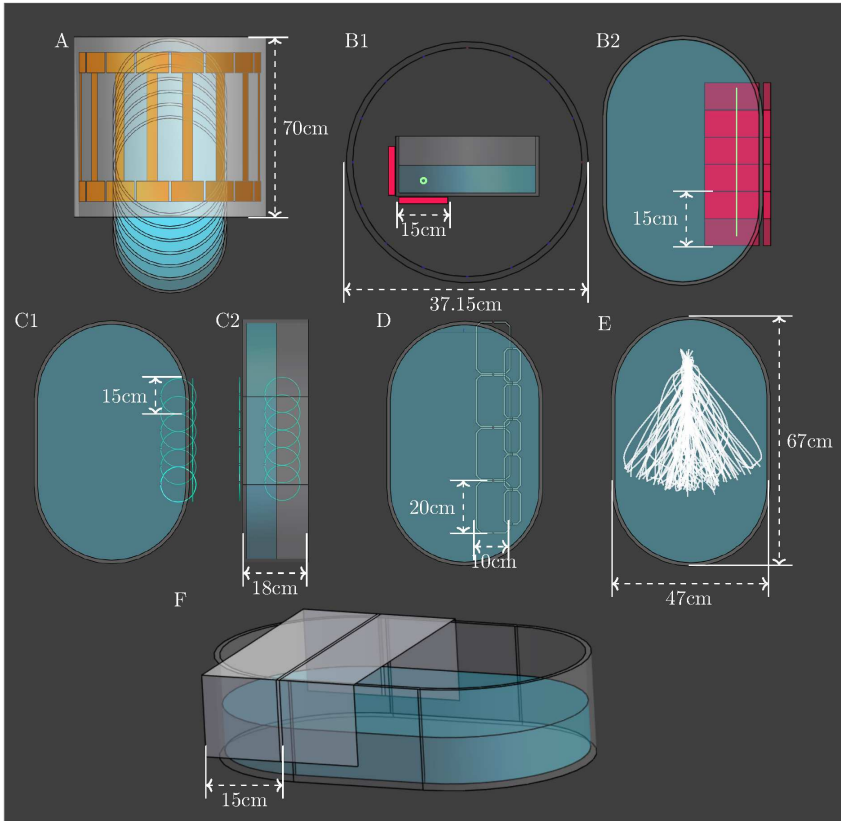


Figure 2.1: All the simulation setups that were used to investigate the methodologies to change the incident tangential electric field. A) shows how the phantom was shifted out of the birdcage coil. B1) & B2) show the side and top view of the dielectric pads. The electric field is extracted at the location of the light green trajectory, this location within the phantom is used for all methodologies except changing the trajectory. C1) & C2) show the top and side view of the passive RF coil positions. D) displays the local transmit coil positions. E) indicates the 100 random implant trajectories that were extracted and finally F) shows an example of how the phantom was wrapped in aluminum foil.

Shifting the Phantom

As mentioned in the introduction, it is possible to create different exposure conditions using a dual-transmit birdcage coil and shifting the phantom along

the bore axis with respect to the coil. Starting with the ASTM phantom centered inside a birdcage coil and shifting it 50 mm outwards of the coil along the center bore axis to a maximum of 300 mm.

Passive Scatterers

This category consists of three different methods: Dielectric pads, aluminium foil shielding, and passive resonant RF loops. A dielectric pad with a relative permittivity of 450 is used to create different exposure conditions. The placement of the aluminium sheets are shown in Figure 2.1 and Supporting Information Figure S1. A total of 10 configurations were simulated. The resonant loop coil has a thickness of 3 mm, a capacitor value of 28.6 pF, and placed at the same locations as the dielectric pad. For all three methods described above the birdcage coil was simulated as a multiport simulation to obtain twice the number of exposures.

Local Transmit Coils

We simulated two rectangular local transmit loop coils made with strips, simulated as a perfect electrical conductor. The loop coils are tuned to 64 MHz using two capacitors and are placed along different positions of the lead trajectory.

2.2.2 Validation Quality

To adequately validate the measured TF, the incident tangential electric fields that the lead is exposed to during the validation should be linearly independent with respect to each other (i.e. over the domain \mathbb{C}^n with n the number of segments along the lead). A method where a higher number of linearly independent exposure conditions can be realized means it is more suitable. For example, electric field distributions that always have the same amplitude and phase distribution, and are only scaled globally, are not linearly independent and would result in a poor validation quality. A better set of distributions preferably has many linearly independent incident electric field distributions.

To assess which validation method performs best in terms of the validation quality and effectiveness we use the singular value decomposition (SVD). The SVD will decompose any matrix into orthogonal vectors and a matrix containing singular values. Consider a matrix that consists of a collection of vectors as its columns. The singular values associated with this matrix indicate the lengths of the orthogonal vectors. If many of the original vectors are linearly dependent, the singular values will quickly decrease to zero. This entails that the original matrix can be described predominantly by a small number of orthogonal vectors. If the vectors are linearly independent, the singular values

will be higher and the original matrix can only be adequately described by using a larger number of orthogonal vectors.

For the validation methods that we simulated, the set of incident tangential electric field distributions is extracted along the implant trajectory (when the implant is not present). These different exposures are first normalized to equal vector length and then all placed as columns into a matrix. This matrix is then decomposed using the SVD where the resulting singular values are normalized and summed to obtain a single metric for the validation quality. Where a higher number indicates a better validation (i.e. more linearly independent exposure conditions).

2.2.3 Proof-of-principle validation study using the best performing MRI-setup validation method

The second part of this study will focus on performing a combined TF measurement and validation study for four linear implants. The first is a 36 cm bare copper wire, the second a 36 cm insulated copper wire. The third is a 40 cm coaxial implant lead (which was supplied to us by Medtronic (Fridley, Minnesota, USA)) with a tip structure on one end, while the other end is insulated. The last implant is a spinal cord stimulator (Medtronic, Prime Advanced Sure Scan MRI) with an IPG at one end and an electrode array at the other end. Furthermore, there are two leads of 70cm running from the IPG to the electrodes. The diameter of the copper wires is 2.5mm and the insulation layer has a thickness of 1mm, the diameter of the coaxial lead is 1.25mm. The lead structures are shown in Figure 2.2.

The phantom that was used in this measurement and validation study is the same ASTM phantom that was used in the simulation-based study described in the section above.

The leads and the temperature probe are suspended inside the phantom using plastic screws and nylon threads. Fixating the leads and the temperature probe enables them to be close to each other and not drift away or sink to the bottom of the phantom, all while maintaining the signal around the lead intact for MRI measurements. Particular care has been given to ensure that the temperature probe cannot move relative to the lead tip.

2.2.4 MRI-based transfer function measurement

For the transfer function measurement, the procedure has been followed as described by Tokaya et al. [17]. This procedure makes use of the TM of the implant. To obtain the TM from an MRI experiment the induced current (I^{ind}) and the incident tangential electric field (E_{tan}^i) are required to minimize

$$f = \|I^{ind} - TME_{tan}^i\|_2^2, \quad (2.1)$$

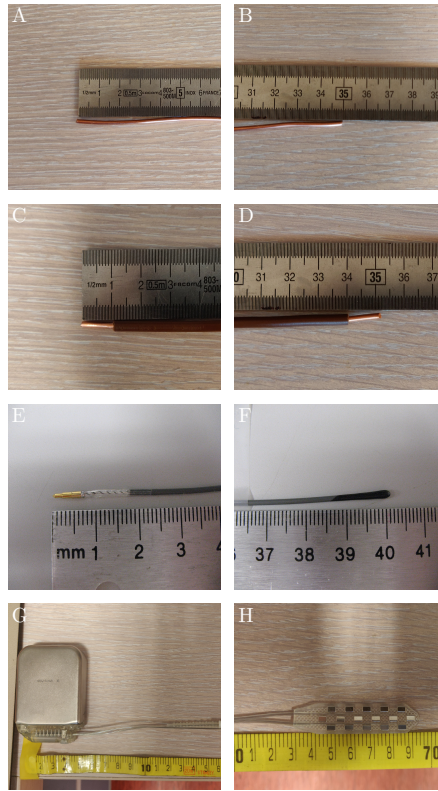


Figure 2.2: The ends of the implants for which the TFs were measured and validated. A) & B) show both ends of the bare copper wire. C) & D) show both ends of the insulated copper wire where the ends of the insulation are removed for about 1cm. E) & F) show the ends of the coaxial lead and a proper lead tip. G) & H) show the IPG and the electrode patch of the spinal cord stimulator respectively.

where TM is the transfer matrix. Using an attenuated wave model, the matrix is parametrized by only a few unknowns (i.e. 6 to 10 for the lead structures defined here) [17]. The magnitude of the induced current and the phase difference between the current and the background B_1^+ are calculated from the measured B_1^+ magnitude distribution around the lead. This $|B_1^+|$ distribution is obtained by using a fast field echo (FFE) series with variable flip angles. For this work, we used FDTD simulations to obtain the incident tangential electric

field and the phase information of the incident B_1^+ (i.e. this phase information together with the measured phase difference is used to calculate the phase of the induced current) field to fit the TM [17].

2.2.5 Transfer function simulation

For reference, the TF of the four investigated leads were also simulated using the same EM modeling package Sim4Life. We obtained simulated TFs by performing the MRI-based TF measurement in-silico as outlined by Tokaya et al. [17]. These TFs were obtained from simulated B_1^+ fields rather than measured B_1^+ fields. The same geometries as in the actual MRI-based measurements were used.

2.2.6 Validation Method

To validate the TF using temperature measurements we correlate the SAR from the temperature measurement and the SAR we calculate using the TF and the incident tangential electric field obtained from simulations. To calculate the actual SAR from the temperature measurement we use the fact that the initial slope of the temperature increase is proportional to the SAR [37],

$$SAR = c \frac{\partial T}{\partial t} \Big|_{t=0}, \quad (2.2)$$

where c is the specific heat capacity of the tissue surrounding the lead tip, T is the temperature and t is the time. The temperature was sampled every 0.7s. To accurately obtain the initial slope of the temperature increase, we fitted a set of exponential growth and decay functions to the temperature curve [38]. This fit allows us to use all the data points of the curve.

To calculate the SAR using the TF we first calculate what the scattered electric field at the tip of the lead is given the incident tangential electric field. Then together with the incident electric field created at the tip by the source, we can compute the SAR at the lead tip by

$$SAR \propto \sigma(|\alpha_1 E^{sc} + E^i|^2), \quad (2.3)$$

here σ is the conductivity of the surrounding dielectric and α_1 is the calibration coefficient we need to compute since the TFs that are measured are all normalized. This calibration coefficient is calculated using linear regression between the predicted SAR using the TF and the measured SAR from the temperature probes. Afterward, we can compute the R^2 for this linear regression and find out how well the TF describes how the implant reacts to the incident fields.

2.2.7 Validation Measurement

For the validation of the TF, we used local transmit coils to create the incident RF fields and varied the incident electric field by shifting the transmit coils along the lead between different heating tests. The transmit coils that were constructed had the same dimensions as the ones simulated. The transmit coils were tuned to 64MHz and matched using a vector network analyzer. The measurement series was performed once with the smaller coil and once with the larger coil. For the larger coil, it was moved in steps of 6 cm and the small coil in steps of 4 cm. This in total created 10 different measurements per lead structure. To connect the local transmit coils to the MRI scanner, the birdcage coil was unplugged from the quadrature hybrid power unit and connected with dummy loads. Afterward, the local transmit coil was connected to one of the quadrature hybrid output channels while the other channel was connected to a dummy load.

The temperature increase is measured using fiber optic temperature probes (OpSens, type: OTP-M, resolution: 0.01k, accuracy: 0.30k (99.9%confidence level)) that can be used inside the MRI system (Ingenia, Philips). To accurately measure the temperature increase as a result of the lead only, a temperature probe at the tip of the lead and a reference background temperature probe is required. The temperature probe at the tip of the lead will measure the temperature increase as a result of the incident and scattered electric while the reference temperature probe is positioned away from the lead. This reference temperature probe will measure the temperature increase that is associated with only the incident electric field. The temperature probe at the tip of the lead is placed close (less than 2mm away) to the tip of the lead to obtain a reliable correlation [30].

To generate sufficient heating for the probes to register and for us to predict, we use the MRI system to deposit power into the phantom. This was achieved with a turbo spin echo (TSE) with a long echo train (i.e. 25 180° RF-pulses). RF exposure was continued until significant heating has occurred and enough time has passed to obtain a good fit (preferably 0.5 to 1.5 K) or the temperature increase started to flatten.

In Figure 2.3 the temperature measurement setup is shown. This includes the position of the temperature probe relative to the lead tip, the temperature measurement equipment, and how the phantom is placed inside the MRI. The last picture in the figure shows how the placement of the coils was measured with respect to the end of the ASTM phantom.

2.2.8 Uncertainty analysis

From the MR and temperature measurements, we obtain a single predicted and measured SAR value. However, both measurements are subject to noise

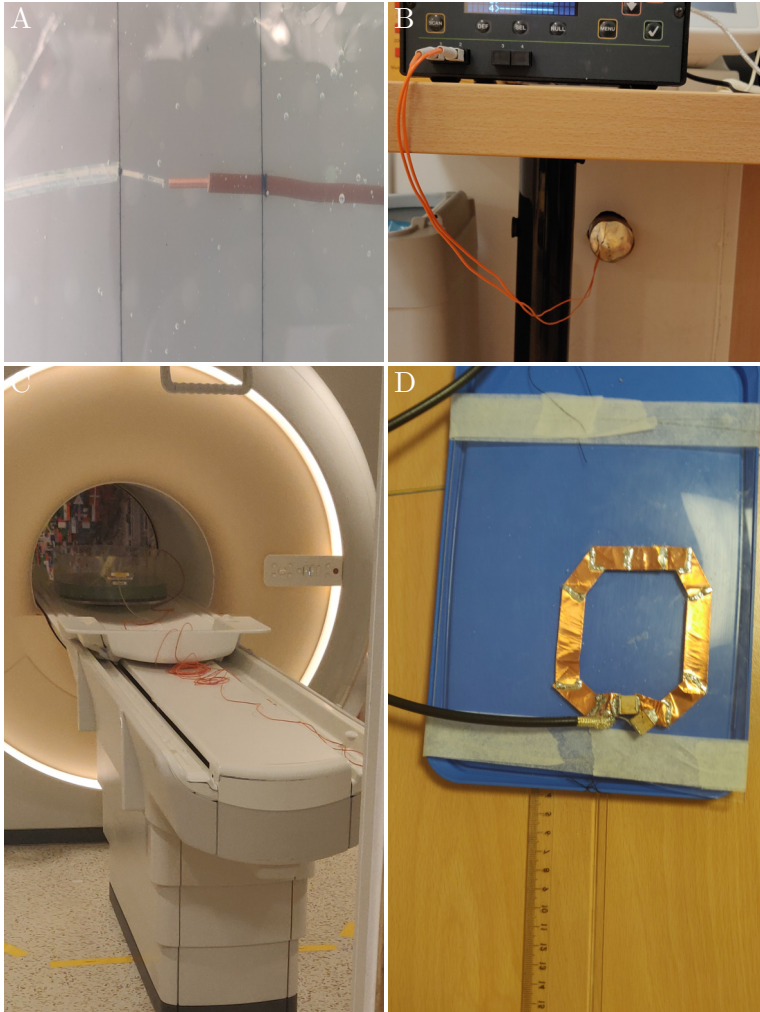


Figure 2.3: Images that detail the measurement setup. A) shows the positioning of the temperature probe with respect to the lead tip. B) shows the temperature measurement device and how the probes are entered through the RF waveguide into the MRI room shown in C). D) using the ruler we measured the distance from the end of the ASTM phantom towards the place of the local transmit coil when it is placed underneath the phantom.

that corrupts the underlying data that affect the resulting SAR values that are found. Therefore, we perform an uncertainty analysis for both the MR and temperature measurements. The result is a standard deviation around the obtained SAR values that show the accuracy of the proposed methodology.

For the temperature measurements, we fit an exponential curve using two parameters. From the fit, we calculate the Jacobian and use that to find the covariance matrix. The diagonal of the covariance matrix is the squared standard deviations of the fitted parameters. These standard deviations are used to calculate the uncertainty of the measured SAR values. This can be interpreted as a range of exponential curves that go through the measured temperature data. This is shown in Figure 2.4 A.

The predicted SAR uncertainty is determined through a Monte Carlo simulation. We first obtain the noise distribution from the FFE series measured with the MR system. From that noise distribution, we sample new noisy data and add that to the original FFE series (i.e. shown in Figure 2.4 B) to create a new FFE series. Afterward, we go through the same step as before to obtain the TF. This includes first a $|B_1^+|$ fit, then a current fit, and finally a TF fit. These steps are visualized in Figure 2.4 C. For all the leads shown in this paper, this process is done 100 times. From the found TFs and the simulated electric field, we obtain a range of predicted SAR values.

2.3 Results

2.3.1 Simulation based investigation of potential validation methods

In Figure 2.5 the magnitudes of the matrices on which the SVD is applied are shown. Each column of the matrices corresponds to the magnitude of the electric field along the implant location, which is extracted from the FDTD simulations. One column in the matrix corresponds to one simulation. It can be observed that shifting the phantom, wrapping the phantom in aluminium, and using dielectric pads do not alter the electric field along the lead significantly. Adding passive resonant loop coils shows more spatially varying exposures. For the local transmit coils and bending the lead we observe the largest changes in the incident electric field distribution along the leads.

After the SVD has been applied to the matrices in Figure 2.5 the singular values are extracted and compared to each other in Figure 2.6. Similar to the observations mentioned above we find that the singular values for the methods: shifting the phantom, wrapping the phantom in aluminium, and using dielectric pads decay rapidly. For the passive resonant loop coil and changing the trajectory, this decay of the singular values is slower. Finally, the singular values for the local transmit loop decay the slowest. The slower

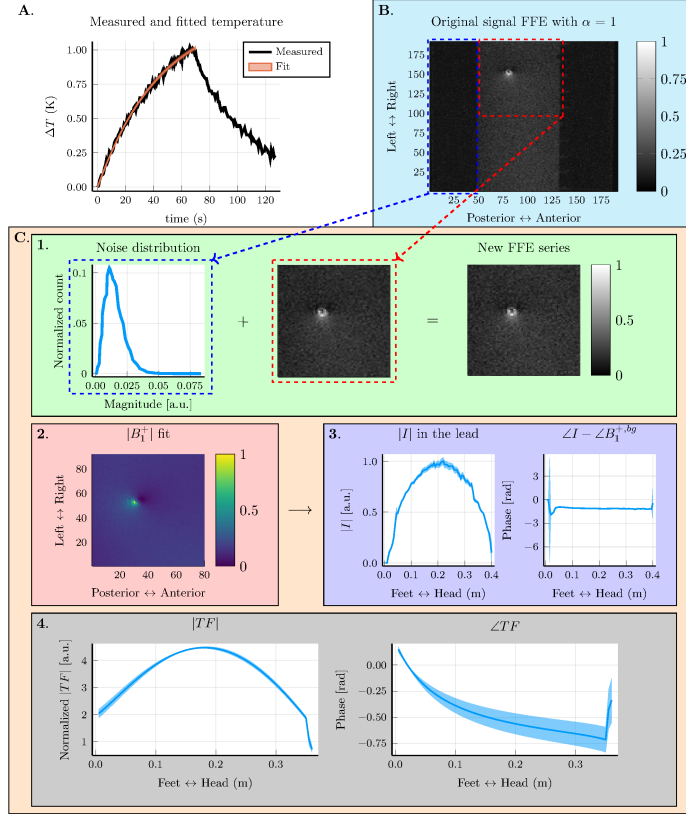


Figure 2.4: The overview of the uncertainty analysis. A) shows the curve fit with uncertainty of a single temperature measurement, this fit is used to find the measured SAR. B) shows a transverse slice of the FFE sequence where the artefact created by the lead is visible. C) shows the steps in the Monte Carlo simulation approach to find the uncertainty of the measured TF and thereby the uncertainty in the predicted SAR. Step 1 is to sample the noise distribution and that noise to the original FFE series to create a new FFE series. Step 2 is to fit the $|B_1^+|$. Step 3 is to fit the current from the $|B_1^+|$. In step 4 we fit the TF using the current and the simulated E_{tan} . The blue-shaded area shows the standard deviation of the measured TF.

the decay of the singular values the more suitable the validation method is for generating orthogonal exposure conditions.

The validation quality of the presented methods is expressed in the sum of

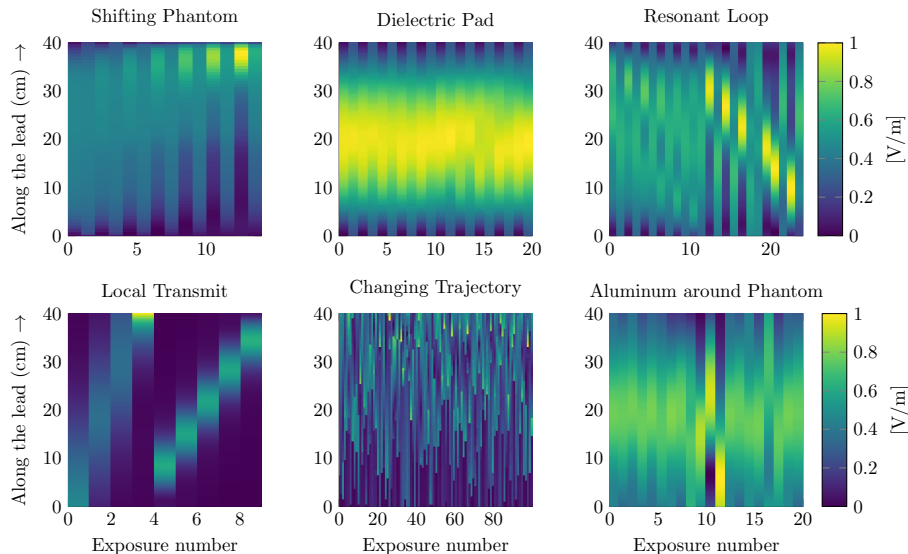


Figure 2.5: The incident tangential electric fields for all the methods described to alter the exposure conditions. Each column is the electric field along the implant trajectory. The columns are normalized to have the same vector length. Afterward, these matrices are used to compare the normalized singular values between the methods.

these normalized singular values and can be observed in the legend of Figure 2.6. This sum indicates how many equivalent orthogonal exposure conditions are subjected to the lead, where a higher sum indicates more information is obtained from conducting those experiments. From Figure 2.6 it is observed that the sum of the normalized singular values for shifting the phantom, wrapping the phantom in aluminium, and using dielectric pads is small (i.e. 1.3, 1.3, 1.1 respectively). For the resonant loop, the validation quality increases to 2.0, but it is still low compared to using local transmit coils at different positions (3.3) and changing the trajectory (3.5). It could be concluded that changing the trajectory will result in the best validation of the TF, however, more temperature measurements are required. Furthermore, local transmit coils have the added benefit that the distance between the temperature probe and the lead tip is constant.

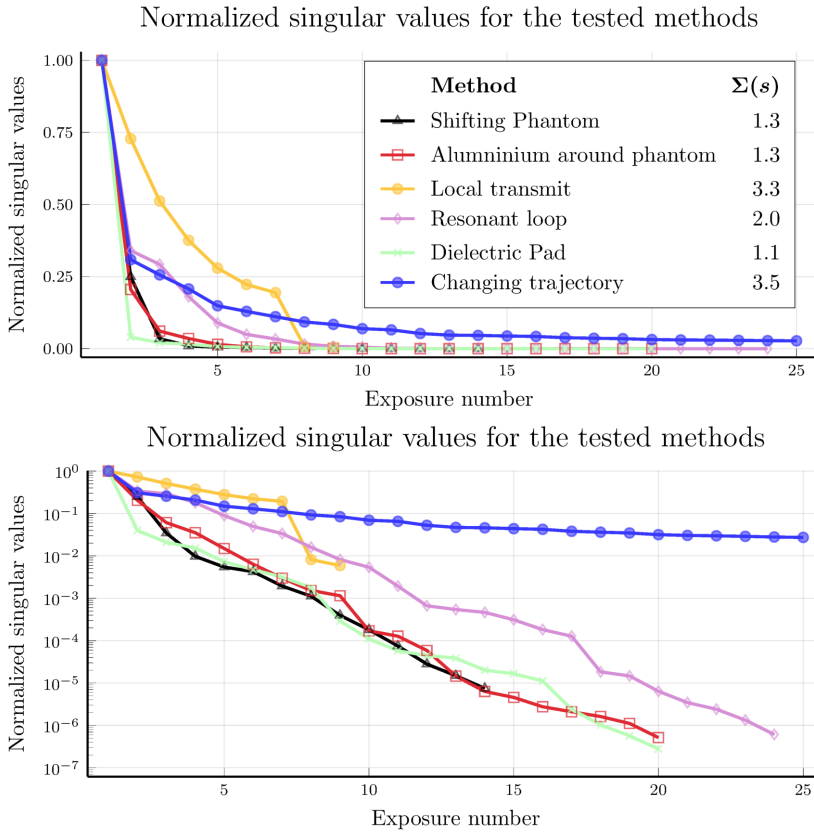


Figure 2.6: The normalized singular values of the different excitation methods. The legend indicates the sum for the different methods where a higher number indicates more equivalent orthogonal exposure conditions, thus more information is obtained using that method. The top figure is on a linear scale and the bottom figure is on a semi-log scale.

2.3.2 Proof-of-principle validation study using best performing MRI-setup validation method

Because of the higher validation quality and the fact that we want to keep the relative distance between the lead tip and the temperature probe the same, the choice was made to construct the local transmit loop coils and use them to create different exposure conditions in the heating test to validate the TFs.

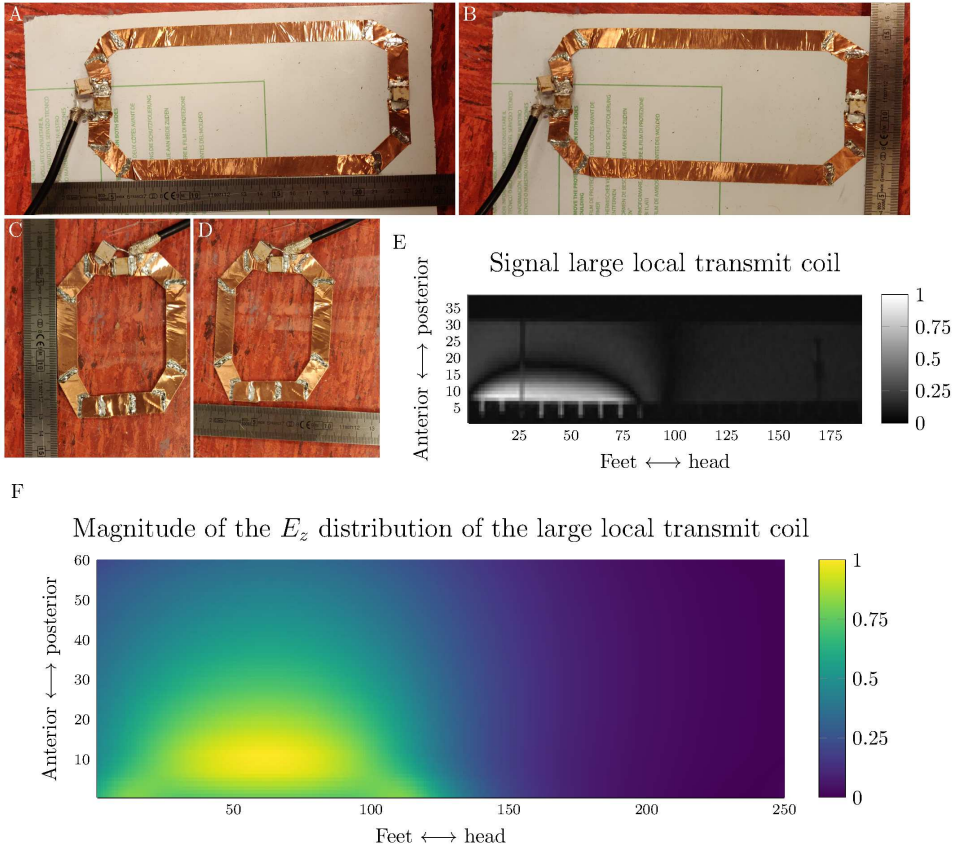


Figure 2.7: The two local transmit coils that were constructed to create different incident tangential electric field exposures along the lead trajectory. A) & B) show the length and width of the larger loop coil and C) & D) show the length and width of the smaller loop coil. E) shows the generated signal of the larger loop coil in a sagittal slice through the phantom. F) shows the corresponding z -component of the electric field.

These constructed loop coils are depicted in Figure 2.7. The smaller coil is on a transparent plastic substrate.

First, the TF was measured for the three investigated structures (Figure 2.2) using a 1.5T MRI system. The resulting TFs are shown in Figure 2.8 along with their simulated counterparts for reference.

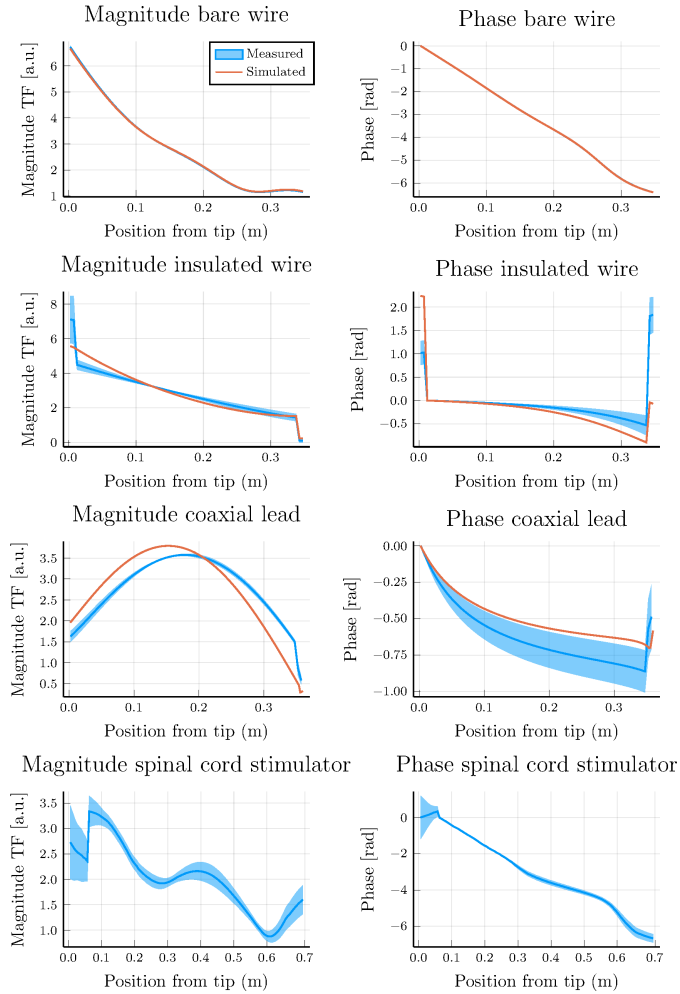


Figure 2.8: A comparison between the transfer functions obtained with FDTD simulations and the transfer function obtained with MRI. The top row of figures shows the magnitude and phase of the transfer function for the bare copper wire. The second row shows the same for the insulated copper wire, the third row shows the TF for the coaxial lead, and the last row is the TF for the spinal cord stimulator. For all the TFs the blue-shaded area displays the standard deviation of the measured TF.

Using the setup depicted in Figure 2.3, we obtained the temperature increases at the tip of the lead as shown in Figure 2.4 A. The temperature measurement is indicated in black and the fitted temperature in orange. Between measurements the position of the local transmit coils was shifted to a different position along the lead trajectory.

Finally, the SAR is obtained from the temperature measurement by fitting an exponential to accurately determine the derivative at the start of the RF exposures. This will be referred to as the measured SAR. Furthermore, we can calculate the SAR using the measured TFs and the simulated incident tangential electric fields, which we refer to as the predicted SAR. The SAR values were normalized to 1 W/kg for all of the tested leads, since the exposure conditions we subjected the leads to are not to be expected during a regular MR examination. These results are plotted in Figure 2.9 where we used linear regression to find the calibration coefficient (α_1) that maximizes R^2 which resulted to be equal to 0.91 at a minimum.

2.4 Discussion

Previous work has demonstrated that the TF for linear implants can be acquired with the use of MRI through the image artefact created in the RF transmit fields by the implant. However, in a typical RF safety assessment procedure, the measured TF needs to be validated too. Conventionally, the validation of the TF is performed by changing the implant trajectory within a phantom inside a birdcage body coil and measuring the temperature increase at the tip of the implant lead. This methodology has some disadvantages and is difficult to implement using the same setup as the MRI-based TF measurement. Therefore, we aim to define a validation procedure that can be incorporated into the same setup as for the MRI-based measurement of the TF, which would expedite the entire process.

The first part of the paper consists of a simulation-based study where we compare different TF validation methods. To compare the different methodologies in terms of their validation effectiveness, we used the SVD. The SVD decomposes the matrix of incident field distributions of the evaluated methods into a set of orthogonal vectors with corresponding singular values. Normalizing and summing the singular values results in the number of equivalent orthogonal incident field distributions that the method is capable of creating. The more orthogonal incident field distributions that can be created the higher the validation quality of that method.

From the simulation study, we found that shifting the phantom inside the MRI system, using dielectric pads, and wrapping the phantom in aluminium foil all are not effective in creating orthogonal incident field distributions. Using a passive RF coil is more effective, but still falls short with respect to the

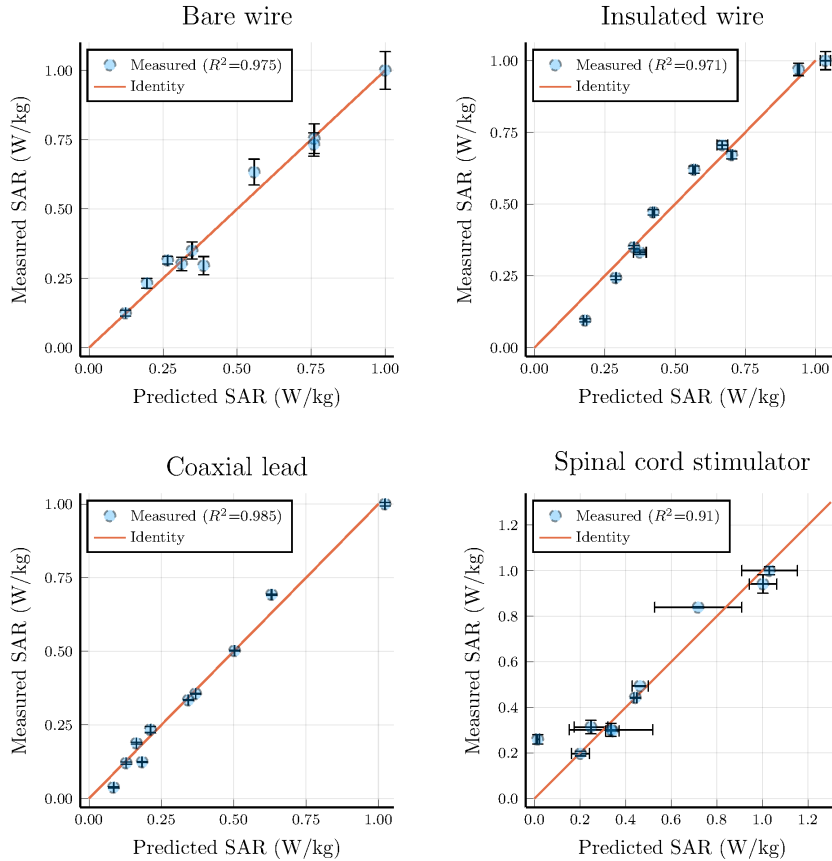


Figure 2.9: The SAR that is calculated using the transfer function and the known exposure condition correlated with the SAR that is calculated from the measured temperature curves. Six measurements were done with the small transmit coil and 4 were done with the large transmit coil for a total of 10 measurements per lead.

conventional validation method. Positioning local transmit coils at different positions along the implant trajectory has comparable effectiveness compared to changing the implant trajectory. This method has the added experimental benefit that the temperature probes stay at the same position relative to the lead tip.

From Figure 2.6, it can be observed that the singular values for the local transmit coils drop rapidly after the seventh exposure. Therefore, increasing

the number of positions along the implant trajectory will have little effect in terms of validation quality. To increase the validation quality further, a third transmit coil could be constructed that creates a spatially different electric field. A benefit, however, is that the number of temperature measurements that are required for the proposed validation is significantly fewer compared to the conventional method (i.e. nine compared to one hundred temperature measurements).

For the second part of the paper, we completed an MRI-based TF measurement and validation procedure for four elongated lead structures using the validation method that emerged as the best candidate from the simulation comparison: local transmit coils.

The validation procedure resulted in the scatter plot depicted in Figure 2.9, which shows a good correlation ($R^2 \geq 0.91$) between the measured and predicted SAR at the tip of the lead trajectory. This means that for a given incident electric field (i.e. in this case, created by local transmit coils) and the MRI-measured TF the predicted SAR is in agreement with the independently measured temperature increase. The reason we find these high coefficients of determination is a result of multiple beneficial factors compared to the conventional methodology.

The first benefit is that the used setup for the measurement of the TF is the same as the setup for the validation. The phantom, the implant position within the phantom, and its orientation are all exactly the same. Furthermore, since the implant trajectory is kept constant and straight, the implant cannot couple with itself and effectively alter the TF.

Another important experimental benefit for the presented validation method is that the relative distance between the lead tip and the temperature probe is constant since we move neither. This results in all the temperature measurements being in the same position eliminating any errors as a result of the misplacement of the temperature probe. These errors can be quite large since the gradient of the temperature elevation around the tip is very steep [30, 3]. The final major benefit of using this measurement and validation method is that only one setup is required to be built. This decreases the effort significantly and reduces the possible amount of errors that can be made.

A potential caveat to this method is that there might be coupling between the implant and the local transmit coil. This could alter the TF and induce errors during the validation. Therefore, this potential error source was investigated using FDTD simulations. We simulated the TF for the insulated copper wire with and without the local transmit coil placed next to the phantom. Negligible changes were observed between the two TFs, this is shown in Supporting Information Figure S2.

The presented validation method also contains some drawbacks. The major drawback is that the local transmit coils that are used for the validation have

to be simulated precisely to obtain the correct incident tangential electric field. Otherwise, the wrong SAR is predicted and the measured and predicted SAR might not correlate anymore. Thus any errors made in the simulation of the local transmit coils will be propagated to errors in the validation of the TF. For the loop coils, the RF fields are smooth and predominantly affected by the dimensions of the coil itself. Simulating other types of coils or antennas might be more difficult and prone to errors.

Another drawback of this validation methodology is that the coils are connected to the quadrature hybrid of the birdcage body coil. Although the procedure is not difficult, it can be a considerable obstacle for some institutes or systems. More ideal would be to have a local transmit coil with more appropriate coil interfacing. Although the method has been specifically designed to facilitate the validation of MR-based measured TFs, the validation method could also be applied outside of the MR scanner with a separate power source for the coils. Combined with a benchtop TF measurement setup, this could be a cheaper solution than using the MR system. However, depending on the setup, the phantom may need to be moved between the TF measurement and validation which could possibly displace the lead or the temperature probe.

The uncertainty depicted in Figure 2.9 shows that overall the presented method is accurately predicting the SAR at the tip of the leads. Only for the spinal cord stimulator, we see larger uncertainties arising for the measured TF. This can be a result of the more complicated structure of the implant. Another reason for the larger uncertainty is that the amount of usable data in the FFE sequence was limited because parts of the signal were corrupted by small ferromagnetic parts inside the implant. The uncertainty in the measured SAR is significantly increased when the scans used for heating were terminated prematurely or when the overall temperature increase was small.

The uncertainty analysis includes the goodness of fit for the temperature data for the measured SAR and the data uncertainty for the TF fit. The simulated electric fields, the positioning of the local transmit coils, and any model imperfections are not included. These uncertainties have been investigated in detail by Neufeld et al in where they find the uncertainty in the SAR arising from differences in conductivity, permittivity, phantom placement, and implant placement to be in the order of 5.6% [39]. Where changes in the conductivity and permittivity were varied a percent and contribute to the largest source of uncertainty. The phantom placement was varied 10mm in all three directions and the implant placement was varied 1mm in all directions. The implant placement can be equated to our local transmit coil placement since the positions are relative to each other. Therefore, the actual uncertainty depicted in Figure 2.9 is likely higher, however, these values give an impression of the accuracy of the presented methodology.

In this work, we only validated the TF of the tip of the four leads. The TFs

of other electrodes in the patch of the spinal cord stimulator can be validated using this methodology. This can be done by using the column of the TM that corresponds with the electrode location and placing a fiberoptic temperature probe at that electrode. For the TF for the RF rectification voltage at the IPG header of the spinal cord stimulator the last column of the TM should be used, however, this TF cannot be validated using this method because the temperature probes cannot be placed inside the IPG.

2.5 Conclusion

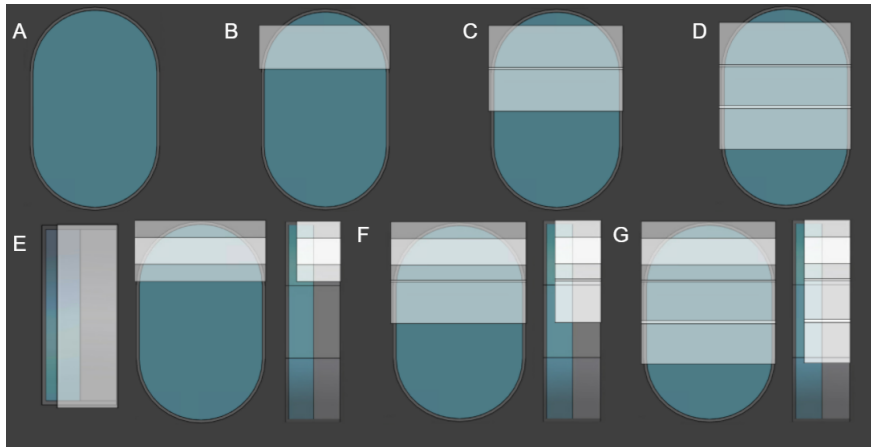
In the first part of this paper, we performed a simulation study on the effectiveness of different methods to validate the TF for linear implants. We introduced a metric to assess the validation quality/effectiveness by using the singular value decomposition. From the simulation study, we found that positioning local transmit coils at different locations along the fixed implant trajectory has a similar validation quality compared to the conventional method (i.e. changing the implant trajectory).

In the second part of the paper, we performed a TF measurement and validation study on four linear implants. Here the TF is both measured and validated using the MRI system, all in one setup. The validation was done with fiberoptic temperature probe measurements where the incident field distribution was varied by placing the local transmit coil at different positions between heating tests. We obtained a good agreement between the predicted SAR using the TF and the measured SAR, extracted from the temperature measurements. For the investigated lead structures, using linear regression, we found an R^2 of at least 0.91. The benefits of using the presented measurement and validation method are that only one setup is required, the measured TF is not altered during the validation through self-coupling of the lead, and the relative distance between the temperature probe and the lead tip is constant since neither is moved during validation.

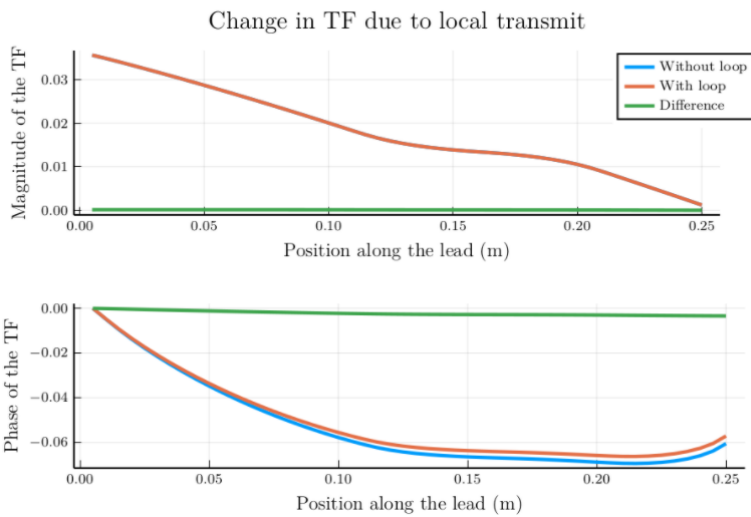
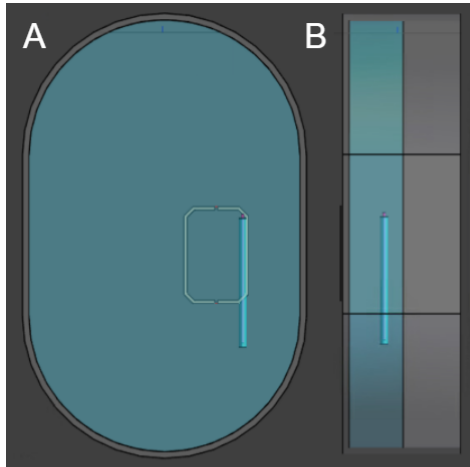
2.6 Acknowledgements

We would like to thank Dr. Ir. Jurriaan Bakker for providing medical implants that could be used for measurements.

2.7 Supporting Figures



Supporting Information Figure S1: The different setups of the aluminium foil shielding. A) shows the case without any shielding. B) & C) & D) show increasingly more aluminium foil shielding where the foil is placed once on top of the phantom and once on the bottom of the phantom. E) shows first the back of the phantom covered in aluminium foil then the top view and the side view for once simulation setup. F) & G) show the top and side view for increasingly more aluminium foil.



Supporting Information Figure S2: A) shows the top view of the simulation setup and B) shows the side view, where the local transmit coil is placed directly underneath the phantom. The TF was simulated for the setup shown in A) & B) with and without the local transmit coil present. Below the setup the magnitude and the phase of the simulated TFs are shown. Which are in good agreement, only a negligible change in the phase.

Accelerating Implant RF Safety Assessment Using a Low-Rank Inverse Update Method

*Peter R.S. Stijnman, Janot P. Tokaya, Jeroen van Gemert, Peter R. Luijten,
Josien P.W. Pluim, Wyger M. Brink, Rob F. Remis, Cornelis A.T. van
den Berg and Alexander J.E. Raaijmakers*

*Based on: P.R.S. Stijnman, J.P. Tokaya, J van Gemert, et al. Accelerating
implant RF safety assessment using a low-rank inverse update method. Magn
Reson Med. 2020; 83: 1796– 1809. <https://doi.org/10.1002/mrm.28023>*

Abstract

Purpose: Patients that have medical metallic implants, e.g. orthopaedic implants and pacemakers, often cannot undergo an MRI exam. One of the largest risks is tissue heating due to the radio frequency (RF) fields. The RF safety assessment of implants is computationally demanding. This is due to the large dimensions of the transmit coil compared to the very detailed geometry of an implant.

Methods: In this work, we explore a faster computational method for the RF safety assessment of implants that exploits the small geometry. The method requires the RF field without an implant as a basis and calculates the perturbation that the implant induces. The inputs for this method are the incident fields and a library matrix that contains the RF field response of every edge an implant can occupy. Through a low-rank inverse update, using the Sherman-Morrison-Woodbury matrix identity, the EM response of arbitrary implants can be computed within seconds. We compare the solution from full-wave simulations with the results from the presented method, for two implant geometries.

Results: From the comparison, we found that the resulting electric and magnetic fields are numerically equivalent (maximum error of 1.35%). However, the computation was between 171 to 2478 times faster than the corresponding GPU accelerated full-wave simulation.

Conclusion: The presented method enables for rapid and efficient evaluation of the RF fields near implants and might enable situation-specific scanning conditions.

Keywords: Implant Safety, RF Safety, Simulations, FDTD, Minimization Problems.

3.1 Introduction

The group of patients with medical implants that require an MRI scan is constantly growing. However, MRI scanning of a patient with metallic implants bears a potentially severe safety risk. The electromagnetic (EM) fields produced by an MRI scanner can couple to the metallic implant resulting in image degradation and serious health hazards. The largest risk is tissue heating due to the radio frequency (RF) fields. The implant can locally enhance the RF fields causing temperature hotspots [23, 40] with potentially severe consequences [24, 41]. Therefore, people with an implant are either exempted from MRI scanning or scanned with very conservative RF power limitations degrading the achievable image quality severely.

In order to quantify the risks associated with a particular implant EM simulations are often performed. These EM simulations can compute the RF fields for a given transmit coil, patient model and implant. The electrical properties, conductivity and permittivity, of both the patient [42] and implant [43, 44] affect the resulting RF fields. The geometry and location with respect to each other of the transmit coil, patient model and implant are relevant for assessing the RF fields. Finally, the drive settings for the transmit coil are required to correctly quantify the RF fields [45, 10, 46, 47, 48, 49]. The simulated RF fields are often used in thermal simulations to quantify tissue heating.

A popular method for EM simulations is the finite-difference time-domain (FDTD) method [50]. With the FDTD method a single configuration of source, patient and implant can be computed at a time. These FDTD simulations are time-consuming due to the large domain (the whole MRI RF system) that needs to be simulated, even though the implant only affects a small domain within the patient. On top of this, to obtain a conditional label for an implant with the most lenient restrictions on scanning hundredths of thousands of these simulations, for all the different possible configurations, need to be done (i.e. the tier 4 approach as specified by ISO/TS 10974:2018 [14]). For this reason, investigating RF safety for a particular implant in a patient model is a computationally demanding task. This has been demonstrated by B. Guerin et al. [20] recently for different deep brain stimulation implants. The full-wave simulation, performed with the finite element method, took up to 6 hours with 13 processors and ~ 300 GB of RAM for a single simulation. For FDTD simulations E. Cabot et al. [51] showed that similar types of simulations can take up to 43 hours for a single simulation, even with GPU acceleration.

To alleviate the computational complexity substitute models are used. One such model used for EM simulations including implants is the Huygens' box [52, 53]. This method takes a two-step approach to compute the RF fields. First, a simulation without an implant is done where the RF fields are computed and

used to construct a box around the implant. Surface currents running on the Huygens' box are computed that create the same incident RF field inside this box. After this, the implant is placed inside the Huygens' box and the surface currents found are applied, on its boundaries, to the simulation which results in the total RF fields. Everything outside of the Huygens' box is ignored in this second simulation resulting in a smaller computational domain. A challenge with this is making the Huygens' box large enough such that the scattered RF fields created due to the implant are not reflected back into the box by something that is outside of the box (i.e. there should be no crosstalk between the two domains).

Another substitute model that is applicable to elongated implants, e.g. pacemaker leads, is the electric field transfer function (TF). This transfer function describes the electric field enhancement at the tip of an elongated implant for a given incident tangential electric field exposure [16], where the incident tangential electric field is acquired by an FDTD simulation without the implant geometry present. This effectively entails that the scattered RF field due to the implant is superimposed on the incident field, thereby decoupling the concurrent simulations of transmit coil, human model and implant into concurrent simulations with only the transmit coil and human model.

The use of a TF drastically decreases the number of full-wave simulations that need to be performed. However, as mentioned before, the transfer function is only valid for elongated implants, which is a subset of a large number of different possible implants. Furthermore, the TF can only predict the electric field enhancement at the tip of the implant. The idea of the transfer function was extended to a transfer matrix in the work of J.P. Tokaya et al. [17]. The transfer matrix can predict the electric field enhancement at any location along the elongated implant, rather than only at the tip.

Although the TF enables quick calculation of the RF field enhancement due to an elongated implant, its use comes at the price of a loss of accuracy compared to a full-wave simulation. This was shown by E. Cabot et al. in [54] where it was found that there is a difference (up to 48%) between the concurrent full-wave simulation of the implant and the patient model compared to computing the response of the implant by the use of the TF.

Due to the aforementioned problems with the current methods, very long simulation times or sub-optimal accuracy of substitute models, there is a need for a new and more efficient method. Therefore, in this work, we will investigate a fast and accurate generalized methodology to do RF safety assessment for arbitrary implant geometries. This is derived from the work of J. van Gemert et al. [32] that describes a method for efficiently computing the scattered RF fields produced by dielectric pads. Here we use the same methodology for medical implants, thus, instead of computing the EM response of an object near the patient we are interested in the EM response of an object (i.e. an

implant) within the patient.

In this method, the RF fields are simulated without the implant present and the scattered RF field produced by the implant is computed and afterwards superimposed onto the incident field. The computation to include the EM response of the implant is achieved through a small domain inversion, using the Sherman-Morrison-Woodbury formula [55]. We assume that the matrix that needs to be inverted is non-singular, which is normally satisfied [32]. The inversion is computed on a much smaller domain than the initial simulations. Therefore, the effect of the implant can be computed almost instantly. Furthermore, since the simulation with the source and patient is decoupled from the implant, the electrical properties, geometry and location of the implant can easily be altered without doing another full-wave simulation, making this an efficient method for a tier 4 [14] safety assessment.

To compute the scattered RF field due to an implant, a library and the RF fields without the implant are required. The library consists of the EM response for a unitary current density for each location (i.e. voxel edge) that can be occupied by an implant, which can, for example, be simulated using the FDTD method. Computing this library is a one-time effort and once available it facilitates computing the effect of different materials (i.e. electrical properties) and locations of these implant geometries within the patient can be computed in an extremely fast manner. This decreased computational effort allows for efficient evaluation of the RF safety assessment for implants.

In comparison to existing full FDTD simulations, the presented method achieves unprecedented acceleration factors. This may enable RF safety assessment of implants at much lower costs, may benefit the design of implants and ultimately may even enable online RF safety assessment of implants.

3.2 Theory

We follow similar steps as [32] and start with the Maxwell equations, given by

$$-\nabla \times H + \sigma E + j\omega\varepsilon E = -J^{ext}, \quad (3.1a)$$

$$\nabla \times E + j\omega\mu H = 0, \quad (3.1b)$$

here H is the magnetic field, E is the electric field, σ is the conductivity, ε is the permittivity, ω is the angular frequency at the Larmor frequency, μ is the magnetic permeability and J^{ext} is the external current density, i.e. the current running through the RF coil. In an MRI environment, all materials have a magnetic permeability of $\mu \approx \mu_0$. Equations (3.1a) and (3.1b) are defined on a continuous domain. For numerical analysis the domain is typically discretized into a voxelized grid. The discretization of Equations (3.1a) and (3.1b) can be

written in matrix-vector notation as

$$(D + C^{bg})f^{bg} = -q, \quad (3.2)$$

where D contains the curl operators and C^{bg} , the electromagnetic properties matrix, contains the electrical properties and is defined as $C^{bg} = \text{diag}(c^{bg})$, where the vector c^{bg} is written as

$$c^{bg} = \begin{bmatrix} \sigma_1 + j\omega\epsilon_1 \\ \vdots \\ \sigma_k + j\omega\epsilon_k \\ j\omega\mu_1 \\ \vdots \\ j\omega\mu_l \end{bmatrix}, \quad (3.3)$$

where bg is used as shorthand notation for background, indicating that there is no implant present. The subscripts k and l indicate the number of edges and faces of the discretized domain respectively. The vector f^{bg} contains the E and H fields and q contains the external current densities. Equation (3.2) can be written more compact as

$$Af^{bg} = -q, \quad (3.4)$$

where $A = (D + C^{bg})$. Solving the field distributions for a given external current density is performed through the inversion of A

$$f^{bg} = -A^{-1}q. \quad (3.5)$$

It should be noted that A encompasses the complete simulation domain, which can be dozens of millions of voxel edges for realistic situations. Therefore, this inversion is not feasible and the fields can only be computed using numerical methods (e.g. FDTD or FEM).

However, we are now interested in a small perturbation in this A matrix created by a change in the dielectric properties, for example, due to an implant. If we were to add this implant to the simulation domain and keep the discretization the same we would need to solve

$$\begin{aligned} (D + C^{bg} + C^{imp})f &= -q, \\ (A + C^{imp})f &= -q, \end{aligned} \quad (3.6)$$

where C^{imp} contains the change in electrical properties between the newly added implant and the background. Similar to Equation (3.3) we write $C^{imp} =$

$\text{diag}(c^{imp})$, where c^{imp} is defined as

$$c^{imp} = \begin{bmatrix} \sigma_1^{imp} - \sigma_1^{bg} + j\omega(\varepsilon_1^{imp} - \varepsilon_1^{bg}) \\ \vdots \\ \sigma_k^{imp} - \sigma_k^{bg} + j\omega(\varepsilon_k^{imp} - \varepsilon_k^{bg}) \\ j\omega(\mu_1^{imp} - \mu_1^{bg}) \\ \vdots \\ j\omega(\mu_l^{imp} - \mu_l^{bg}) \end{bmatrix}, \quad (3.7)$$

where the superscript imp is used as shorthand notation for implant. This operation is equivalent to deleting the electrical properties of the background and adding those of the implant. Since the magnetic permeability of objects in an MRI should be, approximately, equal to μ_0 the bottom half of the vector in Equation (3.7) is equal to zero. Furthermore, at locations where the implant is not present the change in conductivity and permittivity is zero too. Therefore, the change in the medium property matrix is confined to a very small (low-rank) domain within the matrix A . This small domain consists of M edges whereas the entire domain on which A is defined has N edges. To

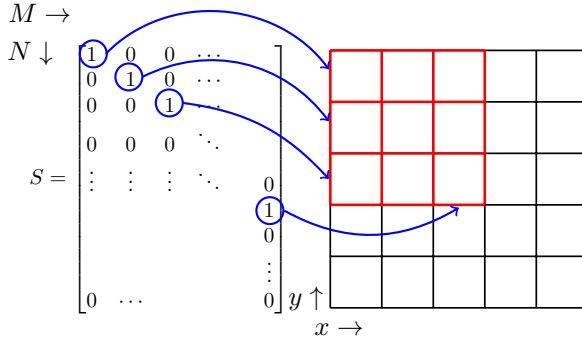


Figure 3.1: A representation of the S matrix for a 2D grid. The left shows the values inside the support matrix for the corresponding edges in the grid on the right. The red edges define the small domain while the red plus the black edges define the large domain. The blue arrows indicate to which edge in the grid each '1' corresponds to.

map quantities from this large domain to the small domain the support matrix S is introduced. The S matrix has N by M entries where,

$$S_{ij} = \begin{cases} 1, & \text{if } (x_N, y_N, z_N)_i = (x_M, y_M, z_M)_j \\ 0, & \text{otherwise} \end{cases}, \quad (3.8)$$

here i and j indicate the row and column numbers respectively. Furthermore, $(x_N, y_N, z_N)_i$ and $(x_M, y_M, z_M)_j$ describe the coordinates of the i^{th} edge within the large and j^{th} edge within the small domain respectively. Effectively, this entails that there are M nonzero entries that indicate when an edge in the large domain coincides with an edge in the small domain as shown in Figure 3.1. To go from the large domain to the small domain we use

$$S^T C^{imp} S = \tilde{C}^{imp}, \quad (3.9)$$

where \tilde{C}^{imp} now describes a diagonal M by M sparse matrix with the values of the electrical properties for each voxel edge occupied by the implant as described by Equation (3.7). To go from the small domain to the large domain we use

$$S \tilde{C}^{imp} S^T = C^{imp}. \quad (3.10)$$

Substituting Equation (3.10) in Equation (3.6) and solving for the field distributions results in

$$f = -(A + S \tilde{C}^{imp} S^T)^{-1} q. \quad (3.11)$$

Solving this still requires an inverse operation on the large domain. This is not possible for realistic simulation domains due to the number of edges in the simulation domain. However, there is a matrix identity that allows us to rewrite this equation to our advantage. This is called the Sherman-Morrison-Woodbury matrix identity [55] and is given for Equation (3.11) by

$$f = -A^{-1} q + A^{-1} S (I_M + \tilde{C}^{imp} S^T A^{-1} S)^{-1} \tilde{C}^{imp} S^T A^{-1} q, \quad (3.12)$$

where I_M is an M by M identity matrix. We will now introduce a new matrix called the library matrix Z

$$Z = -A^{-1} S. \quad (3.13)$$

This matrix is an N by M matrix where every column is the field response for a unitary current density of the corresponding edge in the support matrix S . This matrix needs to be simulated before computing the response of any implant. Building the library matrix poses an extensive simulation effort, M numerical simulations need to be performed. However, each separate simulation converges quickly because there is only a single edge source present. The library only needs to be computed once for a given dielectric background environment (e.g. for a specific patient model). After this, the response of any arbitrary implant can be calculated almost instantly.

Now substituting Equation (3.5) and Equation (3.13) into Equation (3.12) we obtain

$$f = f^{bg} + Z (I_M - \tilde{C}^{imp} S^T Z)^{-1} \tilde{C}^{imp} S^T f^{bg}. \quad (3.14)$$

Note that the inverse in this equation only needs to be computed on the small domain. This allows the computation of the E and H to be possible with this methodology. From Equation (3.14) two key points can be observed. The first is that the total field is the sum of the two different RF fields, the incident fields and a field that is dependent on the scatterer (i.e. the implant). The second is that a generalized form of the transfer matrix [17] is defined within this equation. This can be seen when realizing that the library matrix, Z , has to be multiplied by the scattered current density within the implant. Furthermore, we can observe from Equation (3.1a) that the conductivity and permittivity, the quantities we are changing, are only multiplied by the electric field within f^{bg} . Therefore, the terms in between Z and f^{bg} must be equivalent to the transfer matrix. This point is explained in more detail in Section 3.7. The generalized transfer matrix can help provide insight into what implant characteristics significantly influence the scattered RF field. The above mentioned key points show another way of looking at how and why this low-rank inverse computation works and more specifically which electromagnetic quantities affect the total RF field.

Within Equation (3.14) all the interactions between the electric field components and the resulting current density are defined. Whereas the transfer matrix only uses the E_z^{inc} component of the electric field and results in only the I_z component of the current [17]. This generalized transfer matrix could compute the current running on any arbitrary implant for any incident electric field.

3.3 Methods

In order to compute the scattered RF field created by an implant using the presented method a simulation with the transmit coil and patient model is required (i.e. the implant is not present). The RF field computed in this simulation represents the incident/background RF field, f^{bg} . Further, the library matrix, Z , needs to be computed. The columns of the library matrix represent the RF fields on the edges in the large domain for a unitary current density, $J = 1A/m^2$. All the edges that can be occupied by the implant need to be simulated. Therefore, constructing the library matrix requires a considerably large set of simulations. The described inputs have been computed using an FDTD software package (Sim4Life, ZMT, Zurich, Switzerland).

To validate the method a separate simulation is performed with the transmit coil, patient model and implant present. This simulation will produce the total electric and magnetic fields, f , which are compared to the total fields produced by the computation performed with the presented method. Three different implant structures are used to test the method. The first represents an orthopaedic surgical implant: a metallic screw. The geometry of the or-

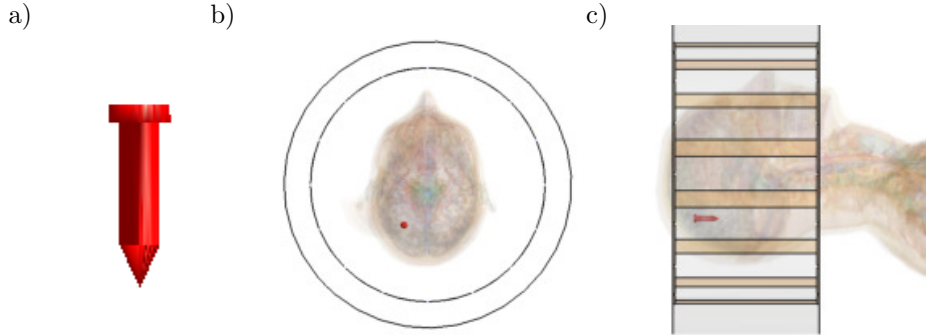


Figure 3.2: The geometry and location of the passive implant inside Duke. a) The model of the orthopaedic implant used inside Duke. b) A transverse slice of Duke inside the birdcage coil showing the position of the orthopaedic implant. c) A sagittal slice of Duke inside the birdcage coil showing the position of the orthopaedic implant.

thopaedic screw is shown in Figure 3.2a, while the location with respect to Duke and the birdcage coil in the transverse and sagittal plane are shown in Figure 3.2b and Figure 3.2c respectively. The second implant resembles a deep brain stimulator (DBS) lead structure and the third is a DBS lead structure that is tilted with respect to the FDTD grid axes. Both of these DBS lead structures are shown in Figure 3.3.

The FDTD simulations for the passive implant are simulated at 128MHz (3T) and for the DBS implants the simulations were done at 298MHz (7T). For all implant types, the convergence level of the simulation with and without implant was set at -50dB, while the library matrix simulation had a convergence level of -30dB.

The simulations for all three implants were calculated on a 1mm isotropic grid. The orthopaedic screw was simulated with a conductivity of $2.38 \cdot 10^6 S/m$, the conductivity of titanium, and a relative permittivity of 1. The DBS electrode consists of two different materials, a conductive lead and an insulation layer around the lead. For the lead $2.38 \cdot 10^6 S/m$, and $\epsilon_r = 1$ was chosen, while for the insulation material the electrical properties were chosen to be $\sigma = 0 S/m$ and $\epsilon_r = 4$.

The computations for the FDTD simulations were calculated using a GPU, NVIDIA TITAN X. The update was performed with the Julia programming language [56] using a CPU, Intel Xeon E3-1270 v5 (@ 3.60 GHz), and 64GB of RAM available. To solve the inverse in Equation 3.14 the generalized minimal residual method (GMRES) was used.

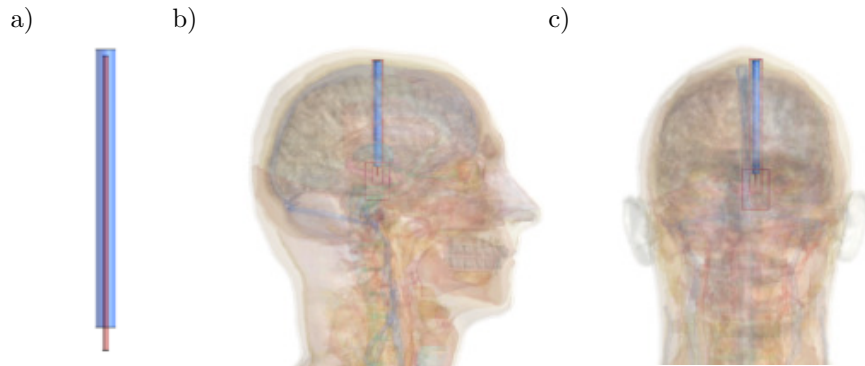


Figure 3.3: The geometry and location of the DBS lead inside Duke. Duke's position inside the birdcage coil is the same as for the setup with the orthopaedic implant. a) The model of the DBS lead used inside Duke. b) A sagittal view of Duke showing the position of the DBS lead. c) A Coronal view of Duke showing the position of the DBS lead.

As a sanity check that GMRES finds the correct solution, we look at the physical interpretation of the solution of the system $Ax = b$ in our case. As shown in Appendix A the solution of our system, x , is the scattered current density given by

$$J^{sc} = (I_M - \tilde{C}^{imp} S^T Z)^{-1} \tilde{C}^{imp} S^T E^{inc}. \quad (3.15)$$

However, we can also write the scattered current density, per definition, as

$$\begin{aligned} J^{sc} &= (\sigma^{imp} - \sigma^{bg} + j\omega\epsilon_0(\epsilon_r^{imp} - \epsilon_r^{bg})) E^{tot}, \\ &= C^{imp} E^{tot}. \end{aligned} \quad (3.16)$$

When written in this form the scattered current density can be computed using quantities from the FDTD simulations for the incident and total RF fields.

3.4 Results

To validate the presented method we compare the results from Equation (3.14) with the simulation from the FDTD solver when the implant is present. For the orthopaedic screw, the results are shown in Figures 3.4 and 3.5 for the E and H fields respectively. In both figures, the magnitude of the x, y, z components of the fields is shown. Furthermore, error plots are shown where we defined

Table 3.1: Maximum error percentage in E and H fields for the passive and DBS electrode.

Field Component	orthopaedic screw	straight DBS electrode	tilted DBS electrode
E_x	0.05%	1.23%	0.57%
E_y	0.04%	1.29%	0.45%
E_z	0.04%	1.25%	0.47%
H_x	0.67%	1.06%	0.26%
H_y	0.62%	1.16%	0.23%
H_z	1.35%	0.37%	0.31%

the error between FDTD fields and the fields as computed by Equation (3.14) as

$$Err = \frac{|f_{FDTD} - f_{inv}|}{max(f_{FDTD})} \cdot 100\%, \quad (3.17)$$

where f_{FDTD} and f_{inv} are substituted for the x, y, z components of the E and H fields, f_{FDTD} are the fields obtained from the FDTD solver, whereas f_{inv} denotes the RF fields obtained from the inverse computation. The error is scaled by the maximum value in the field, rather than the local field value. This was performed to suppress errors in regions where the magnitude of the fields are very small (e.g. inside the implant). Otherwise, these small deviations inside the implant would result in large error values although they are of minor concern because the peak values in the electric field contribute significantly more to the heating of the tissue. The ratio between the peak value of the electric field and the electric field inside the implant is a few orders of magnitude. In Table 3.1 the maximum errors as computed by Equation (3.17) are shown. For the DBS electrodes, the magnitude of the E and H fields are shown in Figures 3.6 and 3.7. Again the maximum errors, as defined by Equation (3.17), are shown in Table 3.1. Between the three different implants shown we find that the range of the maximum errors is given by 0.04% to 1.35%. In Table 3.2 we compare the dimensions of the problem and the computation time for the FDTD method and the inverse computation. Here the number of edges in the entire domain for the FDTD simulation is given. Furthermore, the number of edges that the implants consist of is shown. This determines both the dimensions of the square matrix that needs to be inverted according to Equation (3.14) and the number of columns of the library matrix. The computation time, i.e. on the GPU, per column for the library matrix and the total computation time are also given. Finally, the computation times for both methodologies are given together with the acceleration factor. The latter is defined as

$$Acc = \frac{t_{FDTD}}{t_{inv}} \quad (3.18)$$

Table 3.2: Comparison computation time, t , between the FDTD method and the inverse computation.

	orthopaedic screw	straight DBS electrode	tilted DBS electrode
Total edges FDTD	$3.1 \cdot 10^6$	$9.9 \cdot 10^6$	$9.9 \cdot 10^6$
N	$1.3 \cdot 10^5$	73032	73032
M	3804	8794	6583
length (z)	3 cm	9 cm	8cm
RAM Z	8GB	9GB	9GB
t_{FDTD} for one column of Z	20 s	15 s	15 s
t_{FDTD} of Z	21.1 hrs	36.6 hrs	27.4 hrs
t_{FDTD} (CPU)	14760 s	22790 s	23441 s
t_{FDTD} (GPU)	3420 s	2414 s	2483 s
t_{inv} (CPU)	1.38s	14.1 s	6.8 s
Acceleration (CPU)	10696	1616	3423
Acceleration (GPU)	2478	171	362
Break even point	22.2	54.9	53.2

With Acc as the acceleration factor, t_{FDTD} as the computation time for the FDTD simulation (using either the CPU or GPU) and t_{inv} for the proposed inverse updating method (CPU based), without the calculation of the library matrix and incident field included. The acceleration factor that is found between the two methods is between 2478 and 171 times faster for the proposed method. This acceleration in simulation time entails that the break even point (BEP) of simulations, meaning that using the proposed method with its corresponding precomputation step is as fast as FDTD, when 22 and 55 simulations are done for the case of the first and second implant respectively. When more implant geometries/locations with varies incident field exposures are required, which for implant safety assessment standards is certainly the case, the proposed method is faster than FDTD. The BEP is calculated as,

$$BEP = \frac{t_{FDTD} \text{ of } Z}{t_{FDTD}(\text{GPU}) - t_{inv}} \quad (3.19)$$

Finally, to show that the minimization process finds the correct solution of the system the scattered current density is computed for both implant geometries according to Equations 3.15 and 3.16. The current density is summed for all the transverse slices (xy -plane) of the implant to make the plots readable. The result is shown in Figure 3.8, where it is clearly seen that the minimization process finds the correct solution, i.e. the blue and black line are directly on top of each other and the difference between them is two orders of magnitude smaller than the actual magnitude of the current density.

3.5 Discussion

This work has demonstrated an alternative approach to calculate the RF field response of a medical implant in an MRI. As an input, the method requires

the incident RF field distribution (RF field without an implant present) and a library consisting of the unitary current density response of every voxel edge on the discretized implant geometry. To demonstrate the validity of the method, the method is tested for a screw and a deep brain stimulator lead where the input fields are determined by FDTD simulations.

From the maximum errors shown in Table 3.1 it is clear that this methodology is very accurate. The accuracy is subject to the numerical precision of the supplied incident, library fields, and the convergence level of the GMRES solver. This is further substantiated by the results shown in Figures 3.4 to 3.8, where the RF fields and scattered current densities computed by the presented method are shown to be almost equivalent to those computed by the FDTD method.

One major difference between the presented method and the Huygens' box is that the reduced domain in the presented method is only as large as the implant itself, whereas with the Huygens' box the reduced domain should be large enough that there is no crosstalk between the full and reduced domain.

Due to the nature of the inverse computational complexity, $\mathcal{O}(M^3)$, the acceleration factor for this method is dependent on the number of edges that the implant occupies. Therefore, the larger the number of edges the implant occupies the longer the simulation time becomes. This occurs when either the implant size is increased or if the discretization is performed on a finer grid. This is also shown in [32] and can be observed by Table 3.2. The computation time of the inverse, however, is independent of the frequency of the RF fields and the voxel size, i.e. geometric resolution, while FDTD simulations are dependent on these properties. This means that very small implants on a very fine grid would require a precomputation step, i.e. computing the library matrix and incident fields, that is slower while computing the EM response of the implant will be equivalently fast for a similar number of edges that need to be updated.

Another, potentially more restricting factor is the memory requirement. The library matrix grows linearly with the number of edges. For the orthopaedic implant given here the library matrix is already 4GB for the electric fields (and another 4GB for the magnetic fields, however only the electric fields are needed for the computation). On top of this, the memory requirements for the inversion that needs to be computed grows with the square of the number of edges the implant occupies, i.e. 0.1 GB for the orthopaedic implant in this work and 0.6 GB for the DBS electrode. Therefore, while theoretically possible, in the current state of the presented method it would be difficult to compute the response of highly realistic lead structures. Both due to the large structure of such an implant and the high resolution required to capture all the details, i.e. the helical lead structure. This would increase the simulation time for the incident field and the library matrix. The resulting matrices required

for our method would become too large, both M and N grow cubically with the factor increase in resolution. The memory requirements of the library matrix and the inverse scale with N by M and M by M respectively, i.e. with the 6th power of the factor increase in resolution. We are currently investigating ways to decrease the memory requirements for the presented method. Some of the ideas are discussed below. The current setup and implementation of the presented method would serve well for orthopaedic implants which usually are not tested for RF safety and are either smaller in size or can be modelled on a coarser grid.

To tackle the previously mentioned memory problems we could approximate the library matrix, Z , by exploiting two properties to introduce sparsity into the library matrix. First, the presented method involves the simulation of a full library matrix, while simulations of current density sources that are spatially located near each other have very similar EM responses due to the equivalent dielectric surrounding. Second, the magnitude of the RF fields decays very rapidly for increasing distances away from the source location. This implicates that the value of the current density at any edge of the implant is dominated by the edges that are located close to it. By either interpolating between columns of the library matrix or truncation of the data if the magnitude becomes too small (i.e. adaptive cross approximation [57, 58]), sparsity can be introduced into the library matrix at the cost of the accuracy of the computation. These and other alterations for improved performance will be investigated in subsequent studies.

Assuming that the limitations described above can be addressed sufficiently, the presented method bears strong potential for applications in RF safety assessment of implants in MRI, since the calculation time of the RF fields is now in the order of seconds. One example is the safety assessment of implants according to the ISO/TS 10974 technical specification. The output of this technical specification is a conditional label for the implant that specifies the maximum $B_1^{+,rms}$ and/or other RF power-related settings a patient with the particular implant can safely undergo an MRI examination. For the most rigorous RF safety assessment level (tier 4) of this technical specification concurrent simulations of the implant, patient and transmit coil are required for a wide variety of potential implant locations and trajectories. Although this method will result in the least restrictive scanning constraints, it is often considered too demanding. With the presented method, the field response of every voxel edge in the domain only needs to be calculated once, after which the RF field distribution for any potential lead wire trajectory can be computed almost instantly. This may greatly reduce the workload for tier 4 safety evaluations of implants, given that we have access to a library of different RF field exposures and the libraries of different human models.

Another application could be to predict the local RF field enhancement

prior to MRI examination of the patient. The implant structure and location could be revealed by the help of previously acquired X-ray photos of the patient. After the implant is localized a quick RF field calculation could be performed based on pre-calculated RF field distributions, both for the incident fields and the library matrix, using generic body models. This calculation would result in a situation-specific power threshold by which the overestimation is reduced to a minimum. This could possibly be achieved for implants without a conditional label, the RF safety assessments could be performed beforehand to verify if a patient with such an implant can safely undergo an MRI exam.

3.6 Conclusion

In this work, we have shown a new methodology for RF safety assessment of implants in an MRI setting without assumptions on the implant geometry or composition. With appropriate simulations done beforehand, the presented method can perform the RF safety assessment in a greatly accelerated fashion compared to full-wave simulations, e.g. FDTD.

The incident fields when no implant is present and a library matrix, containing the EM response of every edge the implant can possibly occupy, need to be precomputed. Afterwards, the effect of any arbitrarily shaped and positioned implant, with arbitrary material properties, can be calculated within seconds. The result of the computation is numerically equivalent to the solution of a full-wave simulation. For the implants shown in this work the maximum error was 1.35%. However, using this method a significant acceleration is obtained (a factor 171 to 2478 compared to GPU accelerated FDTD simulations). This is excluding the calculation of the library matrix and the incident RF field.

3.7 Generalized Transfer Matrix

A generalized form of the transfer matrix as described in [17] can be extracted from Equation (3.14). The transfer matrix relates the current in an elongated implant (i.e. a lead wire) with the incident electric field according to

$$I = ME^{bg}, \quad (3.20)$$

where M is the transfer matrix. The first column of the transfer matrix is the transfer function as defined in [16]. There are two limitations of these concepts: the first is that TFs are only defined for elongated, linear implants. The second is that they only relate an E_z^{bg} to an I_z . In an MRI setting this part of the electric field is the main contributor to I_z (which in turn is also the main contributor to the total current I). However, the x - and y -components

of the electric field also contribute to the total current that will run on the elongated implant.

The transfer matrix can be obtained from Equation (3.14) by observing that the library matrix consists of the field responses per unitary current density for each edge of the implant. This implies that to obtain the RF fields produced by the implant a multiplication with the current density at each edge of the implant is needed, which is thus given by

$$(I_M - \tilde{C}^{imp} S^T Z)^{-1} \tilde{C}^{imp} S^T f^{bg} \equiv J^{sc}. \quad (3.21)$$

Where J^{sc} is the current density at each edge of the implant. From Equation (3.1a) we observe that the dielectric properties in C^{imp} are only multiplied by the electric field in f^{bg} and not the magnetic field (i.e. there is no change in μ_r). This entails that we can write Equation (3.21) as

$$J^{sc} = (I_M - \tilde{C}^{imp} S^T Z)^{-1} \tilde{C}^{imp} S^T E^{bg}, \quad (3.22)$$

Further we know that the element-wise multiplication of the area with the current density results in the current as shown by

$$I = a \circ J, \quad (3.23)$$

where a is the area of each edge, as defined by the Yee Cell [50], of the implant. Using Equation (3.20) it is now evident that

$$M = a \circ \left((I_M - \tilde{C}^{imp} S^T Z)^{-1} \tilde{C}^{imp} S^T \right). \quad (3.24)$$

3.8 Acknowledgement

This work is part of the research programme "Safety threat or measurement device? Using the MRI scanner to assess RF safety of implanted medical devices in MRI." with project number 15739, which is (partly) financed by the Netherlands Organisation for Scientific Research (NWO).

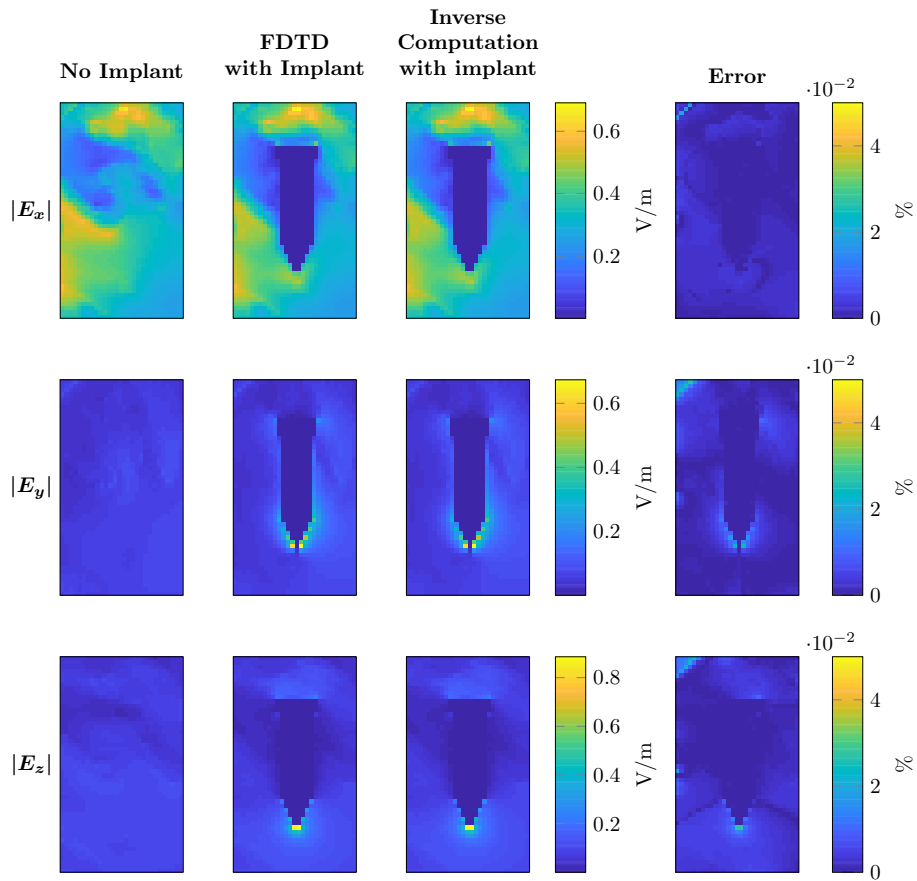


Figure 3.4: Comparison of the electric field components obtained by FDTD and the proposed inverse computation method from a surgical screw. The three rows show the magnitude of the $E_{x,y,z}$ components respectively. The first column shows the magnitude of the electric field if there is no implant present. The second column shows the electric fields with the implant present computed by the FDTD method. For the same implant, the third column shows the output of the computations performed with the presented methodology. The last column shows the error percentage as computed by Equation (3.17).

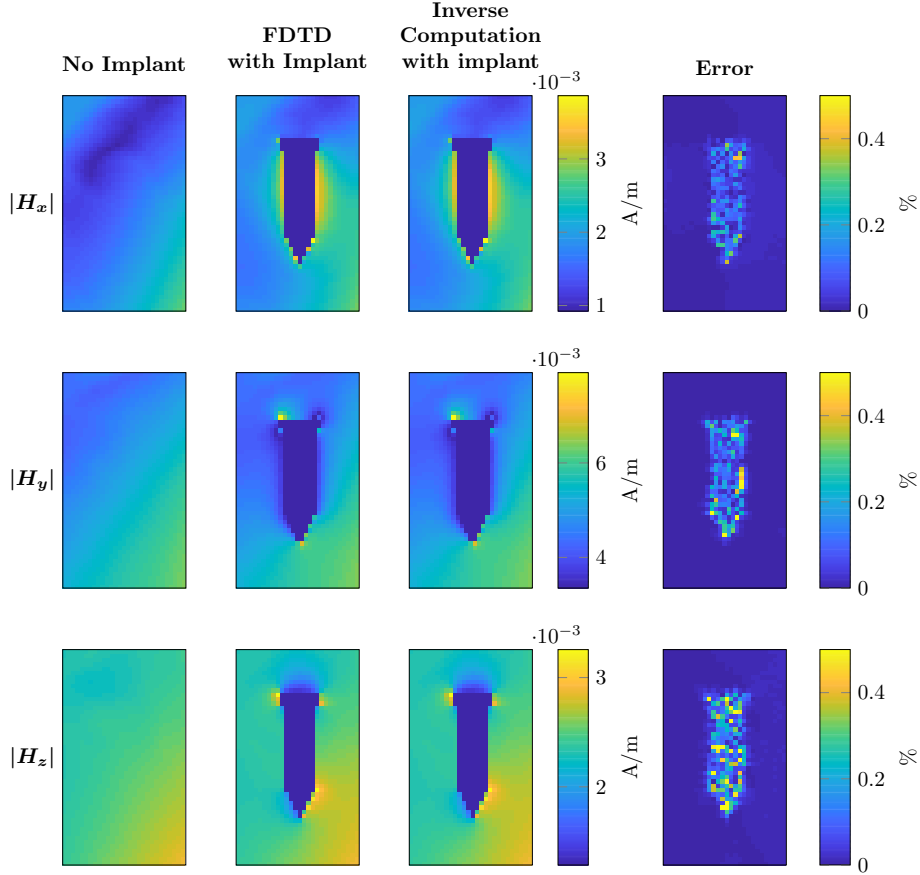


Figure 3.5: Comparison of the magnetic field components obtained by FDTD and the proposed inverse computation method from a surgical screw. The three rows show the magnitude of the $H_{x,y,z}$ components respectively. The first column shows the magnitude of the magnetic field if there is no implant present. The second column shows the magnetic fields with the implant present computed by the FDTD method. For the same implant, the third column shows the output of the computations performed with the presented methodology. The last column shows the error percentage as computed by Equation (3.17).

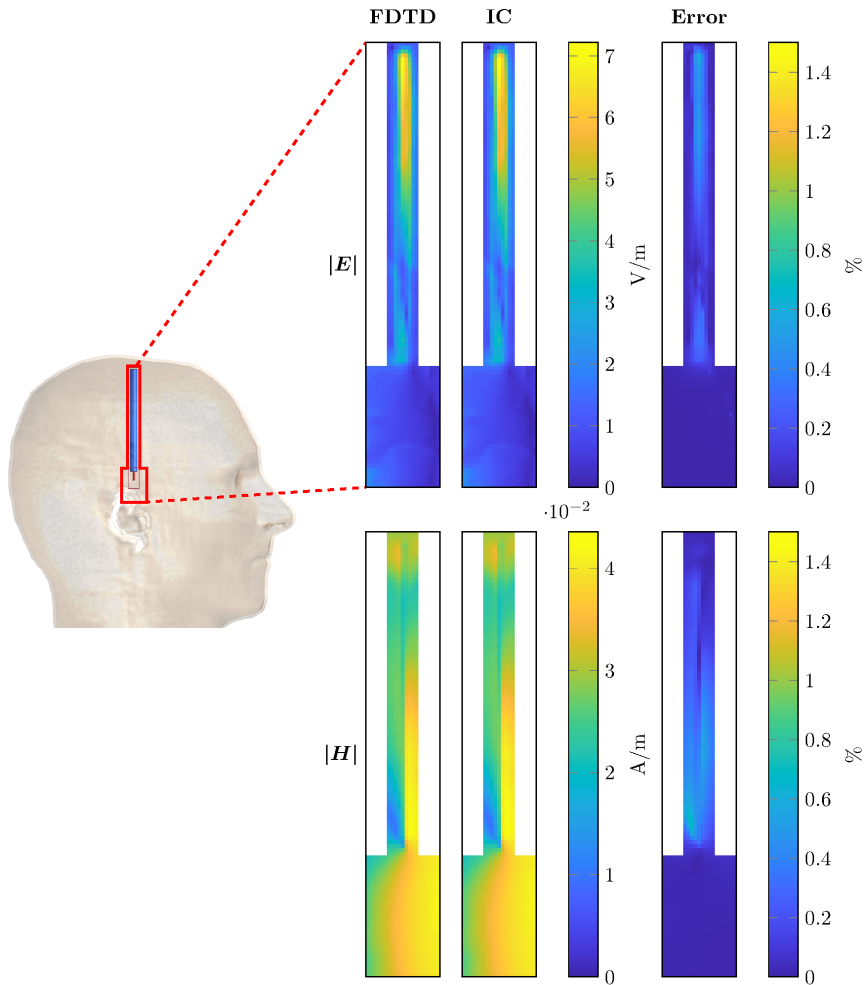


Figure 3.6: Comparison between the RF fields computed with the FDTD and the presented method for the straight deep brain stimulator lead (aligned with grid axes). On the left, the location of the computed domain within the model is indicated with a red contour. The top row of figures shows the magnitude of the electric field for the FDTD simulation, the inverse computation and the error percentage as computed by Equation (3.17). Equivalent plots are shown for the magnetic field in the bottom row.

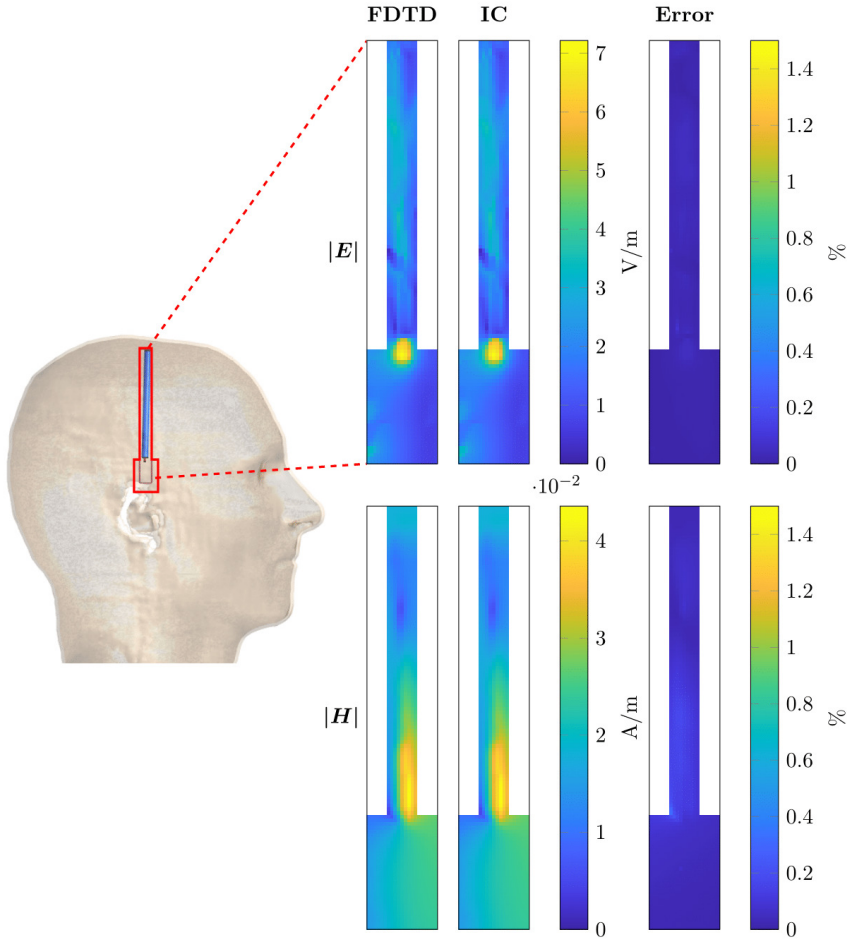


Figure 3.7: Comparison between the RF fields computed with the FDTD and the presented method for the tilted deep brain stimulator lead (not aligned with grid axes). On the left, the location of the computed domain within the model is indicated with a red contour. The top row of figures shows the magnitude of the electric field for the FDTD simulation, the inverse computation and the error percentage as computed by Equation (3.17). Equivalent plots are shown for the magnetic field in the bottom row.

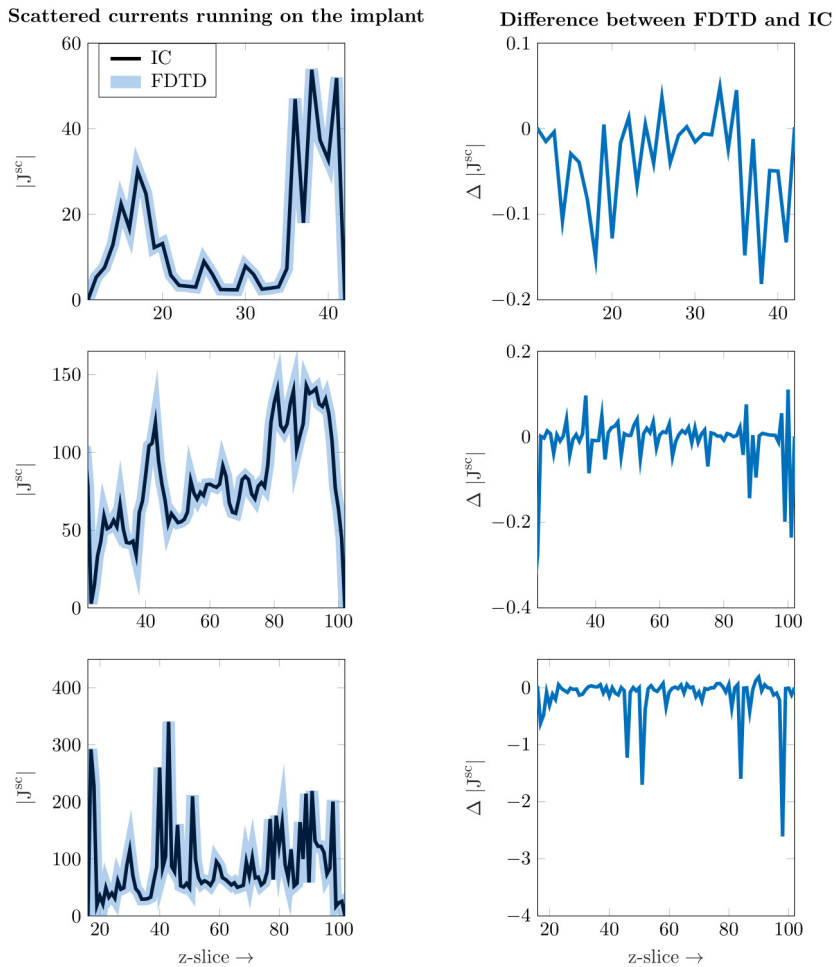


Figure 3.8: Comparison between the true solution, as computed by Equation (3.16), and the solution found by the inverse computation, as defined by Equation (3.15). The current density is summed for the transverse (xy -plane) slices. The top row shows the result for the orthopaedic implant and the second row shows the result for the straight DBS implant and the bottom row shows the result for the tilted DBS lead.

A Perturbation Approach for Ultrafast Calculation of RF Field Enhancements near Medical Implants in MRI

Peter R.S. Stijnman, Bart R. Steensma, Cornelis A.T. van den Berg and Alexander J.E. Raaijmakers

Based on: P.R.S. Stijnman, B.R. Steensma, C.A.T. van den Berg and A.J.E. Raaijmakers. A perturbation approach for ultrafast calculation of RF field enhancements near medical implants in MRI. Sci Rep 12, 4224 (2022). <https://doi.org/10.1038/s41598-022-08004-7>

Abstract

Patients with medical implants often are deprived of magnetic resonance imaging examination because of safety risks. One specific risk is the enhancement of the radiofrequency fields around the medical implant potentially resulting in significant tissue heating and damage. The assessment of this enhancement is a computationally demanding task, with simulations taking hours or days to converge. Conventionally the source of the radiofrequency fields, patient anatomy, and the medical implant are simulated concurrently. To alleviate the computational burden, we reformulate a fast simulation method that views the medical implant as a small perturbation of the simulation domain without the medical implant and calculates the radiofrequency fields associated with this perturbation. Previously, this method required an extensive offline stage where the result is intractable for large simulation domains. Currently, this offline stage is no longer required and the method is completely online. The proposed method results in comparable radiofrequency fields but is orders of magnitude faster compared to standard simulation technique; the finite-difference time-domain, the finite-sums, and the finite element methods. This acceleration could enable patient-specific and potentially online radiofrequency safety assessment.

4.1 Introduction

Magnetic resonance imaging (MRI) is one of the main medical imaging modalities and has become indispensable for diagnosis, treatment planning, and patient follow-up studies. The number of people requiring an MRI examination is steadily increasing every year as can be seen in Figure 4.1 [59]. This is in part because of the excellent soft-tissue contrast provided by this imaging modality. Based on the principle of nuclear magnetic resonance, MRI requires three types of magnetic fields: a permanent strong magnetic field (1.5 or 3 T), rapidly switching magnetic gradient fields for spatially encoding the signal, and radiofrequency (RF) fields generated by an RF coil or antenna to excite the atomic nuclei to create the signal. This multitude of magnetic fields poses a severe safety risk for patients with medical implants. Also, this patient category is rapidly growing. For example, from Figure 4.1 b) and c) it can be observed that the number of hip and knee replacement, and the number of pacemakers (PMs) and implantable cardioverter-defibrillators (ICDs) surgeries is increasing annually [60, 61, 62, 63]. Both MRI investigations and medical implants are more prevalent in the aging population; it is estimated that 50-75% of patients with PMs and ICDs will require an MRI within the lifetime of the device [13].

Patients with medical implants can be excluded for an MRI examination because of the many safety concerns that exist when introducing metal inside the MRI environment [3, 5, 22]. The safety concerns include displacement, malfunctioning, and heating of the medical implant all of which can harm the patient under examination [23, 25, 64]. This has occurred in a handful of instances with detrimental outcomes [24, 65, 66, 67, 68]. Furthermore, in the USA alone around 300 cases of adverse events involving MRI and medical implants are reported to the FDA annually [69]. When these patients are scanned, extra precautions have to be taken; an individual risk-benefit analysis, extra monitoring and experienced physicians are mandatory, and an informed consent by the patient is required. Since a lot of smaller hospitals either do not have the equipment or the experience these patients are often referred to another hospital or not scanned at all.

To avoid depriving patients of the diagnostic capabilities of MRI, implant manufacturers have been developing increasingly more products that are MRI-compatible. To facilitate this, implant manufacturers, MRI vendors, and the scientific community have set up a technical specification for passive implanted medical devices like surgical plates or vascular stents; ASTM F2182 [15], and for active implanted medical devices like pacemakers or neurostimulators; ISO/TS 10974 [14]. Depending on the results of the prescribed tests and simulations included in this technical specification, an implant can obtain a label stating it is MRI safe, MRI conditional, or MRI unsafe. When a med-

ical implant is labeled, MRI conditional limitations are placed on the MRI sequence parameters (e.g. maximum RF power). These limitations decrease the image quality and/or increase the required scan time. One particularly

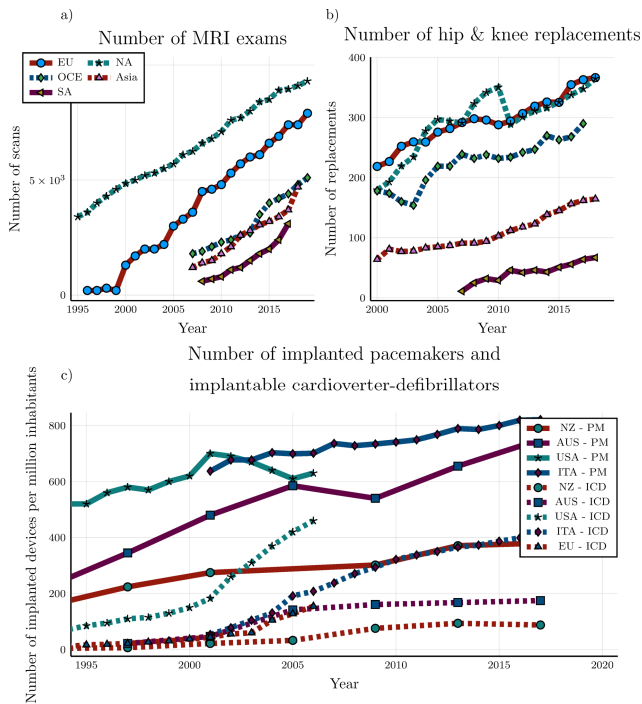


Figure 4.1: a) The number of MRI scans performed per 100.000 inhabitants. b) The number of hip and knee replacements per 100.000 inhabitants. Data presented for the 21 indicated countries (OECD (2021), Magnetic resonance imaging (MRI) exams (indicator). <https://data.oecd.org/healthcare/magnetic-resonance-imaging-mri-exams.htm> (Accessed on 01 August 2021)). c) The number of implanted pacemakers (PM) and implantable cardioverter-defibrillators (ICD) per 1 million inhabitants in the indicated countries [60, 61, 62, 63].

demanding and challenging safety aspect of this technical specification is the RF safety testing. The RF fields that are generated during an MRI examination can induce currents in metallic implants which are excellent conductors. The induced currents cause charge accumulation at the interfaces between the implant and the tissues surrounding the implant. The charge accumulation creates conservative electric fields in those tissues and thereby enhances the

RF electric field. This enhancement creates locations where the temperature is drastically increased, potentially causing tissue burns inside the patient or even excessive brain damage [24].

The potentially dangerous enhancement of the electric field can be calculated using for example finite difference time domain (FDTD) or finite element method (FEM) simulations. The electric field inside the patient results in power deposition because of the conductivity of the tissue. The amount of dissipated power is expressed by the local specific absorption rate (SAR), which is the power deposition divided by the mass density of the tissue.

To correctly assess the RF safety of a medical implant a wide variety of patient anatomies [42] and RF coils [10, 45, 46, 47, 48, 49] should be simulated. Furthermore, the location of the medical implant inside the patient anatomy and the patient position within the RF coil are important factors for the SAR increase. A single simulation can take up to hours or even days to converge even with GPU acceleration [20, 51]. Therefore, the RF safety assessment of implants is typically done using simplified scenarios because the full analysis of every possible combination of patient anatomy, implant location inside the patient, patient position inside the scanner, and RF coil (so-called Tier 4 approach in ISO/TS 10974 [14]) is computationally too demanding.

These simplified scenarios are overly conservative to ensure safety and therefore often result in medical implants being conditionally safe. However, the resulting scanning constraints are for the largest patient group overly conservative because these constraints are determined for the worst-case scenario. This entails the worst implant position inside the patient in the worst position in the scanner while having the worst-case patient anatomy. Therefore, if the patient-specific RF interaction of the implant could be characterized before the patient arrives for their MRI examination, these conservative scanning constraints could be relaxed for the vast majority of patients. Furthermore, when the characterization of the RF interaction can be done within the time span of a few minutes the RF safety assessment could be performed online at the scanner. In addition, subject-specific RF safety assessment could make the large group of patients that carry non-labeled or multiple implants eligible again for MRI examination. Currently, the simulation process for RF safety assessment is too slow to be performed before a patient is scheduled for an MRI examination.

In previous work, a method has been described to accelerate the simulation process significantly [70, 71]. In this method, if the RF field distribution without the implant is known, the introduction of the implant into the setup can be considered a small perturbation of the system. We consider a perturbation small if it does not perturb the source of the RF fields (i.e. the RF coil). The RF field distributions arising from this small perturbation can be calculated on the small domain where the implant is present in comparison

to the entire simulation domain including the RF coil and patient anatomy. This method requires an extensive offline precomputation stage dependent on the frequency, patient anatomy, and location of the implant. Afterward, the method can calculate the RF fields within the small domain where the problematic heating will occur in mere seconds compared to hours using standard simulation techniques.

The proposed method bears some resemblance to the Tier 3 approach in the ISO/TS 10974 [14] which uses the transfer function, together with the RF field distribution without the implant present. The transfer function is a simplified model of the electromagnetic interaction of the implant with the electric RF field distribution along the implant. Furthermore, the transfer function as in the ISO/TS 10974 is only defined for elongated implant such as pacemaker leads. For three-dimensional implants using the Tier 3 approach is not feasible, whereas the proposed method is.

Unfortunately, the proposed method cannot be used practically. The result of the offline precomputation stage requires such an excessive amount of memory storage that the maximum calculable size of the implant is rather small. For example, when a human head model, with average dimensions of 15.2 cm by 18.6 cm by 11.2cm (i.e. from top of the head down to the eyes), is discretized on a 1mm isotropic resolution this would require around 650 TB of memory to store all the simulated field distributions in single precision complex float numbers. Furthermore, using an FDTD solver running on a single GPU would take almost 3 years to complete, at 10 secs per simulation [71].

In this work, a rigorous adaptation of the earlier method is presented by which the drawbacks of the previous method are overcome [70, 71]. The result is an ultrafast calculation method of RF field enhancement by medical implants in MRI. The presented method is fast enough to be used for patient specific and/or online RF safety assessment. This would improve image quality and/or reduce scan time for most implants with a conditional MRI safety label. Apart from the patient specific and online possibilities for RF safety assessment, the presented method also enables RF field calculations for the highest standard of RF safety assessment (Tier 4 in ISO/TS 10974) in a significantly accelerated fashion.

Although the method has been developed for MRI implant safety assessment, it is suitable for any application area where electromagnetic simulations (EM) are being used. If a calculated EM field distribution is perturbed by a small change in the simulation domain, the presented method allows for an unprecedented calculation speed of the new field distribution, without the need for an extensive offline precomputation stage.

4.2 Results

First, the proposed calculation method is presented. In Figure 4.9 a visual overview of the prior methodology is shown. For more detail, the derivation of this method is described in the Methods section. Subsequently, the RF field distribution for four common medical implants is calculated using the proposed method and compared to a full FDTD simulation.

4.2.1 Theory to circumvent the offline calculation

In this work, we will start from the equation given in [70, 71] that describes a perturbation of the RF fields as a result of a medical implant, given by

$$f = f^{bg} + Z(I - \tilde{C}^{imp} S^T Z)^{-1} \tilde{C}^{imp} S^T f^{bg}, \quad (4.1)$$

here f and f^{bg} contain the electric and magnetic RF fields concatenated in a vector of length N , where N is the number of edges inside the simulation domain, when the implant is and is not present respectively. I is the identity matrix of size M by M , where M is the number of edges the implant occupies inside the discretized simulation domain (i.e. the size of the implant). The electric properties and the location of the implant are defined by \tilde{C}^{imp} (M by M) and S^T (M by N) respectively. The last matrix, Z , is the so-called library matrix that by definition contains the RF field distributions of a source, $J = 1A/m^2$, within the patient anatomy. Each column, z , inside the library matrix corresponds to a source located at a single edge indicated by the column of the support matrix S according to

$$Z = [z_1, \dots, z_M], \quad (4.2)$$

where the columns are N elements long. The original method prescribes computing this library matrix beforehand by use of numerical simulations which results in unmanageable memory requirements and precomputation times, as mentioned in the introduction. In addition, the resulting matrix Z is patient anatomy-, discretization-, and frequency-specific.

To tackle the issues of memory constraints and precomputation times, we propose an alternative procedure that circumvents the requirement of the library matrix entirely. This is achieved by solving the matrix inversion in Equation (4.1) using a matrix-free approach. To explain the method, we take a closer look at the actual calculation procedure. To efficiently solve the matrix inversion in Equation (4.1) the minimization problem

$$\min_x \|b - Ax\|_2^2, \quad (4.3)$$

where $A = I - \tilde{C}^{imp} S^T Z$ and $b = \tilde{C}^{imp} S^T f^{bg}$ is solved. The variable x for which we minimize represents the scattered current density as a result of the

introduced implant. Equation (4.3) is iteratively minimized, therefore, during the minimization procedure the matrix A is not explicitly required, and only the matrix-vector product A with an estimate of x is required. Not having A explicit would reduce the memory constraints by approximately a factor M . Thus, if there is a function $g(x) = Ax$ that does not require A to be explicit, then Equation (4.3) can also be reformulated as

$$\min_x \|b - g(x)\|_2^2. \quad (4.4)$$

To find this function we start with working out the matrix-vector product according to

$$\begin{aligned} g(x) &= Ax, \\ &= (I - \tilde{C}^{imp} S^T Z)x, \\ &= x - \tilde{C}^{imp} S^T Zx. \end{aligned} \quad (4.5)$$

Here \tilde{C}^{imp} , S^T , and x are known and only the matrix-vector product of Zx is not readily available. To obtain the result of Zx we first substitute Equation (4.2) into this matrix-vector product

$$\begin{aligned} Zx &= z_1 x_1 + \dots + z_M x_M \\ &= \sum_{j=1}^M z_j x_j. \end{aligned} \quad (4.6)$$

Here it can be observed that Zx is the superposition of the unit current density field distributions in Z scaled with the present estimate of the current density distribution defined by x . These field distributions can efficiently be calculated using the volume integral equation method (VIE). The generated electric field (E^t) as a result of a source located within the patient anatomy can be expressed using the VIE method as an incident electric field (E^{inc}) generated by the source in a vacuum and a scattered electric field (E^{sc}) as a result of the patient anatomy following

$$E^t(\rho) = E^{inc}(\rho) + E^{sc}(\rho), \quad (4.7a)$$

$$E^{inc}(\rho) = -i\omega\mu_0 \left(I + \frac{1}{k_b^2} \nabla \nabla \cdot \right) \int_{\rho' \in bg} G(\rho - \rho') J(\rho') dV, \quad (4.7b)$$

$$E^{sc}(\rho) = \left(I + \frac{1}{k_b^2} \nabla \nabla \cdot \right) \int_{\rho' \in bg} G(\rho - \rho') C^{bg}(\rho') E^t(\rho') dV. \quad (4.7c)$$

Note that we follow antenna theory here and in literature on the RF safety of implants the terminology for the electric fields is different [72, 73]. The magnetic permeability and wavenumber in vacuum are denoted by μ_0 and k_b ,

ρ is the position vector, C^{bg} contains the dielectric properties of the patient anatomy, dV is the volume of a single voxel, and the free-space Green's function (G) is given by

$$G(\rho - \rho') = \frac{e^{-ik_b(\rho - \rho')}}{4\pi|\rho - \rho'|}. \quad (4.8)$$

When equations (4.7b) and (4.7c) are substituted into Equation (4.7a) the resulting equation can be solved for E^t . To solve for the superposition found in Equation (4.6) we set $J = Sdiag(x)S^T$, which is equivalent to setting all the sources in the superposition on at once with the current density distribution found in x . Here $diag(x)$ creates a matrix of size M by M with x on the main diagonal. This results in

$$Zx = \sum_{j=1}^M z_j x_j = \sum_{j=1}^M E_j^t(\rho) x_j = \sum_{j=1}^M (E_j^{inc}(\rho) + E_j^{sc}(\rho)) x_j, \quad (4.9a)$$

$$\sum_{j=1}^M E_j^{inc}(\rho) x_j = -i\omega\mu_0 \left(I + \frac{1}{k_b^2} \nabla \nabla \cdot \right) \int_{\rho' \in bg} G(\rho - \rho') Sdiag(x) S^T(\rho') dV, \quad (4.9b)$$

$$\sum_{j=1}^M E_j^{sc}(\rho) x_j = \left(I + \frac{1}{k_b^2} \nabla \nabla \cdot \right) \int_{\rho' \in bg} G(\rho - \rho') C^{bg}(\rho') \sum_{j=1}^M E_j^t(\rho') x_j(\rho') dV. \quad (4.9c)$$

Here when equations (4.9b) and (4.9c) are substituted into Equation (4.9a) we arrive at the remarkable position that we can solve for the unknown Zx without explicitly having to calculate Z . Now the function that replaces Zx for the matrix-free minimization is given by

$$\begin{aligned} \min_{Zx} \left\| -i\omega\mu_0 \left(I + \frac{1}{k_b^2} \nabla \nabla \cdot \right) \int_{\rho' \in bg} G(\rho - \rho') Sdiag(x) S^T(\rho') dV - \right. \\ \left. Zx + \left(I + \frac{1}{k_b^2} \nabla \nabla \cdot \right) \int_{\rho' \in bg} G(\rho - \rho') C^{bg}(\rho') Zx(\rho') dV \right\|_2^2. \end{aligned} \quad (4.10)$$

This enables us to solve Equation (4.4) without having to compute the massive library matrix Z . A schematic visualization of the proposed innovation to the prior method is shown in Figure 4.10.

4.2.2 Simulation results for different medical implants

To verify the correctness of the proposed method, we compare the resulting RF field distributions with those obtained from a traditional FDTD simulation. Four different medical implants are included, where we vary the patient anatomy, implant location, discretization, and the MRI field strength/frequency.

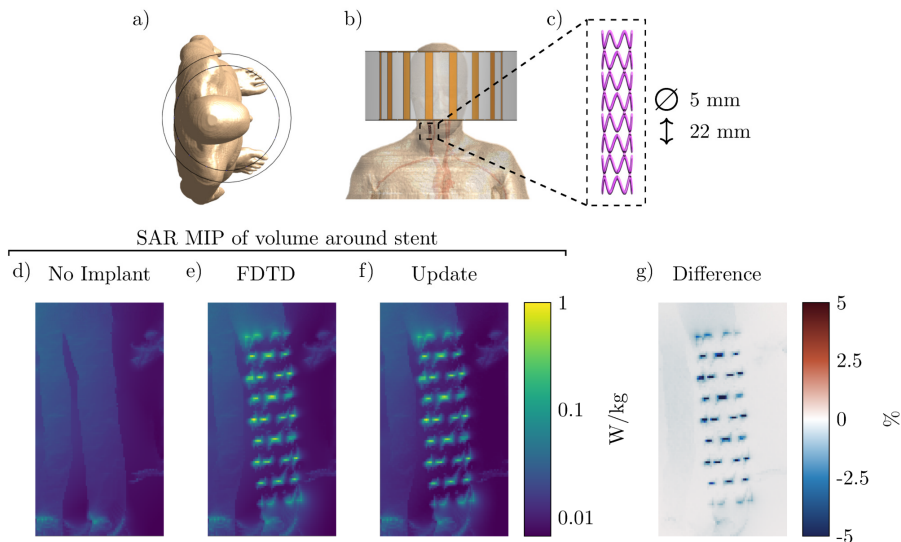


Figure 4.2: Proposed method applied to calculate the SAR increase for a carotid stent. a) & b) Transverse and coronal view of the simulated setup, respectively. c) The model of the simulated stent. d) Maximum Intensity Projection (MIP) of the local SAR without implant. e) & f) The MIPs of the local SAR with the implant present using the FDTD and the proposed method respectively. g) The MIPs of the difference between the FDTD and the proposed method.

The first implant geometry that we evaluate is a vascular stent placed in the carotid artery where the patient model is placed inside the MRI environment for a head scan at 3 T (128 MHz). The setup and the resulting maximum intensity projections (MIP) of the local SAR distribution can be observed in Figure 4.2. Note that the stent causes a 20-fold increase in the peak local SAR. Furthermore, we can observe that the MIP SAR distribution found by the proposed and the FDTD method correlate very well and there is only a small underestimation by the proposed method, as can be seen in the difference distribution in Figure 4.2 g. The FDTD simulation for this implant took 4 hours to run on a GPU while the proposed method took only 96 seconds (150 times faster). A total of 200 iterations was required to minimize Equation (4.4) at 0.475 seconds per iteration and 1 sec was required for the calculation of the scattered electric field. The next implant for which we test our method is an orthopedic implant placed to hold together the ulna after a fracture. Resulting SAR distributions for a scan at 1.5 T (64 MHz) are shown in Figure 4.3.

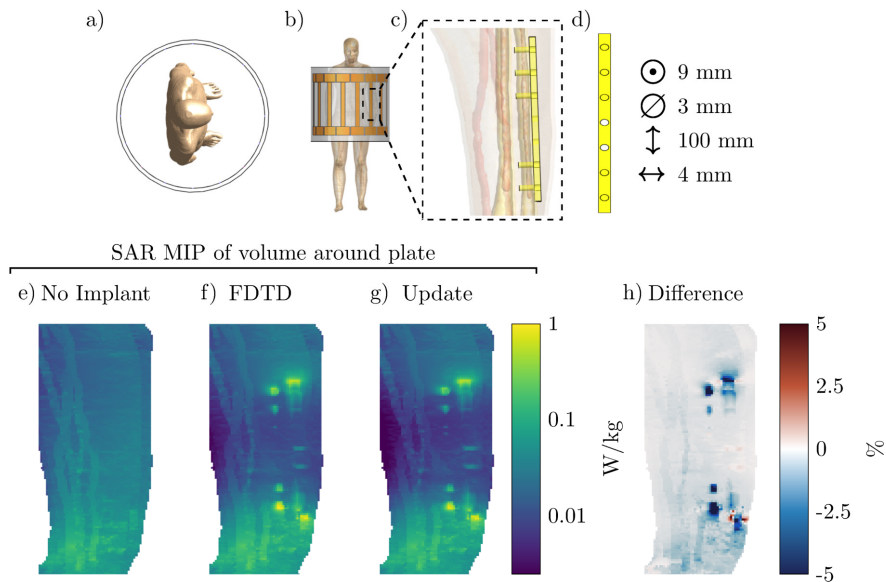


Figure 4.3: Proposed method applied to calculate the SAR increase for an orthopedic plate with screws. a) & b) Transverse and coronal view of the simulated setup, respectively. c) & d) The model of the simulated orthopedic implant. e) The MIP of the local SAR without implant. f) & g) The MIPs of the local SAR with the implant present using the FDTD and the proposed method respectively. h) The MIPs of the difference between the FDTD and the proposed method.

Again, we observe an increase in the peak local SAR values as a result of the implant being present inside the simulation (a 4-fold increase). Furthermore, the MIPs of the SAR distribution from the proposed and the FDTD method correlate well. Here we find both a small under and overestimation of the SAR distribution for the proposed method. For this implant, the FDTD simulation took 3 hours and 26 minutes to converge while it only took 28.2 seconds using the proposed method (438 times faster). A total of 150 iterations was required to minimize Equation (4.4) at 0.185 seconds per iteration and 0.5 sec was required for the calculation of the scattered electric field. The third implant setup that we simulated is a double hip implant at 1.5 T (64 MHz) for which the setup and MIPs of the SAR distributions are shown in Figure 4.4. For this configuration, we observe that there is almost no increase in the SAR values around the implants themselves. Furthermore, the error distribution of

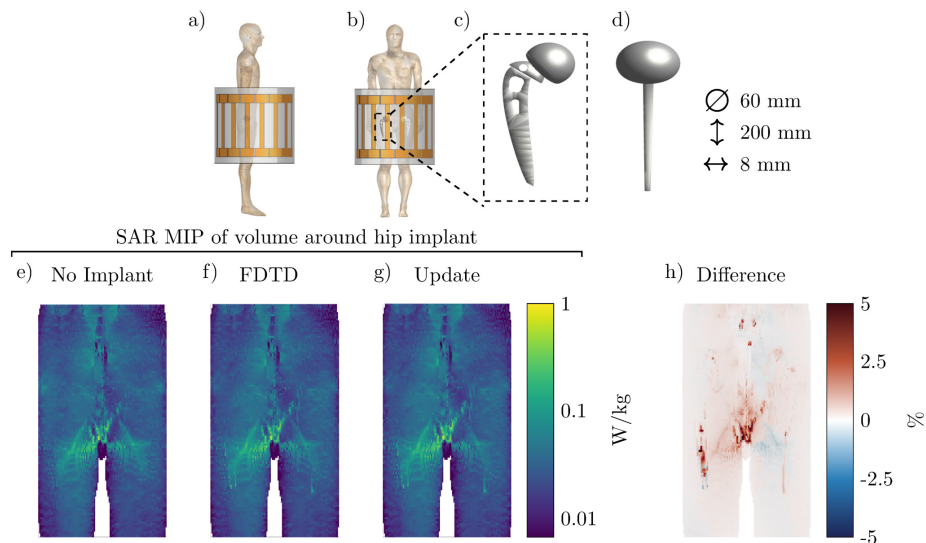


Figure 4.4: Proposed method applied to calculate the SAR increase for a double hip implant. a) & b) Sagittal and coronal view of the simulated setup, respectively. c) & d) The model of the simulated hip implant. e) The MIP of the local SAR without the hip implant. f) & g) The MIPs of the local SAR with the implant present using the FDTD and the proposed method respectively. h) The MIPs of the difference between the FDTD and the proposed method.

the MIP found by the proposed method is smaller compared to the other two simulated setups. The proposed method has converged within 194 s while the FDTD simulation took 3 hours, (55 times faster). A total of 250 iterations was required to minimize Equation (4.4) at 0.772 seconds per iteration and 1 sec was required for the calculation of the scattered electric field. While the presented method has been developed for the RF safety assessment of medical implants in combination with MRI, it is not limited to this field of research. In fact, Equation (4.10) can be solved for any dielectric background, C^{bg} (i.e. not necessarily a patient), or frequency to fit other problem statements. Some examples are computing the change in the power deposition by EM exposure between a standard model and a subject-specific model, the induced SAR by mobile telephones for models with cochlear implants (an example of which is shown in Figure 4.5), or any other EM simulation problem where there are sparse changes between simulations. For these other applications, the acceleration factor that is acquired will vary, depending on the size of the update and the domain size reduction. For the cochlear implant, the FDTD

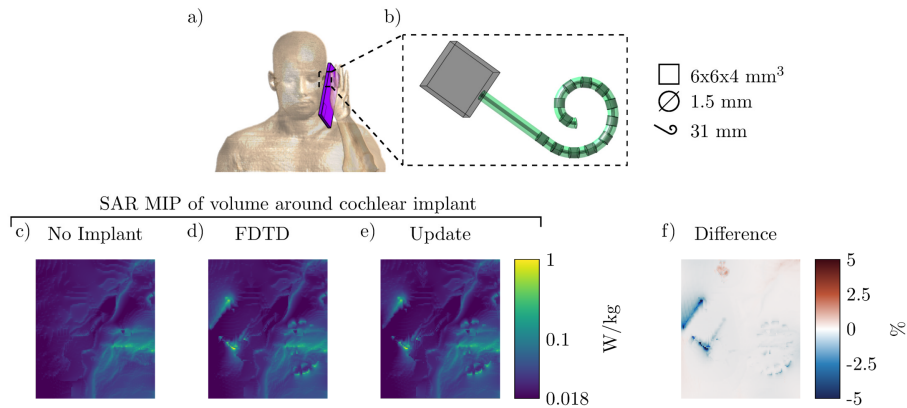


Figure 4.5: Proposed method applied to calculate the SAR increase for a cochlear implant when using a mobile phone. a) the Ella model with a mobile telephone. The antenna is at the bottom of the phone and operates at 900 MHz. b) the cochlear implant inside the Ella model. The implant has 12 electrodes and the lead is 31 mm long with a diameter of 1.5mm. c) The MIP of the local SAR without the cochlear implant. d) & e) The MIPs of the local SAR with the implant present using the FDTD and the proposed method respectively. f) The MIPs of the difference between the FDTD and the proposed method.

simulation took 23 minutes and 26 seconds while the proposed method took 66 seconds (21 times faster). A total of 150 iterations was required to minimize Equation (4.4) at 0.436 seconds per iteration and 0.5 sec was required for the calculation of the scattered electric field. For the investigated cases, the proposed method is orders of magnitude faster, as depicted in Figure 4.6. However, it should be stated that, although the proposed method is faster in many scenarios, the improvement will not be realized for particularly large domains. This is because the proposed method and the reference method scale differently with the problem size. The FDTD simulation scales linearly with the number of voxels within the simulation domain and scales inversely with the smallest voxel within the simulation domain. For the proposed method, the computation time required is more complex. The time required to solve Equation (4.1) is predominantly used to compute the matrix inversion. The time complexity of this is at worst $\mathcal{O}(M^3)$ where M is the length of the solution, in our case, this is the number of edges for which the dielectric is changed (i.e. the size of the implant).

As a result, in Figure 4.6 an indication of the expected acceleration of the proposed method compared to the FDTD method is shown as a function of the domain size. In Figure 4.6 b) the acceleration factor is calculated when the smallest voxel size is kept constant. Figure 4.6 c) indicates the acceleration when the number of voxels in the total FDTD simulation is increased by increasing the resolution. Because the smallest voxel size is decreased, FDTD characteristics dictate that the simulation time is increased, and the acceleration factor obtained with the proposed method is increased too. Figure 4.6 shows that at a very large domain size where the implant is present (i.e. M/x -axis in the plot the FDTD method will be faster than our proposed method.

4.3 Discussion

In this work, we have shown that it is possible to significantly accelerate the calculation of the RF field enhancement that is associated with a medical implant in MRI, without extensive precomputations or excessive storage requirements. This is achieved by using a matrix-free minimization scheme where we use a surrogate function based on the VIE method to replace the intractable so-called library matrix. The local SAR distributions that are obtained using the proposed method are in good agreement with those acquired with a traditionally used FDTD solver.

The acceleration of the proposed method compared to FDTD is obtained by regarding the implant as a perturbation to the original system where the RF field distribution is known. As such, only the effect of the implant on the RF field distributions is calculated.

Using the proposed method, it would be possible to perform patient-specific RF safety assessment for patients with MR conditional implants. The MR conditional label assumes a worst-case scenario which for most MRI examinations would be exceedingly conservative. From the proposed method patient-specific scanning restrictions can be derived to ensure safety while also remaining efficient with the MRI scan time. Furthermore, this method could also be used to assess the RF safety for patients with non-labeled implants. This would allow this patient group to be eligible for MRI examination again, given that the implant is MRI safe on all other aspects. We envision this by using a library of human models and obtaining the implant location from X-ray images acquired prior to the MRI exam and using that information to construct the support matrix S . Using this information the SAR near the implant can be calculated for multiple body models and positions of the implant to ensure the SAR increase is not underestimated. Moreover, as a result of the acquired acceleration, we believe that the proposed method is fast enough to enable RF safety assessment online at the MRI scanner. Finally, another application of

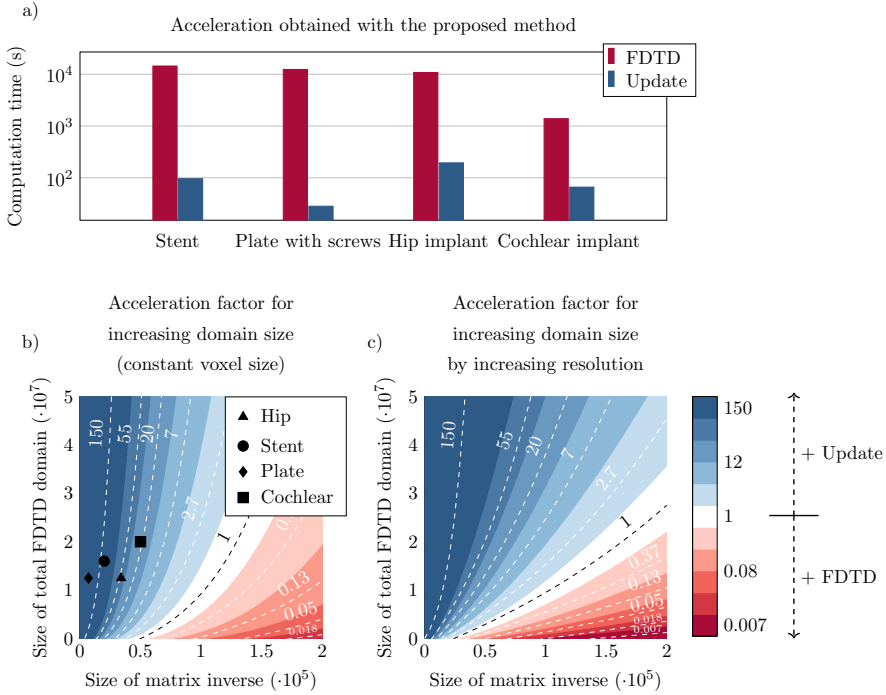


Figure 4.6: a) Acceleration obtained with the proposed method over the standard FDTD method for the four implants that have been tested. b) Acceleration of the proposed method in comparison to traditional FDTD simulation as a function of the domain size when the voxel size in the FDTD simulation is kept constant. The x-axis of the plot shows the size of the matrix to be inverted (small domain). The y-axis displays the size of the total FDTD simulation domain. To offer perspective on realistic problem sizes, the domain sizes of four implants that are investigated in this work are indicated by markers. c) Acceleration gained with the proposed method as a function of the domain size, however, now the size of the FDTD domain is increased by increasing the resolution. A blue color indicates the proposed method is faster while a red color indicates the FDTD method is faster.

the proposed method is the so-called Tier 4 RF safety assessment described in the ISO/TS 10794. The accelerated fashion in which the RF field distributions can be calculated will significantly impact the time required for a Tier 4 simulation study.

The acceleration that is found in Figure 4.6 also depends on the dimensions of the integrals in equations (4.9b) and (4.9c). The fast Fourier transform (FFT) that is performed to efficiently calculate the integrals is computed on a domain size around the implant rather than the entire simulation domain. This FFT domain size will significantly impact the acceleration that is found. The time required for the calculation of the FFTs dominates the time required for the proposed method to converge. Therefore, the proposed method is not efficient when the changes in the dielectric (M) are dispersed around the simulation domain (N). When the updates inside the domain are dispersed it could be more efficient to apply the proposed method multiple times and apply the update in steps. As an example, the double hip implant update could also be performed in two steps, first the left hip implant and afterward the right hip implant. This would however ignore the interaction that these implants may have on each other. From Figures 4.2, 4.3, and 4.4 it can be observed that the proposed method slightly underestimates the local SAR values. The first reason for the mismatch in the local SAR is that not the entire patient anatomy is considered in the integrals of the proposed method; interaction between the implant and more distant tissue is neglected. For the implants in this manuscript this source of error was minimized by increasing the domain of the FFTs until no decrease of the mismatch between FDTD simulations and the proposed methods were observed. The second reason is that any changes in the current on the RF coil (or J^{source}) as a result of a change in loading because of the implant are not included in the proposed method. However, for the investigated implants the RF fields arising from the model perturbation approach zero magnitude at the location of the RF coil. The final reason for a mismatch between the proposed method and the FDTD simulation is that there are inherent differences between the FDTD and VIE methods [74, 75]. While the VIE method has been adapted to closely resemble the FDTD method, by having the same Yee cell discretization and dielectric averaging, the method for solving the RF fields is still different and could explain the found underestimation. As for the distribution of the error, only 0.5% of the voxels inside the calculated domain had a larger underestimation than 5% with a maximum of 18% underestimation, this can also be observed in Figure 4.7. For our intended application, this is not problematic since the calculated SAR values are on a voxel basis, while all the regulations for MRI implant safety prescribe a 1 g averaged SAR value. Applying such an averaging on the results will decrease the maximum underestimation, as can be observed in Figure 4.8. From the MIPs of the differences, it can be observed

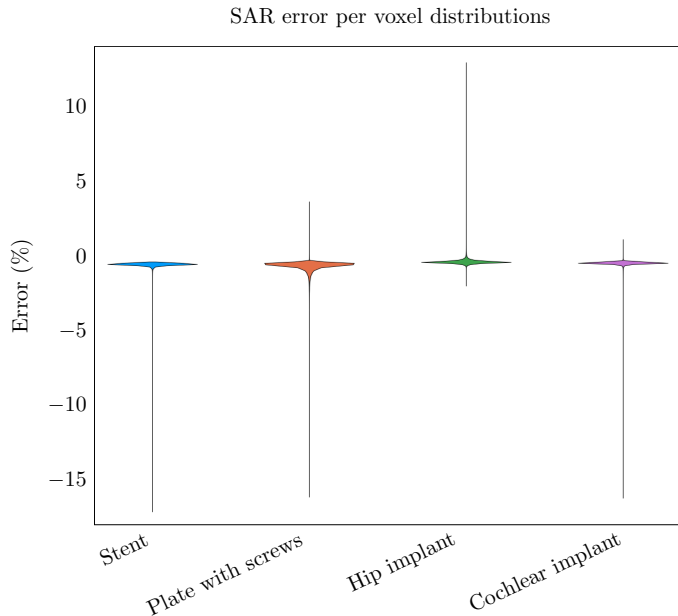


Figure 4.7: The percentage error distribution for every voxel around the implant. The violin plots show the distribution of the error per implant. A positive error is an overestimation of the proposed method and a negative error is an underestimation.

that the underestimation is decreased significantly compared to the pointwise differences. In this work, we have reformulated the update method as described in [70, 71] to no longer require the offline stage, and is now completely online. This entails that given an electromagnetic field without an implant present the effect of the implant on the electromagnetic field can be calculated. The proposed method is demonstrated for multiple implants where we show that the calculated RF fields are comparable to the RF fields obtained with FDTD simulations. Using the proposed method we obtain a speed up between 55 and 438 times. Therefore, the proposed method could be used for patient-specific RF safety assessment or an ISO/TS 10974 Tier 4 approach.

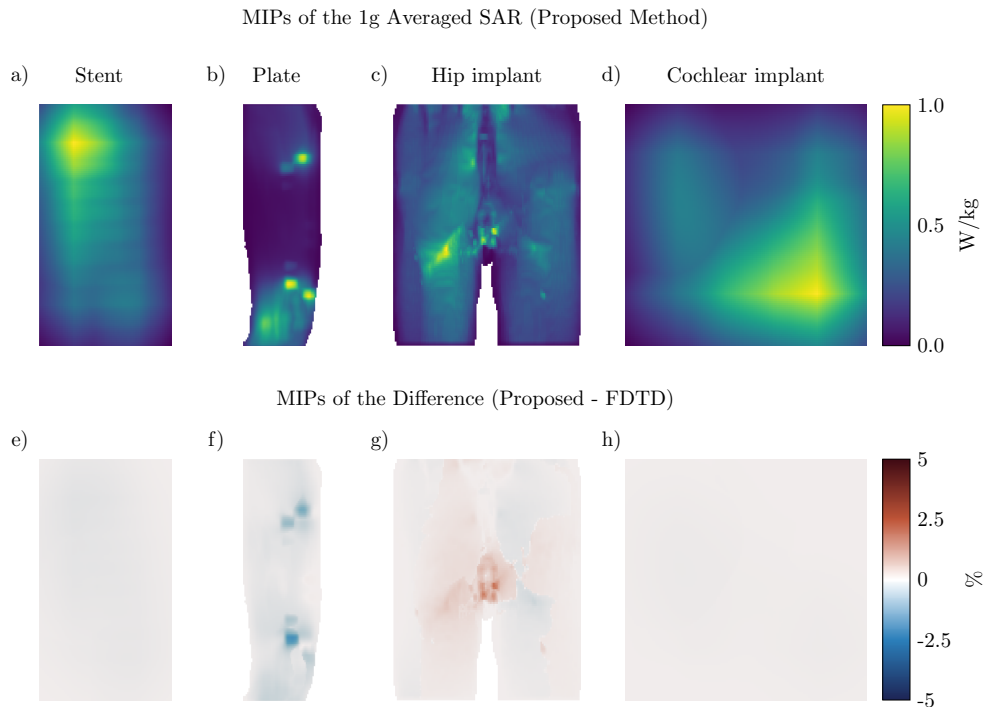


Figure 4.8: The MIPs of the 1 g averaged SAR obtained with the proposed method (a till d) and MIPs of the difference between the proposed method and the FDTD simulations (e till h). a) For the stent. b) For the plate with screws. c) For the hip implant. d) For the cochlear implant. e) shows the MIP of the difference for the stent. f), g) & h) show the same for the plate with screws, hip implant, and the cochlear implant respectively.

4.4 Methods

4.4.1 Simulation details

The proposed method has been implemented in the Julia programming language [76] and predominantly uses the existing software packages: `CUDA.jl` [77] and `IterativeSolvers.jl`. The software has been developed into a new package that can be used by others, details are in the code availability section.

To find the solution to Equation (4.4) we use a generalized minimal residual (GMRES) method. Multiple solvers have been tested, but GMRES proved to be the most stable and the fastest solver for the problem. For solving

Equation (4.10) we use the conjugate gradient squared method because it was the fastest solver to obtain the correct solution. Furthermore, the integrals in equations (4.9b) and (4.9c) are computed efficiently using 2 FFT operations and a multiplication rather than a convolution which decreases the number of operations from $\mathcal{O}(N^2)$ to $\mathcal{O}(N \log(N))$. This can be performed when the Green's function is calculated for a homogeneous dielectric background (i.e. a scalar value for k_b , vacuum in our case) and the resolution is uniform, note that we do take into account the inhomogeneous dielectric of the patient anatomy using this formulation with the variable C^{bg} in Equation (4.9c).

To benchmark our method we use the commercial FDTD package Sim4Life v5.0 (ZMT, Zurich, Switzerland). Furthermore, the body models of Ella and Duke from the virtual family (IT'IS, Zurich, Switzerland) are used.

For each comparison, we simulated a setup without and with the medical implant present. The simulation without the medical implant served as the input RF field distribution for our proposed method, while the simulation with the implant was used to compare the RF field distributions. The medical implants were modeled after standard implant geometries using XCoreModelling within the Sim4Life environment. The metal parts in all implants are modeled as titanium.

In the first comparison, the stent was placed in the carotid artery of the Ella model. The stent is 22 mm long and has a diameter of 5 mm. The thickness of the wires that make up the stent is 0.5 mm. The birdcage head coil that is used has a 155 mm radius, a leg length of 168 mm, a leg width of 20 mm, and the endrings are 2.5 mm wide. The RF shield around the coil has a 190 mm radius and a length of 173 mm. The stent was discretized using a 0.25 mm isotropic resolution and the rest of the setup was automatically discretized by Sim4Life for a total of 15.5 million voxels inside the simulation domain.

For the second comparison, the plate with screws is placed onto the ulna of the Ella model, with the screws going through the bone. The length of the plate is 100 mm long, 4 mm wide, and has a thickness of 2 mm. The screws that are placed inside have a diameter of 3 mm and a length outside of the plate of 9 mm. The birdcage body coil that is used has a radius of 352 mm and a length of 420 mm. The width of the legs is 40 mm while the endrings are 80 mm wide. The RF shield around the coil has a radius of 371.5 mm and a length of 700 mm. The implant is discretized on a 1 by 1 by 2 mm³ uniform grid and the rest of the setup is discretized using an automatically generated grid for a total of 12 million voxels.

In the third comparison, the two hip implants have a length of 200 mm, a thickness of 8 mm, a width of 30 mm, and the ball has a radius of 30 mm. The two hip implants are identical in size and are placed such that they replace the hip joint inside the body model of Duke. The birdcage body coil in these simulations is identical to the birdcage body coil used for the orthopedic

implant placed unto the ulna of Ella. The simulation setup was discretized using 12 million voxels with the hip implants being discretized on a 3 mm isotropic grid.

The last implant that is investigated is a cochlear implant. The lead of the cochlear implant has 12 electrodes, a diameter of 1.5 mm, and is 31 mm long [78, 79]. The lead is insulated with a plastic material that has zero conductivity and a relative permittivity of 3. One end of the implanted lead is attached to a casing that is 6 by 6 by 4 mm³. The implant is discretized on a 0.2 mm isotropic grid. In this scenario, the source of the RF fields is a mobile phone antenna. The antenna is a printed inverted F-antenna (PIFA) and operates at 900 MHz.

All the FDTD simulations are terminated at a convergence level of -50 dB and run on an NVIDIA GTX Titan Black. The proposed method uses GPU acceleration for the solver of Equation (4.10) running on an NVIDIA RTX 2070 super. The solver for Equation (4.4) runs on an Intel Core i5-6600 CPU, but can also run on a GPU. The proposed method is terminated at a convergence level of -50 dB which is similar to the FDTD simulations.

4.4.2 Theory prior method

For the sake of completeness, here we provide the full details of the original method. A visual overview of the original method can be seen in Figure 4.9. We start by discretizing Maxwell's equations, which describe the generated RF fields during an MRI experiment, given by

$$-\nabla \times H + \sigma E + i\omega\varepsilon E = -J^{source}, \quad (4.11a)$$

$$\nabla \times E + i\omega\mu H = 0, \quad (4.11b)$$

$$(D + C^{bg})f^{bg} = -q, \quad (4.11c)$$

where ω is the angular frequency, i is the imaginary unit, D is the discretized version of the curl operators, and q contains the source current density (J^{source}) which for our application is the current density running through the RF coil. If we now introduce an implant into the problem statement while keeping the discretization the same and solve for f our equation becomes

$$f = -(D + C^{bg} + C^{imp})^{-1}q, \quad (4.12)$$

The change that is introduced by C^{imp} takes place only on a small domain compared to the entire simulation domain that includes the RF coil. Using the support matrix S we can define the significantly smaller matrix \tilde{C}^{imp} as

$$\tilde{C}^{imp} = S^T C^{imp} S. \quad (4.13)$$

Equation (4.12) can now be reformulated using the Sherman-Morrison-Woodbury matrix identity in order to decrease the size of the matrix inverse from N by N to M by M .

$$\begin{aligned} f = & -(D + C^{bg})^{-1}q + \\ & (D + C^{bg})^{-1}S(I + \tilde{C}^{imp}S^T(D + C^{bg})^{-1}S)^{-1}. \end{aligned} \quad (4.14)$$

$$\tilde{C}^{imp}S^T(D + C^{bg})^{-1}q.$$

When we substitute f^{bg} in the above equation and introduce a so-called library matrix, Z , we arrive at

$$f = f^{bg} + Z(I - \tilde{C}^{imp}S^T Z)^{-1}\tilde{C}^{imp}S^T f^{bg}, \quad (4.15a)$$

$$Z = -(D + C^{bg})^{-1}S, \quad (4.15b)$$

where the perturbed RF field distribution f is calculated from the unperturbed RF field distributions f^{bg} .

When changing the conductivity and permittivity within the simulation domain to include the medical implant, the library matrix only requires the electric field responses of single-source current densities within the patient anatomy. For other applications, using the same formalism and equations as above the magnetic permeability can also be updated in case if the magnetic field responses are required. This could for example be used to calculate the magnetic field distortion around the implant. For this purpose, the magnetic field responses would need to be included within the library matrix after the current density distribution is obtained from the matrix inverse in Equation (4.15a). Similar to calculating the electric field using the VIE method once the solution x to Equation (4.4) is obtained, we can also compute the magnetic field according to

$$H(\rho) = H^{bg}(\rho) + i\omega\nabla \times \int_{\rho' \in bg} G(\rho - \rho')Sdiag(x)S^T dV, \quad (4.16)$$

where H and H^{bg} are the magnetic field distributions when the implant is and is not present respectively, note that since we do not have the library matrix anymore we need an equation to compute the magnetic field part of f .

4.5 Acknowledgements

The authors would like to thank Seb Harrevelt, Gabrio Rizzuti, and Rob Remis for interesting discussions and helpful insights.

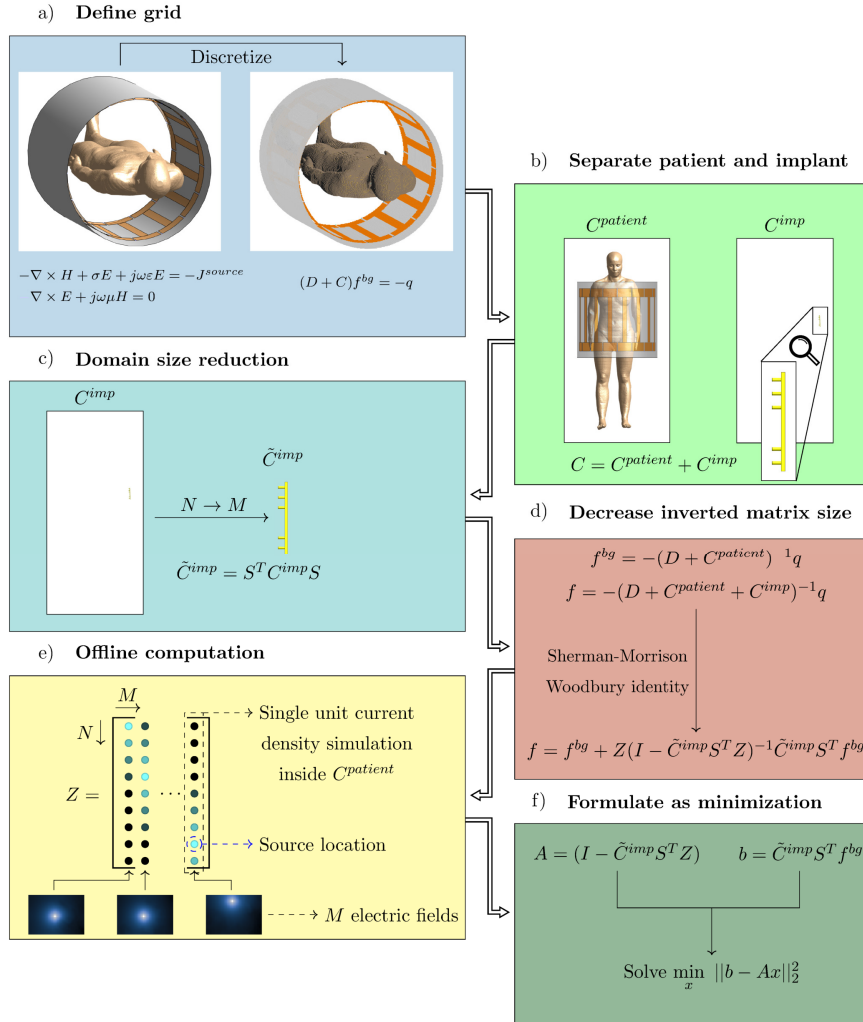


Figure 4.9: Schematic visualization of the prior method still using the library matrix. a) the RF coil, patient anatomy, and the implant are discretized on a cubic grid. b) the dielectric of patient anatomy and the implant are separated. c) the implant is only present on a small domain in the simulation, therefore we can decrease the domain size of the computation to only those locations where the implant is present. d) using the Sherman-Morrison-Woodbury identity we can do a low rank update to the RF field distribution without the implant. As a result of the domain reduction, the matrix inverse can now be calculated. e) before we can execute this calculation the so-called library matrix containing the electric field response of unit current densities at all possible implant locations is required. f) once this is available we can compute the field distribution online by casting the matrix inversion as a minimization problem.

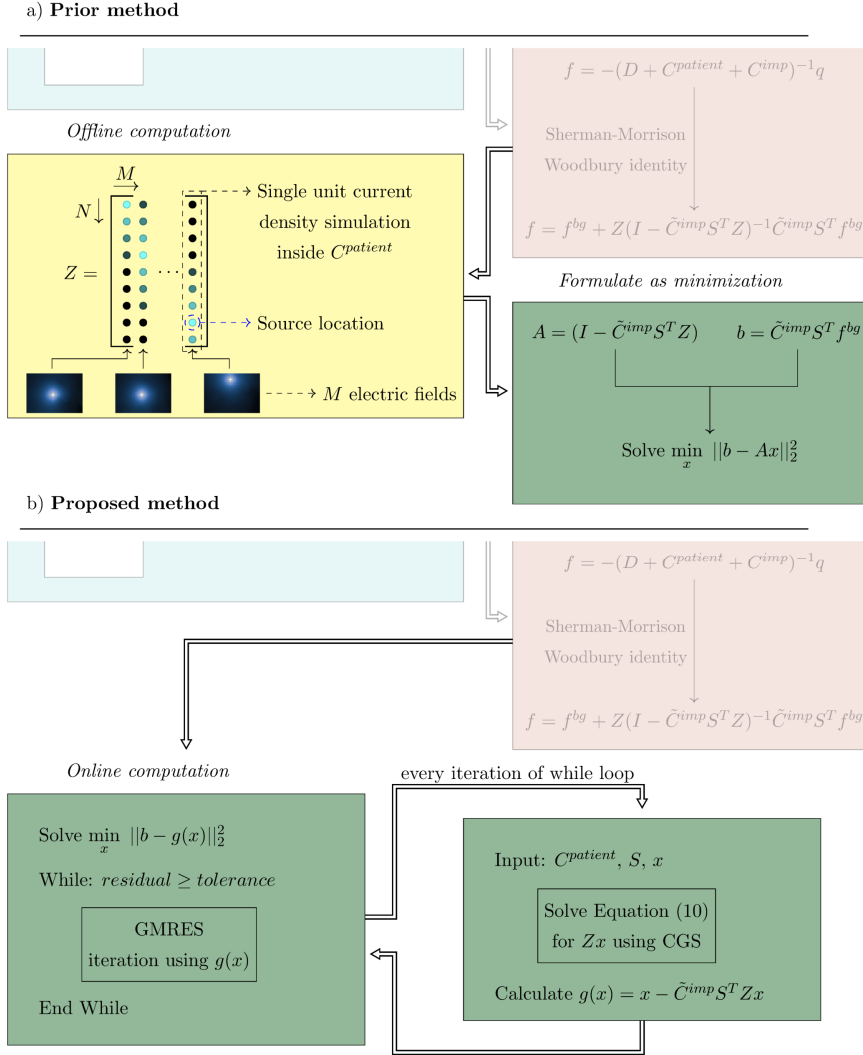


Figure 4.10: A comparison between the prior and proposed method. a) for the prior method a computationally expensive offline stage is required to obtain the library matrix. Afterwards, the matrix inversion to obtain the RF field distributions resulting from the implant can be solved using a minimization problem. b) we now propose to do the calculation completely online by using a matrix free minimization to compute the matrix inverse. The function that replaces the library matrix is a forward simulation of the RF field inside the patient anatomy generated by sources at the implant location. This forward simulation is performed using the VIE method.

Workflow for Subject-Specific RF Safety Assessment of patients with Orthopedic Implants in MRI

*Peter R.S. Stijnman, Bart R. Steensma, Gerrit Melis, Cornelis A.T. van
den Berg and Alexander J.E. Raaijmakers*

Abstract

Purpose: Patients with medical implants often do not undergo magnetic resonance imaging examination or are scanned with constrained sequence parameters, according to a label. Especially the radiofrequency electric field enhancement potentially causing temperature increases around the implant are of concern. For implants without a label it is not known what the eventual temperature increase will be. To enable this patient group to safely undergo MRI examination, we demonstrate a workflow using X-ray images that calculates what the expected specific absorption rate increase will be.

Methods: The workflow is demonstrated retrospectively for three patients; spinal fixation, knee replacement, and femur replacement implant. Using the X-ray images we locate and 3D model the implant. Then using a previously developed simulation method, we can calculate the SAR increase for multiple variations of the patient and implant position.

Results: From the workflow we can calculate a spatial SAR hotspot probability distribution showing where it is likely to obtain a significant temperature increase. Furthermore, the 1 g averaged peak SAR increase for multiple patient and implant positions can be used to determine the maximum amount of power that can be used by the MRI. Currently, it takes around 20 min to go from X-ray images to initializing the simulations. The total simulation time is 2 to 3 hours.

Conclusion: Using the information obtained from these simulations an informed decision on the sequence parameters can be made, either decreasing the total scan time or increasing the image quality, while ensuring safety for the patient.

5.1 Introduction

Magnetic resonance imaging (MRI) is one of the major imaging modalities. Although MRI is a very safe imaging modality, for patients with medical implants there are risks that are caused by the interaction of the radiofrequency (RF) fields of the MRI system with the implant [22, 3, 5, 80]. One of these risks is that the RF coil, which is used to excite the spins by creating a B_1^+ field, can induce high currents in metallic parts of the medical implant. These currents cause charge accumulation at the endings or protruding parts of the implant, resulting in very high local electric fields at these locations. These electric fields eventually may result in severe temperature increases and potentially tissue damage [23, 25, 64]. These and other interactions of the MRI system with the implant make patients with implants in principle not eligible for MRI. However, many implant manufacturers have been developing products that have been designed to be MRI-compatible. Following certain pre-defined standards, products may receive a label 'MRI-safe', 'MRI-unsafe', or 'MRI-conditional' [15, 14]. The latter category allows scanning but only within certain constraints. One of those constraints is on the time-average power delivered by the RF coil, which is limited to mitigate the local temperature increase for patients with an MRI-conditional implant. Constraining the amount of power that can be delivered by the RF coil either increases the time required for an exam (i.e. increasing the cost) or lowers the image quality (i.e. decreasing the diagnostic value).

In addition to scanning labelled implants, select larger hospitals are carefully scanning patients with non-labelled implants. The problem here is that the decision to scan a patient or not is based on empirical data only, for example, patients with similar implants that have been scanned previously in that hospital or case reports of patients that were scanned at other hospitals. There is no information about the RF safety for the patient at hand, making the risk versus benefit analysis more complicated. As a result, these patients with non-labelled implants are scanned with cautious and probably over-conservative sequence parameters, if these patients are scanned at all.

These conservative procedures try to ensure safety but come at the expense of scan time and/or image quality. For the majority of patients, the scan time could be reduced, and/or images could be improved if a patient-specific indication of the expected heating could be determined. We hypothesize that such a patient-specific indication of the expected heating could alleviate the scanning restrictions specifically for non-labelled implants. In addition, for some non-labelled implants, it may make the difference between scanning the patient at reduced power or not scanning the patient at all.

Determining the patient-specific RF heating is a computationally demanding task [81, 45, 10, 46, 42]. This is because the RF heating depends on

many different factors; the patient position, the patient anatomy, the implant shape, material properties, location, and the exposure condition generated by the RF transmit coil. Therefore, to correctly predict the eventual RF heating, different configurations of the implant position and patient position are simulated using an electromagnetic solver. For MRI applications the finite-difference time-domain (FDTD) and the finite element method (FEM) are the most commonly used solvers. The simulation time for a single configuration of patient, implant, and RF coil can be several hours even with GPU acceleration [20, 51]. This is because an implant with fine geometric details needs to be discretized on a very fine grid while the RF coil and patient anatomy have considerably larger dimensions. Therefore, it is unfeasible to simulate multiple exposure conditions, i.e. configurations of the patient and implant position, for every patient with an implant because this would take days to weeks to be completed.

In previous work, we have shown a method, the update method, that greatly reduces the simulation time [70, 71, 82]. This method makes use of the fact that the implant is only present in a small part of the entire simulation domain. As such, the implant is considered a small perturbation of the configuration without the implant. Starting from the RF fields when the implant is not present, the effect of the implant on these RF fields can be calculated within seconds or minutes compared to hours using FDTD or FEM. This method especially excels when the number of voxels to represent the implant is small with respect to the number of voxels inside the total domain, i.e. does not have a microstructure. It is therefore particularly suitable for simulating passive implants (e.g. orthopedic implants).

In this work, we want to use this simulation method to demonstrate a workflow to predict patient-specific RF heating for patients with orthopedic implants. For this purpose, we retrieve the implant position and geometry from X-ray images and prior knowledge about the implant. From the two-dimensional images, a three-dimensional model of the implant is created. Afterwards, this three-dimensional implant model is placed inside a standard human body model (e.g. Duke from the virtual family). Then, using the previously shown simulation method, we can quickly calculate the increase in the RF electric field around the implant by which a more well-founded patient-specific RF safety assessment can be obtained. The procedure for assessment of implant position will inevitably contain small uncertainties. We envision a workflow where the X-ray pictures are available from previous investigations which is typically the case for orthopedic implants. In this case, sufficient time is available to repeat the process for a range of likely configurations, resulting in a distribution of the expected peak levels of energy deposition around the implant. From this distribution, the highest value can be retrieved which we hypothesize to be much less restrictive than the overall worst-case scenario for

all patient positions within the scanner and all implant positions within the patient.

Using this information can provide a well-founded quantitative RF safety assessment to facilitate a more informed decision when scanning patients with non-labelled implants. As such, it could enable scanning patients with non-labelled implants in hospitals where this is currently not done.

The proposed procedure is retrospectively applied to three patients with orthopedic implants that underwent an MRI investigation. The method was tested using the X-ray images that were available for these patients. Implants types included a knee replacement, a hip replacement, and a spinal fixation implant.

5.2 Methods

In this work, we apply this workflow for three patients with different orthopedic implants. The first is a spinal implant, the second is an implant for a knee in the right leg, and the third is an implant that replaces the femur in the left leg, further details on the patients are shown in Table 5.1. The data was anonymized by a data manager before usage in this work.

Table 5.1: Patient details

Patient	Implant type	Gender	BMI	Landmark	Field Strength
1	Spinal fixation implant	M	24.9	Thorax	1.5 T
2	Knee implant	M	21.8	Knee	1.5 T
3	Femur implant	M	23.2	Upper leg	1.5 T

An overview of the envisioned workflow is shown in Figure 5.1. From the X-ray images with orthogonal projections of the patients, we can locate the position and geometry of the implant. Using a seeded region growing segmentation procedure we extract masks of the implant from these X-ray images. After obtaining the two-dimensional masks, a three-dimensional model of the implant can be constructed using *a priori* knowledge about the implant (i.e. the type of implant or knowing a part is circular). For the implants in this work, it was not known what the exact implant models/types were. If available, this knowledge would further facilitate the step from two-dimensional masks to three-dimensional models. Then only the location and rotation of the implants need to be extracted from the X-ray images. For the presented implants, the location was determined by means of the visible bone structure in the X-ray images. When the three-dimensional model has been constructed it is placed inside a human body model that preferably resembles the patient.

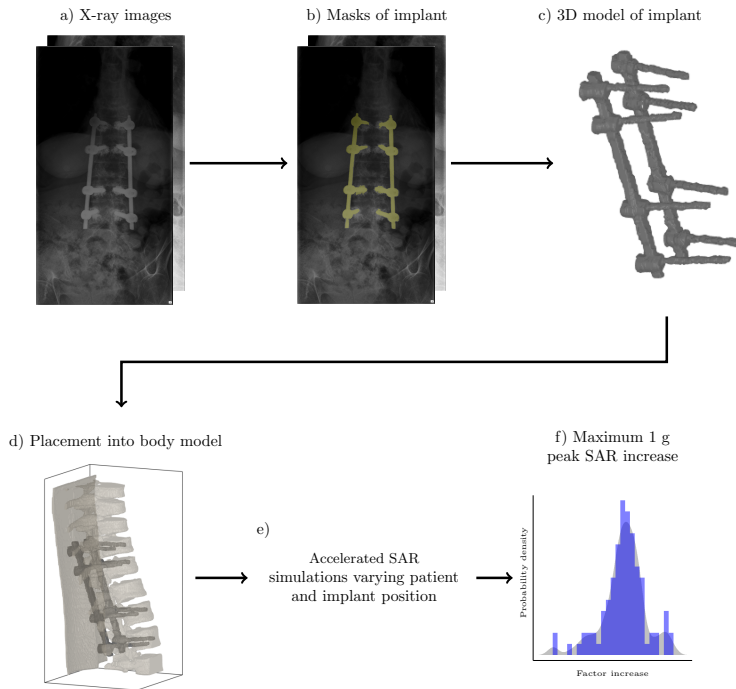


Figure 5.1: An overview of the proposed workflow. X-ray images of a patient with a spinal implant which are used to determine implant shape and position (a). Subsequently, this image is overlaid with a mask obtained from seeded region growing segmentation (b). From the mask a three-dimensional model is constructed (c). This model is placed inside a human body model (d). Then a fast simulation method is used to calculate the SAR increase around the implant (e). From these simulations an estimation of the 1 g averaged peak SAR increase can be made.

This placement of the implant is done based on the position of the implant with respect to the bone structure inside X-ray images. Since all patients in this study were male subjects with average postures, the model 'Duke' from the virtual family (IT'IS, Zurich, Switzerland) was used [83]. No scaling or morphing of the human body model is performed. Using that simulation setup and the pre-determined RF fields without the implant present, we calculate the perturbation of the RF fields caused by the implant. To cope with remaining uncertainties within the implant position within the patient and the patient position within the scanner, this calculation is repeated for a range of likely patient and implant positions. From the calculation results, we extract the

spatial distribution of the 1 g averaged specific absorption rate (SAR_{1g}) around the implant and the maximum increase in the peak SAR_{1g} .

An example of the X-ray images and output masks from the seeded region growing is shown in Figure 5.2. For the spinal implant, there are two orthogonal projections available; one sagittal view and one coronal view of the implant, Figure 5.2 a) and c) respectively. Figure 5.2 b) and d) show the X-ray images overlaid with the segmentation of the implant in yellow. The two-dimensional

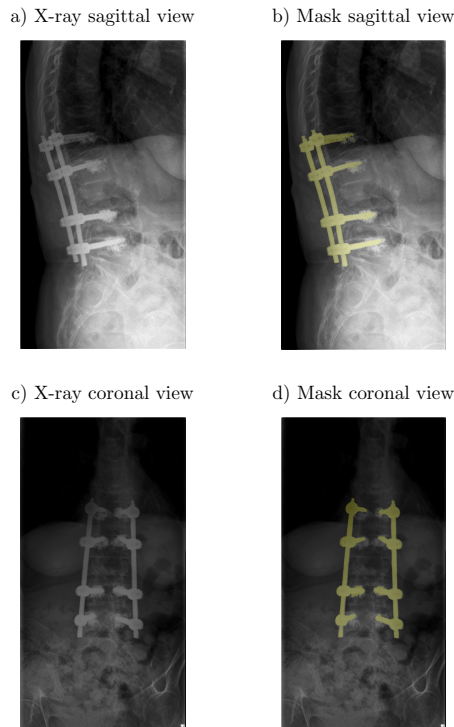


Figure 5.2: Segmentation of implants in X-ray images. a) and c) sagittal and coronal view of the spinal implant. Using a seeded region based segmentation strategy the implant position and geometry is obtained. This is overlaid onto the X-ray images in b) and d).

masks and the three-dimensional models of the implants are shown in Figure 5.3. For the knee and femur implant six and four X-rays, respectively, were used to obtain a complete view of the implants. The variations of the patient and implant position are indicated in Figure 5.4 a) and b) respectively. For the patient position, a translation in the x and z -direction of ± 2 cm is applied for a total of 5 different patient positions. For the spinal implant, the patient

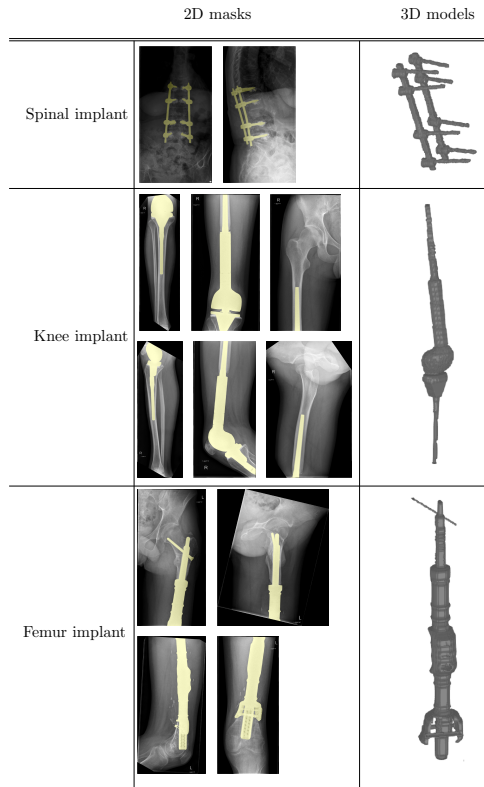


Figure 5.3: The workflow is demonstrated for three different orthopedic implant types; a spinal implant, a knee implant, and a femur implant. Here the X-ray images with the overlaid segmentations of the implant are shown in the second column. The third column shows the three-dimensional models that were constructed.

position is as indicated as in Figure 5.4, while for the other two implants the patient is positioned inside the scanner for a leg scan.

The central placement of the three different implants is shown in Figure 5.4 c), d), and e). Variations in implant position are applied in all three directions for ± 1 voxel, in all combinations achieving a total of 27 different implant positions. This makes a total of 135 possible variations that are calculated. Some implant positions are removed when the implant is incorrectly placed (e.g. when the screws of the spinal implant protrude from bone or enter the nerve tracts). These positions are not realistic and moreover will result in very high SAR values. After removing these configurations (i.e. by hand), we were

left with 105 configurations for the spinal implant, 90 configurations for the knee implant, and 65 configurations for the femur implant. From the calculated RF field distributions, the 1 g averaged SAR is extracted only around the implant since the increase in SAR is to be expected next to the implant. The

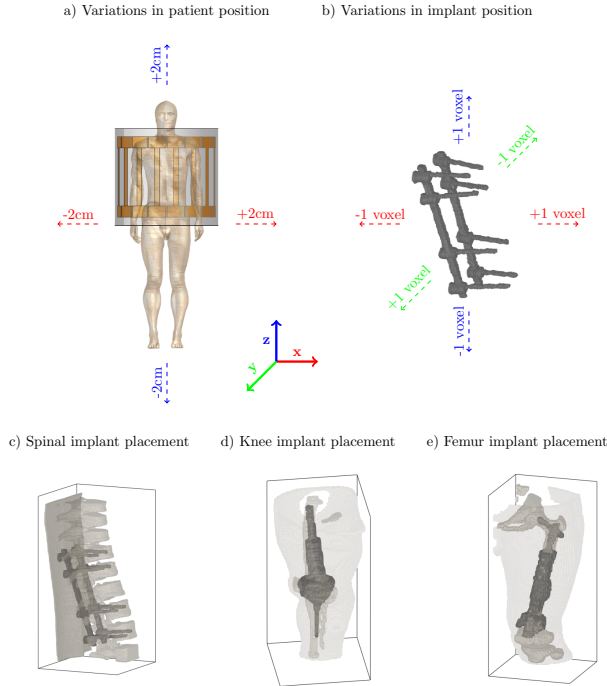


Figure 5.4: Placement of patient model within MRI system and placement of implant within patient model. a) variation of the patient position inside the RF coil. Both in the x and z -direction the patient is translated ± 2 cm. This results in 5 different exposures. b) variation in the implant position, ± 1 voxel in all three directions for a possible 27 combinations/different implant positions. c), d), and e) display the central position (i.e. no shift) of the implants inside the human body model. The bone and skin are also shown here.

RF fields without the implant, that are used as a basis for the accelerated calculations, are simulated using Sim4Life (ZMT, Zurich, Switzerland). The RF coil for all three implants is a volume birdcage body coil that is tuned to 64 MHz, corresponding to a 1.5 T MRI system. The RF coil has a leg length of 420 mm, a leg width of 40 mm, and a radius of 352 mm. The endrings are 80 mm wide and the RF shield has a length of 700 mm and a radius of

371.5 mm. For calculating the perturbation of the RF field by the implant, the three-dimensional model of the implant needs to be discretized. The resolution for the spinal implant was 2 by 2 by 2 mm³, the knee implant was discretized on a 3 by 3 by 6 mm³, and the femur implant on a 3 by 3 by 4.5 mm³.

The simulations using Sim4Life are performed on an NVIDIA GTX Titan Black, while the simulations using the accelerated calculation method are performed on an NVIDIA RTX 2070 super in combination with an intel i5-6600 CPU.

5.3 Results

Before we can use the accelerated calculation method to assess the RF electric field enhancement around the implant, the RF fields without the implant present have to be simulated. These RF fields will serve as a baseline to compare to the RF fields resulting from the scattering of the implant. The maximum intensity projections (MIP) of the SAR without an implant can be observed in Figure 5.5 in transverse, sagittal, and coronal orientation. These MIPs are the SAR distributions for the central position of the patient inside the RF coil, one of the five patient positions that have been used. Using the

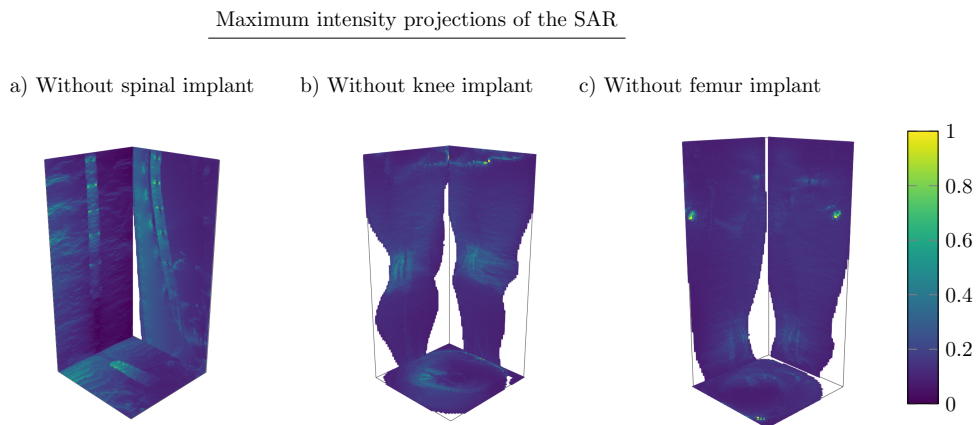


Figure 5.5: Maximum intensity projections of the SAR without the implant are shown for the three different implants. a) without spinal implant, b) without knee implant, and c) without femur implant. MIPs along the x , y , and z -axis are shown. These distributions are used as a baseline for the SAR increase as a result of the implant.

simulated RF field distributions without the implant as an input, the effect

of the inclusion of the implant on the RF fields is calculated for the five different patient and 27 different implant positions. From each of these field distributions the SAR_{1g} around the implant is extracted, which is used to make a spatial likelihood distribution for the SAR hotspot locations around the implant. This spatial distribution is depicted in Figure 5.6. For the spinal

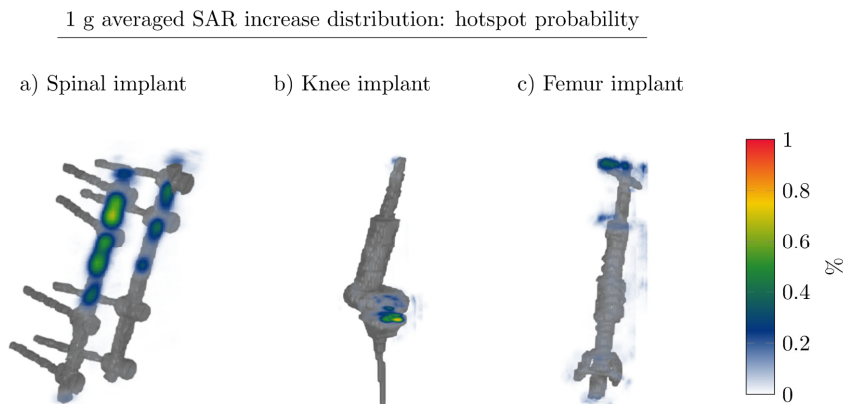


Figure 5.6: Spatial likelihood distributions for the SAR hotspot locations around the implant. Here the spatial distribution for the SAR hotspot location averaged over the different patient and implant positions is shown. a) spinal implant, b) knee implant, c) femur implant.

implant, it can be observed that the SAR hotspot will most likely occur near the top of the implant, where the chance is highest that the hotspot will be near the left plate. Furthermore, it can be seen that the SAR hotspot will not be near the tip of the screws. This is expected since this part is inside the vertebra which has a very low electric conductivity.

For the knee implant, we observe that the SAR hotspot will occur near the middle of the implant where the joint is located. This is exactly in the gap between the bottom and top parts of the implant. This part of the implant will act like a capacitor with the material between the implant parts as the dielectric that is charged. Both ends of the implant, which usually are the locations for SAR hotspots, are again located inside the bone (tibia and femur) and, therefore, do not show any significant SAR increase.

For the femur implant, the SAR hotspot will most likely occur near the top of the implant. Here one end of the screw protrudes from the bone, while the rest of the screw is positioned inside the hip joint. However, the edge of the bone is near the implant, thus the electric field enhancement can reach just outside it, causing a SAR hotspot. For each implant geometry, the local SAR MIP of the simulation set that resulted in the worst-case scenario (i.e.

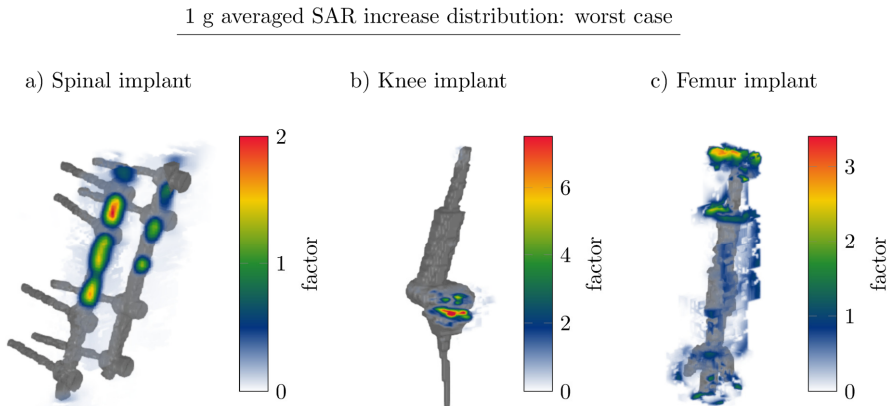


Figure 5.7: SAR_{1g} increase for the worst case of the investigated position variations. a) spinal implant, b) knee implant, and c) femur implant.

the variation where the peak SAR_{1g} is increased the most) is shown in Figure 5.7. For the spinal implant, the worst-case peak SAR_{1g} increase is a factor 2 compared to the case when no implant is present. For the knee implant, this factor increase is 7.5, and for the femur implant, this value is 3.4. For the knee implant, we now observe also a SAR hotspot on the left side of the knee.

To provide insight into the distribution of the peak local SAR_{1g} increase, histograms of the increase in the peak SAR_{1g} value for all the variations of the simulation setup are shown in Figure 5.8. For the spinal implant, the factor increases are between 1.15 and 2.1 with a mean value of 1.75 times higher peak SAR_{1g} . For the knee implant, the largest increase is observed, however, such SAR increases are only observed in a few simulations in the simulation set of the knee implant. With the femur implant, most of the simulations show a 1 to 1.25-factor increase, but again there are a handful of configurations inside the simulation set where the SAR_{1g} increase factor goes up to a value of 3.4. Finally, in Table 5.2 the acceleration obtained using our current method compared to FDTD is shown. Here the accelerated calculation method is between 58 and 234 times faster than FDTD with a total simulation time of under 3 hours per patient. In the total simulation time, the FDTD simulations without implant are not taken into account.

5.4 Discussion

In this work, we have shown a proof of concept for a workflow for patients with (orthopedic) implants to assess the patient-specific RF field enhancement. The

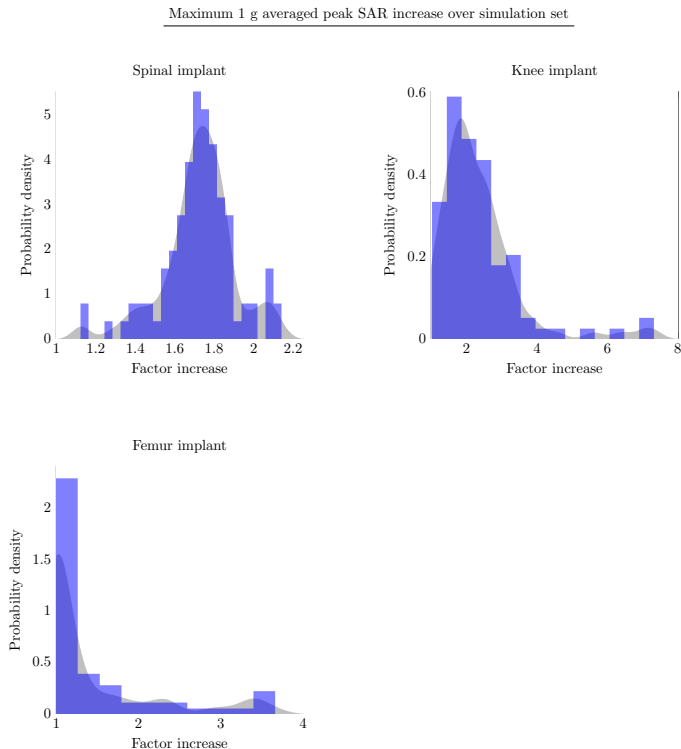


Figure 5.8: Histograms of peak SAR_{1g} increase for all investigated positional variations. In blue the histogram is shown indicating the binning of the maximum SAR values, while in gray the probability density function is shown, which is obtained from the histogram. a) spinal implant, b) knee implant, c) femur implant.

method requires some form of imaging to locate the implant location and -if unknown- the geometry of the implant as well. In this work, we used two-dimensional X-ray images to acquire two-dimensional orthogonal projections of the implant. These X-ray images are often available for patients with implants because they are made after implantation to verify that the implant is placed correctly. From the acquired two-dimensional orthogonal projections of the implant, a patient-specific three-dimensional implant model is constructed. Using this information, we can assess the RF safety of an implant within 2 to 3 hours for a range of patient and implant positions that are possible within uncertainty margins. From this workflow, we obtain both the value and the spatial distribution of the SAR increase as a result of the implant.

Table 5.2: Computation times if the simulations were done using FDTD, and when performed with the current method for the three different implants shown in this work.

Implant type	computation time FDTD (s)	computation time current method (s)	acceleration
Spinal	2337300	9975	234
Knee	475200	8100	58
Femur	432900	5850	74

Upon careful validation of our methodology, we envision that workflow can be used as a tool within the clinic to enable the scanning of patients with orthopedic implants where currently no label exists because the shape and position of the implant are highly patient-specific. Using this tool an informed decision can be made using realistic RF field enhancement information. This information can be used to increase the image quality or decrease the total scan time because higher flip angles or shorter repetition times can be used. Furthermore, for many patients with non-labelled implants, the benefit would be even larger. In hospitals without the expertise of scanning patients with non-labelled implants, this information could make the difference between scanning or not scanning a patient. For these patients, the proposed procedure poses a possibility to undergo an MRI examination, if there are no other safety concerns like ferromagnetic material inside the implant or it is expected that the implant will heat up from the gradient magnetic fields.

Currently, these patients are only scanned when the benefit of an MRI scan outweighs the risk. This decision is now made based on the experience of the MR-safety officer with scanning other patients that have implants. Therefore, these patients are often only scanned in large hospitals where this experience is present. Using this tool, possibly performed remotely, the decision to perform a scan is no longer based on empirical data alone, allowing for a more well-founded decision.

In order to bring this workflow to the clinic, it needs to be automated, where it now is semi-automated. Creating an automatic segmentation tool to extract the two-dimensional masks from the X-ray images would be the first step. This could be done using a deep learning strategy, which has already been shown to be able to segment anatomical images [84, 85, 86, 87]. Segmenting anatomical images is more difficult compared to segmenting an implant from an X-ray image since in the latter the implant is very bright compared to the anatomy. Such a network could also determine the position of the implant within a human body model.

The second step would be to automate the process to construct a three-dimensional model of the implant from the two-dimensional orthogonal masks.

When the type and model of the implant inside the patient are already known this process is trivial, and only the translation and rotation within the patient needs to be extracted from the images. Otherwise, again a deep learning strategy could be useful [88, 89, 90, 91]. There are some two-dimensional to three-dimensional neural networks that can reconstruct an object given a single or multiple projections of that object.

The final step would be to validate this workflow using phantom or ex vivo measurements using electric field or temperature probes. These measurements can then be correlated with the results from the accelerated simulations to show that the predicted SAR increase is correct.

A drawback of the presented workflow is that the patient anatomy is required. This is generally not available and instead standard human body models are used, similar to current RF safety assessment techniques. There are multiple different body models available. However, these are never exactly similar to the patient at hand. There is even a library of simulated RF field distributions for various human body models and for various imaging positions within the MRI (IT'IS, Zurich, Switzerland) that can be used as input for the proposed workflow. Ideally, the RF field distributions without implant for the actual patient anatomy are used as input to perform these RF field simulations with the accelerated calculation method. However, since these are not obtainable some investigation is required to find the effect that the difference in anatomy has on the eventual SAR increase when an implant is present.

The current workflow can be performed in the days before the patient will undergo an MRI examination. Ultimately, this workflow would also be fast enough for it to be performed online at the scanner. However, we are not at this stage currently. Before this is possible, the workflow should be tested extensively as mentioned before, since currently before a label is granted for an implant it is thoroughly reviewed. With the proposed workflow we would be defining a patient-specific label for the situation at hand, therefore, some form of a review or quality assurance should still be required.

5.5 Conclusion

In this work, we have demonstrated a workflow for patient-specific RF safety assessment of patients with three different orthopedic implants. Using X-ray images the implant location and geometry are determined. The three-dimensional implant model is then placed inside a human body model to quickly assess the SAR increase resulting from the scattering of the implant. To perform the calculation of the RF fields a fast calculation method is used that only calculates the effect the implant has on the RF fields. This results in an assessment of the SAR distribution around the implant and the peak SAR increase within three hours based on a series of 105 simulations with potential

implant and patient positions, to cover positional uncertainties.

Using the workflow a more informed decision about the RF safety for a specific patient can be made. This workflow is beneficial for both patients with labelled and non-labelled implants. Patients with labelled implants can be scanned more efficiently since the label dictates a worst-case scenario. For patients with non-labelled implants, it provides a more informed risk versus benefit analysis on scanning or not scanning that patient.

Transceive phase corrected 2D contrast source inversion-electrical properties tomography

*Peter R.S. Stijnman, Stefano Mandija, Patrick S. Fuchs,
Cornelis A.T. van den Berg and Rob F. Remis*

*Based on: P.R.S. Stijnman, S. Mandija, P.S. Fuchs, C.A.T. van den Berg,
R.F. Remis. Transceive phase corrected 2D contrast source inversion-electrical
properties tomography. Magn Reson Med. 2021; 85: 2856– 2868.
<https://doi.org/10.1002/mrm.28619>*

Abstract

Purpose: To remove the necessity of the tranceive phase assumption for CSI-EPT and show electrical properties maps reconstructed from measured data obtained using a standard 3T birdcage body coil setup.

Methods: The existing CSI-EPT algorithm is reformulated to use the tranceive phase rather than relying on the tranceive phase assumption. Furthermore, the radio frequency (RF) shield is numerically implemented to accurately model the RF fields inside the MRI scanner. We verify that the reformulated two-dimensional CSI-EPT algorithm can reconstruct electrical properties maps given two-dimensional electromagnetic simulations. Afterward, the algorithm is tested with three-dimensional FDTD simulations to investigate if the two-dimensional CSI-EPT can retrieve the electrical properties for three-dimensional RF fields. Finally, an MR experiment at 3T with a phantom is performed.

Results: From the results of the two-dimensional simulations, it is seen that CSI-EPT can reconstruct the electrical properties using MRI accessible quantities. For three-dimensional simulations, it is observed that the electrical properties are underestimated, nonetheless, CSI-EPT has a lower standard deviation than the standard Helmholtz based methods. Finally, the first CSI-EPT reconstructions based on measured data are presented showing comparable accuracy and precision to reconstructions based on simulated data, and demonstrating the feasibility of CSI-EPT.

Conclusion: The CSI-EPT algorithm was rewritten to use MRI accessible quantities. This allows for CSI-EPT to fully exploit the benefits of the higher static magnetic field strengths with a standard quadrature birdcage coil setup.

6.1 Introduction

Electrical properties tomography (EPT) is an MR-based technique aiming at measuring the electrical properties (conductivity and permittivity) of tissues. This is achieved in a non-invasive manner through MRI-based mapping of the circularly polarized magnetic component (B_1^+ , the transmit efficiency) of the transmit radio frequency (RF) field. The acquired conductivity and permittivity can be used as a contrast mechanism, especially the conductivity of tissue has been shown to have potential as a biomarker in oncology [92, 93, 94, 95, 96, 97] and stroke imaging [98, 99]. Further, the conductivity and permittivity are important in the field of MR safety, where they are used to compute the specific absorption rate (SAR). The SAR defines the amount of deposited energy during MRI exams and relates directly to the heating of the tissue under examination [100, 101, 102, 103].

There is a variety of different EPT approaches that have been recently published as shown in the review work [92]. A large group of these approaches are derivative-based and stem from the Helmholtz equation for magnetic fields [104, 105, 106, 107, 108]. In these approaches, a second-order derivative using finite difference kernels needs to be computed on the measured B_1^+ fields. This leads to noise amplification in the reconstructed EPT maps and introduces errors in the reconstruction of the electrical properties most notably at tissue boundaries [109, 110].

Next to Helmholtz (derivative-based approaches), gradient-EPT [111] and cr-MREPT [112], there are also approaches based on the integral formulation of the Maxwell equations [113, 114] where the objective is to minimize a cost function by iteratively updating the electrical properties. Among these integral-based methods, the contrast source inversion (CSI) method [115] has been shown to be more noise-robust than derivative-based approaches [116], and allows better EPs reconstructions at tissue boundaries. However, these benefits come at the expense of a higher computational cost and, generally, integral-based optimization methods are more difficult to implement.

Furthermore, CSI-EPT reconstructions have two major limitations. First, CSI-EPT requires knowledge of the incident RF electric and magnetic fields. These are the RF fields of the empty transmit coil, i.e. when an object/patient is not present. These RF fields can only be obtained through electromagnetic simulations and will vary from coil to coil. Second, similar to the derivative based MR-EPT approaches, the CSI-EPT reconstruction algorithm is formulated in terms of the complex B_1^+ field. While the magnitude of the B_1^+ field is measurable with MRI, the phase is not accessible. To overcome this limitation, the measurable transceive phase is used. From this, the transmit phase is derived as half of the transceive phase, which is known as the transceive phase assumption (TPA). However, this assumption is only valid at low field

strengths and for symmetrical objects, where the polarization remains circular. For more complex structures, non-symmetrical objects, or multiple tissue interfaces, these conditions are not met, and the assumption is not valid [106]. This occurs especially at higher static magnetic field strengths due to the larger magnitudes of scattered RF fields, leading to elliptical polarization.

To reconstruct the tissue parameters, essentially two options can be followed. The first option is to discard the phase information of the B_1^+ and formulate the CSI-EPT algorithm in terms of only the magnitude. This has been done in [117] and has been implemented for MR-EPT in [118]. While this approach showed its potential in two-dimensional simulation settings, it comes with an intrinsic drawback. It is well known that the conductivity information is mostly imprinted in the phase of the B_1^+ [119], therefore discarding this information from the reconstruction algorithm makes the reconstruction problem even more challenging.

Therefore, in this work, we reformulate the CSI-EPT algorithm to use the B_1^+ magnitude and the transceive instead of the transmit phase, both measurable with MRI, without relying on the transceive phase assumption, which was until now a cornerstone of MR-EPT reconstruction methods. Furthermore, CSI-EPT reconstructions require knowledge of the background RF-fields. These are obtained from electromagnetic simulations which require inclusion of the RF-shield. We will show that supplying the CSI-EPT algorithm with the correct incident fields is necessary to obtain the correct electromagnetic properties. These RF-shields are especially important for reconstructions from realistic MRI measurements, as these fields are only accessible via simulations. Thus, we numerically incorporate this RF-shield to mimic the realistic MRI scenario. Using these proposed changes we will present the first reconstructions of the electrical properties of a phantom with MRI acquired data using CSI-EPT.

6.2 Theory

6.2.1 Transceive Phase Correction

In this section, we reformulate the CSI-EPT algorithm as described in [113]. We start by defining the contrast source as

$$w(\boldsymbol{\rho}) = \chi(\boldsymbol{\rho})E_z(\boldsymbol{\rho}), \quad (6.1)$$

where E_z is the z -component of the total electric field, and χ is the contrast with respect to free space which is defined as

$$\chi(\boldsymbol{\rho}) = \varepsilon_r(\boldsymbol{\rho}) - 1 - \frac{\sigma(\boldsymbol{\rho})}{j\omega\varepsilon_0}, \quad (6.2)$$

with $\boldsymbol{\rho}$ as the position vector, ε_0 and ε_r as the permittivity in vacuum and relative permittivity respectively, σ is the conductivity and ω is the angular Larmor frequency. Reconstructing the contrast is the goal of this method since the electrical properties can directly be calculated once the contrast is known. The contrast and contrast source are the two parameters that are iteratively updated in CSI-EPT. This is realized by minimizing the cost functional presented in [113] given by

$$F(w_l, \chi) = \eta_S \sum_l \|B_{1,l}^+ - (B_{1,l}^{+,inc} + G_S^+\{w_l\})\|_S^2 + \eta_D \sum_l \|\chi(E_{z,l}^{inc} + G_D\{w_l\}) - w_l\|_D^2, \quad (6.3)$$

where $l \geq 1$ indicates a summation over various transmit channels including linear combinations such as a standard quadrature drive, $\eta_{S,D}$ are normalization factors for the data functional (first term on the right-hand side of (6.3)) and object functional (second term on the right-hand side of (6.3)). It should be noted that in MRI the domain where the object is located, D , is the same as the location where the data is collected, S . Further, G_S^+ and G_D are integral operators that map the contrast source to the scattered B_1^+ field, $B_1^{+,sc}$, and the scattered electric field, E_z^{sc} , respectively. These integral operators are given by

$$E_z^{sc}(\boldsymbol{\rho}) = G_D\{w(\boldsymbol{\rho}')\} = k_0^2 \int_{\boldsymbol{\rho}' \in \mathbb{D}} \hat{G}(\boldsymbol{\rho} - \boldsymbol{\rho}') w(\boldsymbol{\rho}') dV, \quad (6.4a)$$

$$B_1^{+,sc}(\boldsymbol{\rho}) = G_S^+\{w(\boldsymbol{\rho}')\} = \frac{\omega}{2c_0^2} (\partial_x + j\partial_y) \int_{\boldsymbol{\rho}' \in \mathbb{D}} \hat{G}(\boldsymbol{\rho} - \boldsymbol{\rho}') w(\boldsymbol{\rho}') dV. \quad (6.4b)$$

Here, k_0 and c_0 are the wavenumber and the speed of light in vacuum, respectively. The spatial derivatives with respect to x and y are indicated with $\partial_{x,y}$. The source locations are defined by $\boldsymbol{\rho}'$ and $\hat{G}(\boldsymbol{\rho} - \boldsymbol{\rho}')$ is defined as the two-dimensional free-space Green's function, which is given by

$$\hat{G}(\boldsymbol{\rho} - \boldsymbol{\rho}') = -\frac{j}{4} H_0^{(2)}(k_0 |\boldsymbol{\rho} - \boldsymbol{\rho}'|), \quad (6.5)$$

where $H_0^{(2)}$ is the zeroth-order Hankel function of the second kind.

The problem with the cost functional given by (6.3) is that the phase of the B_1^+ field is not directly accessible through measurements. What can be measured is the so-called transceive phase ϕ_{\pm} . This transceive phase consists of the transmit phase ϕ_+ and receive phase ϕ_- according to

$$\phi_{\pm} = \phi_+ + \phi_-. \quad (6.6)$$

Therefore, we can write the B_1^+ field in terms of the transceive phase as

$$B_1^+ = |B_1^+|e^{j\phi_+} = |B_1^+|e^{j\phi_{\pm}}e^{-j\phi_-}. \quad (6.7)$$

Substituting (6.7) into (6.3) results in a new cost functional given by

$$F(w_l, \chi, \phi_-) = \eta_S \sum_l |||B_{1,l}^+|e^{j\phi_{\pm,l}}e^{-j\phi_{-,l}} - (B_{1,l}^{+,inc} + G_S^+\{w_l\})||_S^2 + \eta_D \sum_l ||\chi(E_{z,l}^{inc} + G_D\{w_l\}) - w_l||_D^2. \quad (6.8)$$

The transmit phase is now written in terms of the transceive (known) and receive phase (unknown). Iterating through the algorithm now proceeds similarly as in standard CSI-EPT, except that the measurable transceive phase is used and that the receive phase is iteratively updated using the estimates of the contrast function and electric field strength at the current iteration, n .

In this section, the electric and magnetic RF fields are the fields encountered in the receive state of the birdcage coil. During transmission, the birdcage coil is fed in quadrature mode (i.e. a 90° phase difference between the two ports) and this creates a circularly polarized B_1 field that is efficient in tipping the spins. In receive mode, the birdcage coil is switched to a receive state which means the 90° phase difference becomes a -90° phase difference. This results in a counter-rotating circularly polarized field that is efficient in receiving the signal. This receiving state of the birdcage coil is called reverse quadrature or anti-quadrature. This mode of the transmit coil creates different RF fields. The incident RF fields in reverse quadrature display a simple phase shift for a birdcage coil setup compared with forward quadrature, but the scattered fields are inherently different which is why the TPA is not valid when these scattered fields are comparable in magnitude to the incident field.

To compute the scattered receive field at each iteration we use

$$\begin{aligned} B_{1,n}^-(\boldsymbol{\rho}) &= G_S^- \{ \chi_{n-1}(\boldsymbol{\rho}') E_{z,n}(\boldsymbol{\rho}') \} \\ &= -\frac{\omega}{2c_0^2} (\partial_x - j\partial_y) \int_{\boldsymbol{\rho} \in \mathbb{D}} \hat{G}(\boldsymbol{\rho} - \boldsymbol{\rho}') \chi_{n-1}(\boldsymbol{\rho}') E_{z,n}(\boldsymbol{\rho}') dV, \end{aligned} \quad (6.9)$$

where $B_{1,n}^-$ defines the complex conjugate of the scattered receive field and $E_{z,n}$, the electric field during reception (anti-quadrature setting) at iteration n , is defined as

$$E_{z,n}(\boldsymbol{\rho}) = G_D \{ \chi_{n-1}(\boldsymbol{\rho}) E_{z,n-1}(\boldsymbol{\rho}) \} + E_z^{inc}(\boldsymbol{\rho}). \quad (6.10)$$

Here E_z^{inc} , the incident electric field during reception, is modeled together with $B_1^{-,inc}$ for an empty coil, i.e. in reverse quadrature mode for a birdcage coil. Since the incident fields for the transmit state are already modelled for each

Procedure 1 Transceive phase corrected CSI-EPT

Input: Compute w_0 , w_0^\dagger , χ_0 and the incident RF-fields

for $n = 1$ to maxIterations **do**

Step 1 Update the contrast sources:

Compute g_n^w for $F_n^R(w_{n-1}, \chi_{n-1}, \varphi_{n-1})$

Compute the Polak-Ribière update direction

Compute the stepsize

Update the contrast source

Step 2 Update E_z

Step 3 Update the contrast:

Compute g_n^X for $F_n(w_n, \chi_{n-1}, \varphi_{n-1})$

Compute the Polak-Ribière update direction

Compute the stepsize

Update the contrast

Step 4 Update the receive phase:

Solve for E_z^\dagger with χ_n

Compute $B_1^{-, \dagger}$

Extract the receive phase

Step 5 Update the residuals and normalization factors

if $F_n \leq \textit{tolerance}$ **then**

Break

end if

end for

Output: χ_n , w_n , B_1^+ , $B_1^{-, \dagger}$, E_z and E_z^\dagger

port the incident receive fields are acquired by driving these ports in reverse quadrature.

By adding the receive phase as an extra unknown into the minimization problem, the minimization becomes more difficult and the computation time is increased since the number of required integral operations is increased to obtain the receive phase. However, the TPA is no longer required to reconstruct the contrast from the B_1^+ data. The new pseudo code is shown below with a dagger (\dagger) indicating the quantities in the receive state of the birdcage coil. Furthermore, the Polak-Ribière update directions can be found in [120, 121] and [113].

6.2.2 Numerical Implementation Of The RF-Shield

Inside every MRI system, there is an RF-shield present. The purpose of the RF-shield is to screen external RF signals from the MRI signal. The RF-shield changes the RF-fields produced by the transmit coil, and as previously

stated, the incident electric and magnetic RF-fields are required as input for the CSI-EPT algorithm. Therefore, including the RF-shield in the model that simulates these incident RF-fields is required. The copper RF-shield can be approximated by a perfect electrically conducting material (PEC).

In [122] the RF-shield was included in the Green's tensor functions. This is an accurate way to do this, however, different MRI systems would require different Green's tensor functions. Furthermore, the shift invariance of the free-space Green's tensor function is lost, $\hat{G}(\boldsymbol{\rho} - \boldsymbol{\rho}') \rightarrow \hat{G}(\boldsymbol{\rho}, \boldsymbol{\rho}')$ and this results in a significant increase in computation time because the integrals in Equations (4a, 4b, 9 and 10) can no longer be computed using the fast Fourier transform.

To avoid a severe increase in the computation time of the CSI-EPT algorithm, we implemented the RF-shield for the incident fields numerically using mirror currents. At the location of the PEC, the tangential electric field should be zero. To accomplish this for the circular RF-shield we assume that it is infinitely long in the z -direction. From there we follow [123], where an improved placement of the mirror currents for a first-order approximation of circular planes is given as

$$d = \frac{R_{PEC}^2}{R_S}, \quad (6.11)$$

where d is the distance from the mirror source to the center of the birdcage coil, R_{PEC} is the radius of the RF-shield and R_S is the distance from the center of the RF-shield to the source.

6.3 Methods

First, CSI-EPT was used to reconstruct tissue parameters based on simulated data. Simulations allow knowledge of the ground truth EPs, thus benchmarking the accuracy of the reconstruction algorithm. Subsequently, first CSI-EPT reconstructions were performed from MRI measurements in a phantom.

6.3.1 Simulations

The performance of the modified CSI-EPT scheme is tested first by the use of 2D line source simulations in Matlab (MathWorks, Natick, Ma). The contrast that is used for these simulations is shown in Figure 6.1. This contrast was chosen to be asymmetrical to render the TPA invalid. With these simulated data we investigated the following aspects:

Impact of RF shield

The incident electric and magnetic fields were computed with and without the RF-shield included using the setup that is shown in Figure 6.2. Only the

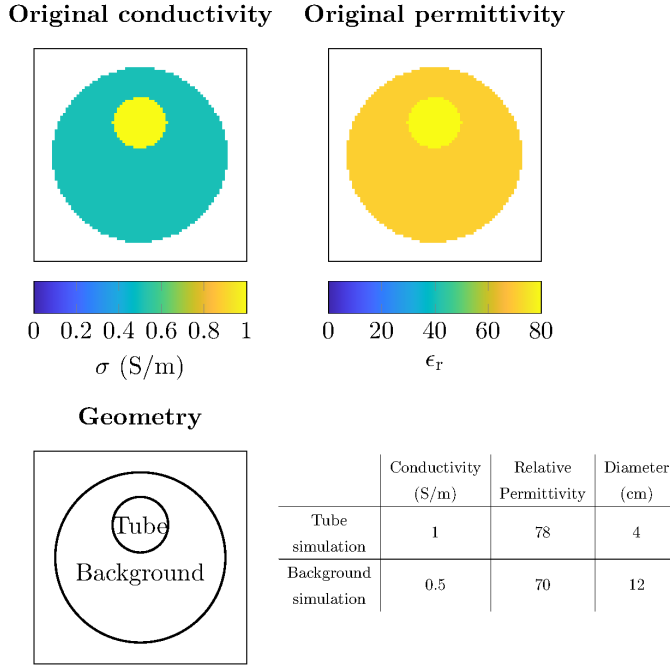


Figure 6.1: The top left shows the conductivity of the phantom and the top right shows the relative permittivity. The bottom left shows the the geometry of the phantom where the inner compartment will be referred to as the tube and the other compartment is referred to as the background. On the bottom right, the table shows the conductivity and permittivity values that were used in simulations as well as the dimensions of the phantom.

quadrature mode of the birdcage coil is used for comparison between the incident field with and without the RF-shield. The reconstructed conductivity is shown in the same figure to demonstrate the impact of using the wrong incident RF-fields on the reconstructed electrical properties. In all the subsequent results the RF-shield is included in the modelling of the incident fields.

Impact of TPC vs TPA

The effects of the transceive phase on the original CSI-EPT algorithm, using the TPA, and the newly proposed transceive phase corrected (TPC) CSI-EPT algorithm are investigated for 3T and 7T. In all the simulations both the B_1^+ amplitude and transceive phase are separately corrupted with white Gaussian

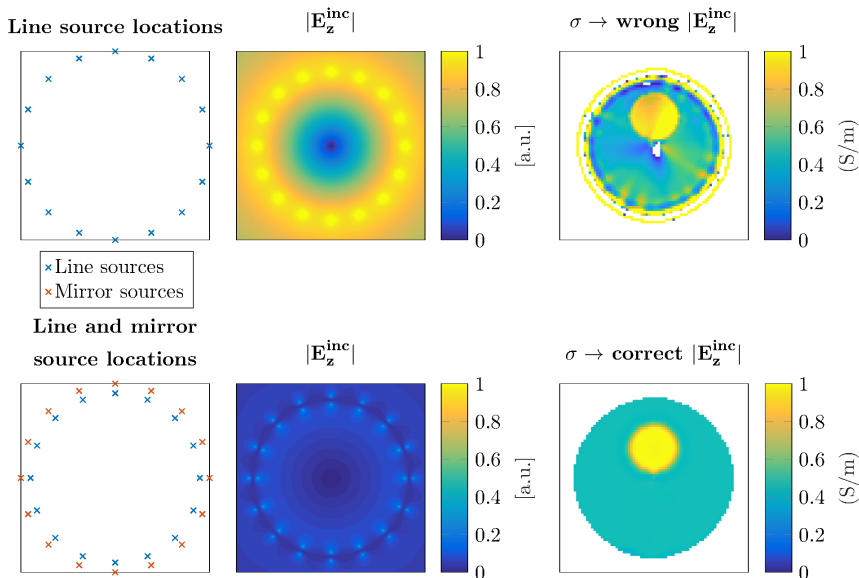


Figure 6.2: The top row shows the setup of the line sources (left) and the resulting incident electric field amplitude (middle) and the reconstructed conductivity when this incident RF-field is used (right). The bottom row shows the same for the numerical implementation of the PEC with mirror sources. The same current is running through the line sources in both cases.

noise using realistic SNR values [124] for the corresponding field strength (1.5T SNR = 30, 3T SNR = 54, 5T SNR = 82, 7T SNR = 119, 9T SNR = 151). We follow this approach because the B_1^+ amplitude and transceive phase are acquired using two different measurements each with a corresponding noise set [125]. The noise was added to the simulation by duplicating the B_1 maps and corrupting both the real and imaginary parts separately. From one pair of corrupted real and imaginary values, the B_1^+ amplitude was extracted. The other pair of real and imaginary values was corrupted with a different noise set and used to construct the transceive phase. In all the simulations total variation regularization was used during the minimization, as described in [113].

To obtain a measure of the quality of the reconstructed electrical properties the mean absolute error is computed. This is performed within a region of the phantom as indicated by the black box in Figure 6.4. We define the mean

absolute error as

$$Err_\sigma = \frac{1}{N} \sum \frac{|\sigma_{true} - \sigma_{recon}|}{\sigma_{true}} \cdot 100\%, \quad (6.12)$$

where Err_σ defines the mean absolute error in the conductivity, σ_{true} is the original conductivity of the phantom, σ_{recon} is the reconstructed conductivity and N is the number of voxels within the region indicated by the black box.

After these 2D line source simulations a 3D FDTD simulation package (Sim4Life, ZMT, Zurich, Switzerland) is used to investigate the effects of the 2D assumption that is used in this version of the CSI-EPT algorithm. This assumption states that in the center plane of the transmit coil the RF-fields have only the E_z , B_x and B_y components. Before using measured data we want to characterize the error that is made by using this 2D assumption.

For these simulations, the same phantom as for the 2D line source simulations was constructed, the specifications are shown in Figure 6.1. The simulated transmit coil is a 16 rung highpass birdcage coil with a diameter of 72cm and a rung length of 42cm. The endrings have a width of 8cm and the included RF-shield has a length of 70cm and a diameter of 74cm. The birdcage coil is driven in quadrature mode. From these simulations, the incident RF-fields and the B_1^+ magnitude and transceive phase with the phantom in the simulation are used as inputs for the CSI-EPT algorithm.

6.3.2 Measurement

Finally, CSI-EPT reconstructions from MRI measurements using a 3T system (Igenia, Philips, Eindhoven, Netherlands) were performed to show the potential of this method on in vivo data. Since there is no ground truth available with measurements, unlike the simulations, the CSI-EPT reconstructions are compared to the standard Helmholtz based EPT method, where a 7 point kernel is used [109, 119].

For the measurements, a phantom was constructed with the same dimensions as the phantoms shown in Figure 6.1. The phantom was agar based and NaCl was added to give the two compartments different conductivity values. In the tube 5.5 gr/L of NaCl was added, leading to a conductivity of 0.9 S/m at 21 °C. For the background 2.5 gr/L was added resulting in a conductivity of 0.41 S/m at 21 °C [126].

An AFI sequence was used to obtain the B_1^+ amplitude [127]. The transceive phase was acquired with two spin echoes with opposite gradient polarity, this reduces the phase contribution due to the eddy currents [119]. The body coil was used for transmission and a head coil was used for reception.

A vendor specific algorithm (Philips, Constant Level of Appearance-CLEAR) was used to convert the receive phase measured with the head coil to the body

coil [128]. Using this algorithm it is as if the body coil was used for both transmitting and receiving. The benefit is that using the head coil during reception significantly increases the SNR of the measurements. The sequence parameters that were used are noted in Table 6.1.

To correctly model the incident RF fields, the B_1^+ amplitude and the phase difference between the two ports of the birdcage coil were extracted from the log file created by the scanner.

Finally, the mean (μ) and standard deviation (σ) are given for the reconstructions of the measured data. These values are computed for the two different compartments of the phantom. Since standard Helmholtz MR-EPT is not able to reconstruct the boundaries properly [109], we report the mean and standard deviation in the case the boundary between the background and the inner tube is included and when it is excluded.

6.4 Results

The effect of the mirror currents is shown in Figure 6.2. It can be seen that the magnitude of the electric field significantly decreases for equal currents running through the line sources. Further, it can be seen that the electric field goes to zero at the location of the RF-shield. The inclusion of the RF-shield, even with a numerical approximation, results in a more realistic model of the incident RF fields which helps with the practical implementation of the CSI-EPT method. This is also observed in Figure 6.2, where the contrast is reconstructed using the incident field with and without the RF-shield (i.e. the total RF fields were calculated with the RF-shield present).

CSI-EPT reconstructions from the 2D line source simulations at different field strengths are shown in Figure 6.3. It can be observed that the error due to

Table 6.1: Scanner parameters for the AFI and SE sequence.

Parameter	AFI	SE
FoV	200x200 mm ²	200x200 mm ²
Resolution	2.5x2.5x3mm ³	2.5x2.5x2.5mm ³
TR1	50ms	1000ms
TR2	250ms	-
TE	2.7ms	5ms
Flip angle	65°	90°/180°

the TPA increases with increasing field strength. This is because of the increasing invalidity of the TPA at higher field strengths, whereas for the transceive phase corrected CSI-EPT algorithm this error is not present. Furthermore, the reconstruction for the transceive phase corrected CSI-EPT algorithm improves due to the higher field strength with its inherently increased sensitivity.

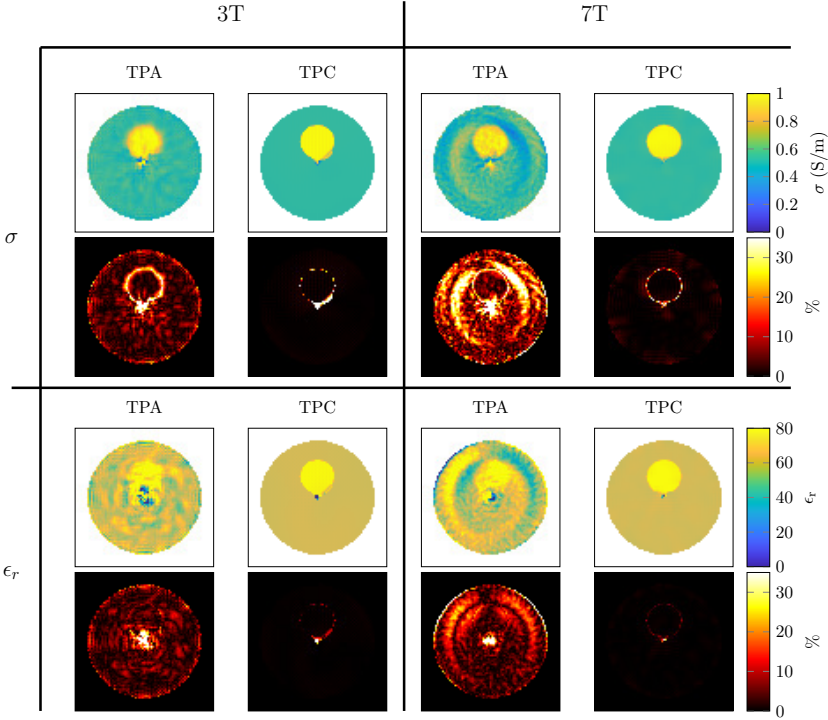


Figure 6.3: The top row shows the conductivity reconstructions with the corresponding absolute error maps below them. The reconstructions were performed with the TPA and the newly proposed method, indicated with TPC, both at 3T and 7T. The third row shows the permittivity reconstructions with the corresponding error maps below them.

This is further illustrated in Figure 6.4, where the effect of these two field strength dependent factors is shown. The mean relative error of the reconstructions at different field strengths for both the standard CSI-EPT (with TPA) scheme and the newly proposed TPC CSI-EPT are shown. Furthermore, examples of the noise corrupted simulated B_1^+ magnitude and transceive phase are shown. From the line plots, we can see the impact of the noise at lower field strengths, because of the lower sensitivity, and the TPA at the higher

field strengths. When the TPC CSI-EPT algorithm is used the higher intrinsic sensitivity at the higher field strengths can be utilized.

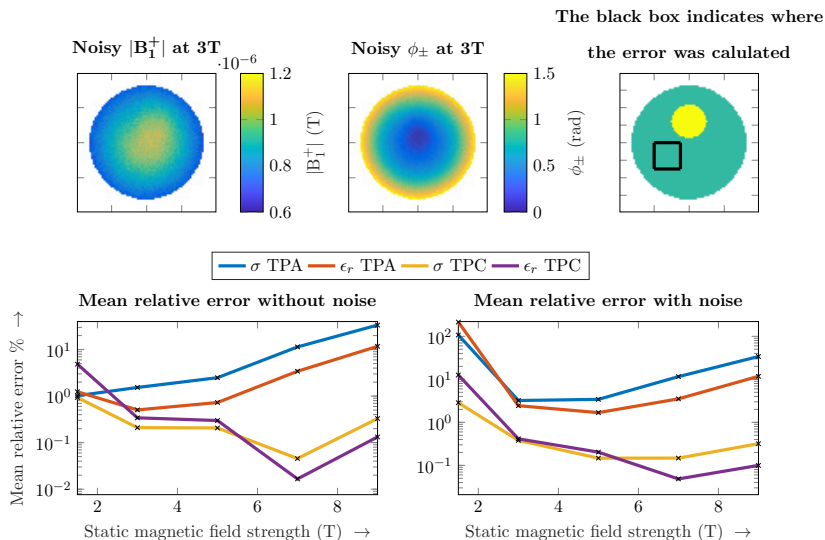


Figure 6.4: The top left shows an example of a simulated noisy B_1^+ amplitude map at 3T. The top middle figure shows the corresponding simulated noisy transceive phase. The top right figure shows where the mean relative error was computed. The bottom row shows the mean relative error in the conductivity and permittivity on a log scale versus the static magnetic field strength, where the left figure is without noise in the simulation and the right figure is with noise. The 3T and 7T reconstructions of these data points can be seen in Figure 6.3.

Figure 6.5 shows the conductivity reconstructions from the 3D FDTD simulations. This is to demonstrate the effect that 3D electromagnetic fields have on the reconstructed contrast since we are using the 2D CSI-EPT. The top left reconstruction is taken from the center slice of the birdcage coil. The subsequent reconstructions are from slices 1cm further out of the middle. All these reconstructions were computed separately as 2D slices and not as a 3D volume.

The bottom plot of Figure 6.5 shows the conductivity value across the reconstructions for the point indicated with the red cross in the top left reconstruction. From this plot, it can be seen that the conductivity value is underestimated. The underestimation increases for more peripheral locations

along the cylindrical axis of the birdcage coil (i.e. moving towards the endrings of the birdcage coil). This arises from the fact that the 2D EM field approximation becomes increasingly more invalid. Furthermore, the phantom is not 2D thus at the end of the phantom the RF field is not 2D E-polarized.

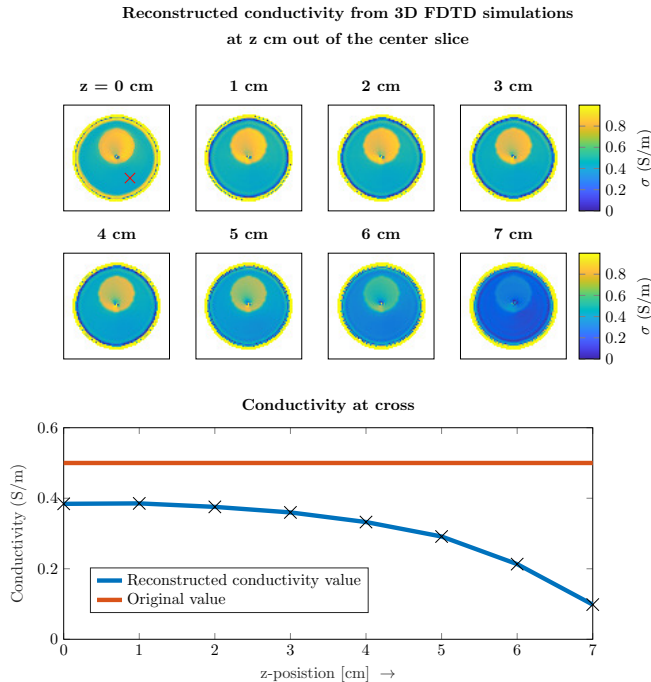


Figure 6.5: The top left figure shows the reconstruction of the conductivity in the center of the birdcage coil for the 3D FDTD simulations. The seven subsequent figures are reconstructions each 1cm more out of the center slice of the birdcage coil. The bottom figure shows the value of the actual conductivity and the reconstructed value at the red cross marked in the top left figure.

Figure 6.6 shows the reconstructed conductivity maps from MRI measured data for the proposed CSI-EPT method and the standard Helmholtz MR-EPT as a reference. For both methods, reconstructions were performed using a number of signal averages (NSA) of 2 and 10. The comparison between the two EPT methods was performed because there is no ground truth of the contrast available, but only an average value based on the NaCl concentrations. With NSA 10, MR-EPT shows good quality maps, while these are noisier for the NSA 2 case. This can also be observed from Table 6.2. Furthermore, we

Table 6.2: Mean and standard deviation (sd) of the conductivity reconstructions from MRI data.

Reconstruction used	mean inner tube	sd inner tube	mean background	sd background
CSI-EPT NSA = 2	0.87	0.17	0.29	0.12
CSI-EPT NSA = 10	0.87	0.05	0.29	0.09
MR-EPT NSA = 2	0.83	0.22	0.42	0.16
MR-EPT NSA = 10	0.81	0.22	0.37	0.13
MR-EPT with boundary NSA = 2	0.6	0.51	0.29	0.7
MR-EPT with boundary NSA = 10	0.63	0.42	0.24	0.68
Reference Value	0.9	-	0.41	-

observe that the standard deviation of the CSI-EPT reconstruction is always lower compared to the MR-EPT reconstruction. Additionally, in both the NSA 2 & 10 reconstructions of the CSI-EPT have the same mean values, while this is not the case for the MR-EPT reconstruction. However, the MR-EPT reconstructs the mean value of the background better than CSI-EPT, which underestimates the conductivity. Nonetheless, this demonstrates the feasibility of CSI-EPT in a realistic setting using data acquired in clinically feasible scan time.

Finally, since the newly proposed method also reconstructs the receive phase during the minimization process, it is possible to compare this reconstructed phase from the measurement with the 2D line source simulated one. This together with the comparison between the 2D simulated transceive phase and the measured transceive phase is shown in Figure 6.7. The simulated, measured, and the reconstructed phases show good agreement. This indicates that the receive phase can be reconstructed using the TPC CSI-EPT.

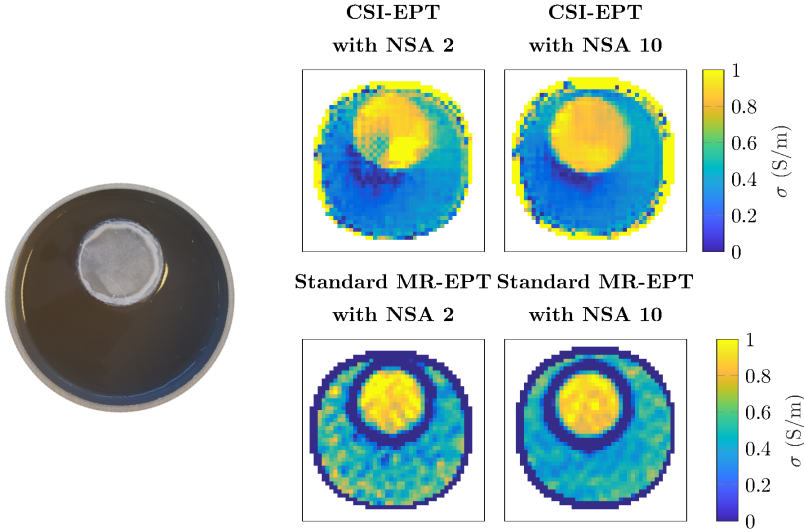


Figure 6.6: On the left is a picture of the phantom that was made for the measurements. The top left shows the conductivity reconstruction for the CSI-EPT reconstruction with an NSA of 2, the top right shows the reconstruction for NSA = 10. The bottom two figures show the standard Helmholtz MR-EPT reconstruction. The left shows the NSA = 2 reconstruction while the right shows the NSA = 10 reconstruction.

6.5 Discussion

In this work, we reformulated the CSI-EPT algorithm in terms of MRI accessible quantities, i.e. the B_1^+ magnitude and the transceive phase. Furthermore, we showed that with this formulation we can derive the true B_1^- fields rather than the relative B_1^- , which is reconstructed by using one transmit channel as a reference. Further, we included a numerical implementation of the RF shield resulting in more realistic incident RF-fields that are used as input for CSI-EPT. Ultimately, with this work we demonstrated for the first time the feasibility of CSI-EPT conductivity reconstructions from MRI measurements at 3T. These results ultimately confirm the reduction of boundary errors and less noise compared to Helmholtz EPT as is always claimed from simulated results.

The solution to the RF-shield was proposed to model the incident RF-fields correctly. Another solution to implement the RF-shield into the CSI-EPT scheme has been proposed in [122], where instead of the free-space Green's

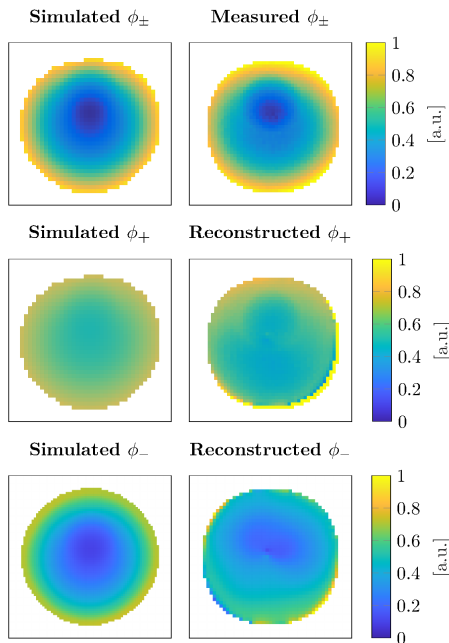


Figure 6.7: The top left left shows the transceive phase from the 2D simulation. The top right shows the transceive phase measured with MRI. The middle left shows the simulated transmit phase and the middle right shows the transmit phase reconstructed by CSI-EPT from the measurement. The bottom row shows the simulated and reconstructed receive phase.

tensor functions the Green's tensor functions in the presence of a circular perfect electrical conductor (PEC), which represents the RF-shield, has been used. This solution showed great improvement, however, the downside of using this method is that the computation time of the CSI-EPT algorithm will increase drastically. Since integral approaches are already slower compared to derivative approaches, we chose to use the implementation proposed in this work, where we only include the RF-shield in the incident RF-fields. For the center slice of the birdcage coil, the two-dimensional RF-fields simulated with line-sources is used and shows similar electrical properties reconstructions compared to reconstructions using FDTD simulated incident RF-fields.

The TPA is valid at lower field strengths, as a result, we can reason that the error in the reconstruction from Figure 6.4 for the lower field strengths is

dominated by the low SNR. For higher field strengths the error in the standard CSI-EPT algorithm increases because the TPA is no longer valid. In Figure 6.3, these effects can also be observed in the electrical properties. In the 3T reconstructions, the error is predominantly due to the low sensitivity, while at the 7T reconstruction more global over and underestimations of the conductivity and permittivity can be seen. When using the TPC CSI-EPT the transceive phase is no longer negatively affecting the reconstruction. Further, we observe that at the lower field strengths the conductivity reconstruction has a lower error compared to the permittivity reconstruction. The displacement current directly scales with the frequency [129]. Therefore, at higher static magnetic field strength, the imprint of the permittivity on the contrast increases, possibly allowing for higher quality permittivity reconstructions at higher field strengths.

With the standard CSI-EPT algorithm and standard Helmholtz EPT, there was a trade-off for the field strength to use when measuring with a standard birdcage setup. At lower field strengths the sensitivity is poor, while at higher field strengths the TPA is not valid. With the TPC CSI-EPT, this trade-off is no longer present since TPC CSI-EPT is not affected by the invalidity of the TPA. Therefore, the increased SNR and inherent sensitivity of 7T for a regular widely available standard quadrature setup can be exploited. As a limitation of this work, MRI measurements were only performed at 3T and not at 7T because the specifications of the transmit coil at 7T are not available. As shown in Figure 6.2, an incorrectly simulated background RF-field would lead to an incorrect contrast reconstruction. Therefore, measuring at 7T without good knowledge of the transmit coil for the simulations would result in poor reconstructions.

In each of the eight reconstructions, in Figure 6.3, it can be noted that reconstruction in the center of the phantom has a larger error compared to the rest of the reconstruction. This is inherently due to the design of the birdcage coil, especially in quadrature and reverse quadrature mode. In these modes, the electric fields constructed by each separate rung of the birdcage coil destructively interfere in the center of the coil creating an electric field that has an almost zero magnitude. This local minimum in the electric field, as can be seen in Figure 6.2, results in a poor reconstruction in this area. To improve this, either a different antenna setup could be chosen to create a different electric field distribution or a dielectric pad could be used to move the local minimum in the electric field [130, 112].

Figure 6.5 shows how realistic three-dimensional electromagnetic fields affect the reconstruction. The center slice of the birdcage coil is the part that resembles a two-dimensional transverse magnetic (TM) polarized field. Slices outside of the center have larger E_x , E_y , and B_z components that are not taken into account in this two-dimensional CSI-EPT algorithm. This is the

cause of the underestimation of the conductivity, as can be seen by the plot at the bottom of Figure 6.5, especially at the outermost slices of the phantom. At the boundary between the phantom and the air, the change in conductivity and permittivity creates three-dimensional scattered fields, and the assumption that the field is TM polarized is no longer valid. The same results were observed for the permittivity, but is omitted here to not display the same information twice.

The phantom has a contrast that is invariant over the z -direction for the length of the phantom. This was done to keep the assumption that the RF field is two-dimensional valid in the center slice of the birdcage coil. In [131], the effects of reconstructing fully three-dimensional contrasts with a two-dimensional CSI-EPT algorithm are shown.

Possible solutions for the underestimation of the dielectric properties is to formulate the CSI-EPT algorithm for three-dimensional RF fields. However, this will significantly increase the computation time of the algorithm. Currently, the reconstructions are obtained within 1 minute of computation time using an i5-6600k processor compared to multiple hours for 3D CSI-EPT [132]. The increase in computation time is a result of the increased problem size and the change in conditioning of the problem, increasing both the time per iteration and the total number of iterations required [132]. If the TPC is used in the 3D implementation of CSI-EPT, the receive phase could be calculated only at every n^{th} iteration to alleviate the additional computational effort. Further, the increase in computation time can be managed by using some form of a hybrid method, where either 2D CSI-EPT or a deep learning approach [133] can be used as initialization for the 3D CSI-EPT method. Another solution could be to use a tube with a reference dielectric during scanning. Then, the results can be scaled until the correct reference value is found.

From the reconstruction of the measured data in Figure 6.6, it is clear that the CSI-EPT reconstruction is more noise robust compared to the standard Helmholtz MR-EPT. Another striking feature is that for EPT a clear boundary error is present while for CSI-EPT this error is not present. This reconstruction of the electrical properties using MRI measured data shows the feasibility of CSI-EPT for the first time. However, for the CSI-EPT, algorithm we observe that for the measured data the conductivity of the background is underestimated and at the outer edge of the phantom the conductivity is overestimated as was expected from the reconstructions of the three-dimensional simulations. Therefore, to improve the reconstructions for MRI measured data similar steps as discussed in the paragraph above should be taken.

From the TPC CSI-EPT, we can also extract the reconstructed transmit and receive phase as shown in Figure 6.7. This was previously not possible and only the transceive phase and the receive fields with respect to a reference channel could be measured. The actual transmit and receive phase maps could

be of interest for coil design and to check the performance of built coils.

Ultimately, the presented methodology enables the use of CSI-EPT for higher field strengths with a standard birdcage setup and as a result of the reformulation to MRI accessible quantities, it could also move to be used for in vivo EPT.

6.6 Conclusion

In this work, the CSI-EPT algorithm was reformulated such that the B_1^+ amplitude and transceive phase can serve as input data instead of the complex B_1^+ field. Due to this reformulation, the transceive phase assumption, which is not valid at high field strengths, is not necessary anymore. This allows for CSI-EPT to fully exploit the benefits of the higher static magnetic field strengths with a standard quadrature birdcage coil setup.

Finally, in this work, the first MRI acquired data CSI-EPT reconstructions are shown and illustrate a significant improvement over the standard Helmholtz MR-EPT reconstructions. Moreover, we observed that CSI-EPT can reconstruct the boundaries between different dielectric properties and that it is robust with respect to realistic SNR values.

Summary

*Peter R.S. Stijnman, Cornelis A.T. van den Berg and
Alexander J.E. Raaijmakers*

For patients with medical implants, it is estimated that 50 to 75% would benefit from having an MRI examination in their lifetime. However, this patient group is not always eligible for an MRI examination since implants interact with the magnetic fields of the MRI system posing a potentially severe safety threat. Especially, first-generation medical implants are often considered MR unsafe rendering the patient ineligible for MRI diagnosis. More recently, implant manufacturers are developing MR-safe and MR-conditional products. The safety assessment of these products takes place according to predefined standards that result in a label defining the constraints for undergoing an MRI examination. In this thesis, we present alternatives to the radiofrequency (RF) safety assessment of MRI-compatible implants.

Of all potential interactions of implants with the MRI system, the interaction of the implant with the RF fields generated by the MRI represents the biggest cause for concern. The implant causes an enhancement of the RF electric field and, therefore, a very localized region of power deposition. When scanning under unconstrained conditions, this local power deposition may result in a hazardous temperature increase. To quantify safe scanning constraints for the patient with implant, the magnitude of power deposition and/or temperature increase needs to be determined.

For this purpose, the so-called transfer function (TF) is defined for elongated implants which is a characteristic function of the implant that describes its interaction with the MRI system RF field. While the MRI system poses a safety concern it is also a versatile measurement system that can be used to quantify this safety concern. Therefore, previous work has presented methodologies to use the MRI system to measure this TF. However, an additional

independent measurement is required to validate the MRI-based TF measurement. This is discussed in the first chapter of the thesis where we present a validation procedure particularly suited for MRI-measured TFs. The method uses local transmit coils to create localized RF fields and fiber-optic temperature probes to measure the response of the implant. Using multiple temperature measurements with the RF coils at different positions we can determine the translation between the RF electric field and the eventual temperature increase. Furthermore, with the TF, the RF electric field from the local RF coils, and the temperature measurements we can determine the validity of the TF. Therefore, combined with previously developed methods, we can both measure and validate the TF inside the MRI environment inside a single experimental setup.

A downside of the TF is that it is only defined for elongated implants; for a wide variety of implants, the TF approach for the RF safety assessment is not possible. Furthermore, the TF approach relies on data measured in a phantom setup and is used to calculate scanning constraints that are safe for every possible scenario. As a result, for every patient the same (worst-case) scanning constraints will be used, i.e. the inter-subject variability is not taken into account. As an alternative, using an online subject-specific RF safety assessment approach that does not utilize the TF, scanning constraints may likely be relaxed for the majority of patients. In addition, it may enable the scanning of non-labelled implants.

For an online RF safety assessment, a method for extremely fast calculation of RF field enhancement near implants is required. For this purpose, we present a method that decouples the problem of the patient/MRI system and the implant. This method updates full-wave electromagnetic simulations of the patient without an implant to include the effect of the implant. This is done through a domain decomposition to calculate the induced currents inside the implant, which results in highly accurate RF field simulations in an accelerated fashion. This calculation method was previously demonstrated for high permittivity dielectric pads used in RF field shimming. Therefore, we first demonstrate the feasibility of the original method for calculating the RF field enhancement near implants. We have shown that we were able to calculate this RF field enhancement 171 to 2478 times faster than traditional FDTD methods, within a 1.35% error margin.

The downside of the original method is that the method requires an RF field distribution with the implant present and a simulation set of simulations containing the RF electric and magnetic field distributions originating from a source on the edges of every voxel location where the implant will be present. Particularly, the latter requires a prohibitively large time investment and memory storage. Therefore, we greatly increased the applicability of the proposed method by developing an online calculation approach for electromagnetic field

distributions, which removes a large part of the simulation work that needs to be done beforehand. As a result, the method now only requires the implant geometry, electrical properties of the implant, location within the subject, and a background RF field distribution without the implant. By removing the need for this simulation set we were able to leverage GPU hardware acceleration to retain an acceleration factor of 55 to 438 compared to traditional FDTD simulation times.

Finally, the potential of the improved method for patient-specific RF safety assessment is demonstrated retrospectively for three patients with orthopedic implants that underwent MRI examination at the UMC Utrecht. Original clinical X-ray images of these patients were used to generate a three-dimensional model of the implant within the patient after which RF field enhancement is calculated for each of these patients.

A caveat that the proposed method has is that for the calculation of the background RF field distribution a generic body model instead of the actual patient anatomy is used. This discrepancy may cause inaccuracies in the predicted RF field enhancement. Therefore, we have worked on a method for the acquisition of the conductivity and permittivity of the patient anatomy, which would enable subject-specific calculations of the background field. For this purpose, the contrast-source inversion electrical properties tomography (CSI-EPT) method was reformulated. The method originally required the B_1^+ magnitude and phase inside the patient in order to reconstruct the dielectric. However, the phase component is not measurable with MRI since it is coupled with the B_1^- phase. Through reformulating the reconstruction algorithm, we can incorporate this additional phase component and use MRI measurable quantities to reconstruct the required dielectric properties distribution.

General discussion

*Peter R.S. Stijnman, Cornelis A.T. van den Berg and
Alexander J.E. Raaijmakers*

In this thesis, we have developed several new tools to utilize in the assessment of the RF safety of medical implants in MRI. These tools have application in measurement validation, simulation procedure, and MR imaging. Using these tools it is possible to obtain more insight into the RF interaction between the MRI system, the patient, and the implant. Ultimately, this gained insight can be used to maximize the applicability of the MRI system for patients with implants, either by alleviating any conservative scanning restrictions or by making patients with non-labelled implants eligible for MRI examination.

8.1 Transfer function validation

The transfer function (TF) is a property that is defined for elongated implants and is used to calculate the RF electric field enhancement near the implant [16]. In previous work, by Tokaya et al a method was developed to measure the TF using MRI [17, 18]. A key component that was missing was the validation of this TF measurement. The validation of the TF is an important step to verify that measurement of the TF was done correctly and any scanning constraints based on the TF ensure the safety of the patient. For this reason, we have developed a method in this work that can validate the TF using local transmit RF coil and fiber-optic temperature probes inside the MRI system. This validation method is especially well suited for the validation of the MRI measured TF since both the measurement and validation can be done within the same MRI-phantom setup.

Using local transmit RF coils for this validation method has significant

benefits. The biggest practical benefit is that the incident RF field can be varied without changing the trajectory of the implant. Therefore, the distance between the tip of the implant and the temperature probe does not change. The correct placement of the tip of the implant and the temperature probe is a potential source for large errors because the gradient in the temperature hotspot at the tip of the implant is very steep [30]. Therefore, a small change in this relative distance can result in a wrong temperature increase. Another benefit is that this validation can be done easily inside of the MRI environment using the same setup as for the measurement, saving time in creating different measurement and validation setups. With the benefits obtained by using local transmit coils, we showed a high correlation between the measured and calculated temperature values for the four different elongated implants that were tested.

Ultimately, the MRI-based TF measurement would be used *in vivo*. Using a low SAR scan the TF of the implant inside the patient anatomy could be measured. This could be a solution for patient-specific RF safety assessment. However, to achieve this goal multiple challenges of the TF measurement method need to be solved. The two biggest problems are obtaining the *in vivo* RF fields without the implant present and the TF determination for leads with a coiled trajectory.

The validation method presented in this work would not work for the validation of an *in vivo* measured TF since there is no (well-tolerated) way to use fiber-optic temperature probes inside a patient. MR thermometry might work when the image artefact created by the implant is negligible. However, it would not be practical nor ethical to perform a validation measurement for an *in vivo* measured TF. Rather, the proposed validation method can serve as a validation for the TF measurement technique itself by demonstrating with the independent temperature measurements that the TF measurement acquires the correct TF for different phantom setups (i.e. different implants, lead trajectories, and dielectric surroundings). This could also include phantom setups with multiple compartments that each contain a gel with different electrical properties to better mimic the heterogenous electrical properties distribution in patients. Furthermore, such phantom setups can investigate the effects that different electrical property distributions have on the TF itself. These multiple compartments are currently not required for an MRI label. There measurements must be performed in a phantom with a low, medium, and high conductivity gel.

A downside of this MRI-based measurement and validation methodology is that it is more expensive compared to non-MRI-based measurement methods. However, having the entire measurement and validation setup inside the MRI adds extra confidence that no additional changes are to be expected, with respect to measuring outside the MRI system. Furthermore, such a TF

measurement and validation can be combined with an MR measurement to quantify the susceptibility artefact created by the implant, all in one phantom setup.

8.2 Accelerating RF simulations for implants

One big downside of the TF is that it is a property only defined for the elongated implants or implants with leads. However, there is a wide variety of implants for which there is no TF defined since they are not elongated or contain leads. Therefore, the simplification of using the TF to calculate the RF electric field enhancement cannot be used. As a result, we have to calculate/simulate the interaction of the implant with the MRI system and the patient using for example FDTD, FEM, or FIM simulations. The benefit of using these simulations is that they produce more accurate results. The reason why the TF approach is used instead of these full-wave simulations is that the computational burden is significantly lower. An RF field enhancement calculation with the TF approach can be done in seconds, whereas the full-wave simulations take hours [20, 81]. If the full-wave simulations can be drastically accelerated, a lot of new approaches become available.

To accommodate this, we developed a method to calculate the scattered RF fields as a result of the implant in an extremely quick fashion, which we have called the ‘update method’ throughout this work. The premise for this fast calculation technique is that it only calculates the effect of a small perturbation within a larger simulation setup. In our specific case, this perturbation is the implant itself, which is small compared to the entire patient anatomy and the MRI system.

In our initial approach, we showed the applicability of this update method on the RF safety assessment of implants there was a requirement to perform another simulation set beforehand, the so-called library matrix. This library matrix quickly becomes intractable as is shown in the work presented here. To circumvent this problem and make the method more “plug and play” we made a version of the method where this library matrix is no longer required. This was achieved by using a matrix-free minimization strategy to solve the matrix inverse. This matrix-free minimization is computationally more expensive compared to the case when the library matrix is explicitly known. If the library matrix is explicit a simple matrix-vector multiplication is performed each iteration when solving the Sherman-Morrison-Woodbury formula. However, the increase in online calculation time is offset by the vast advantages of reduced memory requirements and initial time investment.

The function that is used to enable the matrix-free minimization is a volume integral equation that solves for the RF field inside the patient anatomy when all the sources placed on the edges occupied by the implant are switched

on at the same time. The benefits of this reformulation of the method are that the method does not require an extensive simulation set to be performed beforehand. Furthermore, it is possible to update an RF field distribution calculated in any arbitrary background electrical properties distribution at any frequency. If an explicit library matrix is used, a new library matrix for each different human body model needs to be calculated. Finally, because of the lower memory requirements of the matrix-free minimization, it is possible to use GPU hardware acceleration, leveraging part of the computational complexity. These benefits greatly improve the applicability of the update method.

8.2.1 Applications

In this manuscript, we showed one such application, the workflow for patient-specific RF safety assessment. Using orthogonal X-ray projections we showed that it is possible to make a three-dimensional model of the implant geometry, using some *a priori* knowledge, and extract the location within the patient anatomy. This information about the implant combined with a simulated RF field distribution without the implant allowed us to quickly evaluate the increase in the RF electric field, and thereby the increase in the 1 g averaged SAR, for different implant and patient positions. We envision this workflow to be performed in the days before a patient comes in for an MRI examination.

In that time the three-dimensional model of the implant can be constructed from the X-ray images and the RF field distributions for different configurations can be calculated. These different configurations are required because there is some uncertainty in the location of the implant inside the patient's anatomy, the implant geometry, and the position of the patient within the MRI system [134, 135]. To account for these uncertainties, we can calculate the RF field distribution near the implant for slight variations of the configuration. Using the calculated RF field distributions we can determine a range for the expected increase in maximum 1 g averaged SAR. Based on that information the scanning restrictions for that specific patient can be determined.

The problem currently is to determine the number of different configurations for which the RF field distribution needs to be calculated. In this work, we accounted for the uncertainty in the positions of the implant and patient by calculating the RF field distribution for 27 different implant positions (i.e. a 1 voxel shift in all directions) and 5 different patient positions. Only a 1 voxel shift in all directions was chosen for the implant because of the quality of the X-ray images that were used. The implant is clearly distinguishable and the resolution of the X-ray images was finer than that of the electromagnetic simulation. The number of patient positions could be increased when it is not known what the exact location inside the scanner will be, however for this proof of concept work we limited the study to 5 different positions and did not vary the anterior-posterior position since the table in the MRI is at one

specific height.

Using the 1 g averaged SAR increase obtained from this workflow, an informed decision can be made on what the patient-specific scanning restrictions with respect to the global SAR level would be. This would alleviate the scanning restrictions for a large portion of the patient group resulting in shorter scan times or better image quality.

Furthermore, it would allow smaller hospitals without specific expertise on RF interactions to scan patients with non-labelled implants. Even in the hospitals where they normally scan this patient group often extra scan time, sometimes two or three scan slots, is reserved such that the patient can be scanned with a lower global SAR level to minimize any potential heating. Using the proposed workflow might alleviate the need for extended time slots, which may also prove beneficial for the hospitals that do scan non-labelled implants. In addition, the method provides implant safety experts with valuable information to make decisions.

For labelled implants, this proposed workflow could also be used to alleviate scanning restrictions. This could potentially result in shorter scan times and/or better image quality. However, the potential gain might not be worth the effort. Especially because there already is a label, many hospitals may see no reason to deviate from the predetermined safe scanning restrictions.

Before this workflow can be adopted by hospitals there are some steps that need to be taken. The first would be to automate the workflow such that human interaction is only required in the quality assurance phase of the workflow. To achieve this the X-ray images need to be automatically segmented. This is a trivial task since the implant is very distinguishable from the rest of the image. Afterward, the step from two-dimensional masks to a three-dimensional model is required. One solution to this problem could be to use a library of three-dimensional models for a wide range of known implants. Another solution could be to use deep learning to create a three-dimensional model from the two-dimensional masks. There are some neural networks that can perform such tasks, especially, in the area of computer vision [91, 90, 89, 88]. Such a network could be trained to perform this task at hand. In order to train the network multiple three-dimensional models of implants are required such that a training, test, and validation dataset can be constructed. It might also be possible that currently available trained networks already perform well enough for this task or using a trained network it is possible to use transfer learning and a smaller dataset of three-dimensional implant models to achieve satisfactory results.

After the implant model has been made it should be placed inside the simulation configuration at the same location as inside the patient anatomy. This could either be automatically inferred from the X-ray images by using the skeletal structures that are visible or some predefined landmarks could be

manually assigned inside the X-ray images to position the implant model.

An improvement that could be made is to incorporate the subject-specific patient anatomy in the RF simulations of the background fields. Currently, the patient anatomy is not available inside the simulation environment, and rather a standard human body model from the virtual family is used. The body model that most resembles the patient should be chosen to perform the simulations to obtain the best results. Using the update method it would be possible to incorporate the actual patient anatomy, however, obtaining the dielectric properties of the patient anatomy is still an active area of research [136]. This will be discussed more in detail in the next section.

After the workflow is automated such that the tool is easy to use and understand, there needs to be a validation procedure. This validation procedure should include testing the accuracy of the automated workflow step by step. Furthermore, the impact of small deviations or errors made during the workflow should be investigated. For example, if a small error in the implant position is made how does this translate to the eventual calculated scanning restrictions? Such a validation procedure is important because it will give more insight into the exact workings of the workflow and to which parts of the pipeline extra care should be taken to ensure a correct result, i.e. safe scanning restrictions, in the end.

When the validation procedure has been performed an introduction into the clinic should be possible. Ideally, this should be done by either an existing MRI software tools company or a new startup company. The proposed workflow could then be sold as a service to different hospitals. The hospital would submit the X-ray images, the imaging landmark, and the implant type if known. By having a company provide this service the liability would be at the company, which would alleviate the legal objections of smaller hospitals to scan patients with non-labelled implants.

For a possible introduction, the hospitals that have experience with scanning patients with (non-labelled) implants test the proposed workflow first. They would benchmark their knowledge about the RF safety of implants against the result of the workflow and could choose to scan patients with a higher global SAR level. If the feedback is positive the workflow could be extended to hospitals where there is less or no experience with scanning this patient group. In this way they could, first of all, gain more experience and confidence in scanning these patients. This would benefit patients because they would not have to travel to another hospital and wait for scan time there.

Next to the application that we have described in detail in this work, there are more possible applications within the MRI RF safety assessment area of research as well as outside of the MRI world. For more implant RF safety assessment applications, it would be possible to use this tool to accelerate the so-called Tier 4 safety assessment as described in the ISO/TS-10974 [14].

Another application for the implant RF safety assessment could be to use the update method during the design phase of a new implant. Enabling quick simulations on the RF safety of a current design or changes to a design can give a lot of insight into the makings of an MRI-safe implant. Using the update method different geometries of the implant or different material choices could be investigated. This could allow the easier development of implants that are either inherently safe for MRI use or would obtain a lenient MRI-conditional label.

Finally, we have shown that the update method does not only apply to the RF safety assessment of implants in MRI. The method works for any electromagnetic simulation problem where multiple configurations with small perturbations are required to be simulated.

8.2.2 Further improvements

Other than applications of the update method, there are also still some concepts that could warrant further research into improving the method itself. One such concept is the use of deep learning to accelerate the minimization of the matrix inverse that needs to be calculated. Currently, the minimization is performed according to the GMRES scheme. While this is a robust method to perform the matrix inversion the cost of each additional iteration that is required is more expensive than the last. Therefore, it is slower compared to a conjugate gradient method. At each iteration of a conjugate gradient method minimization, a gradient and a step size are calculated based on the current residual of the cost function. While this is cheaper and faster than using GMRES it is prone to local minima [120]. As an alternative, a neural network can be introduced to add information on the specific problem that is being solved (i.e. electromagnetics). The conjugate gradient method is a generic solver that can work on all problems. However, given knowledge about the physics of the problem, it is possible to reach the (global) minimum faster [137, 138, 139].

For such a neural network the inputs would be the current estimate of the solution and the gradient at that current estimate, x and $\nabla f(x)$ respectively. Using that information either separate iterations could be learned for the neural network (i.e. for every iteration you would obtain a neural network with different coefficients) or a recurrent neural network could be learned. Effectively, the neural network will learn the specifics of solving the minimization problem at hand. The benefit of doing this would be to decrease the total number of iterations that are required to solve the minimization problem, thereby solving the problem faster (i.e. in the order of (sub-)seconds). This is visualized in Figure 8.1.

The same strategy of using a neural network could be applied to the volume integral equation solver which is based on a minimization process too. The gain here would be that each individual iteration of the minimization for the

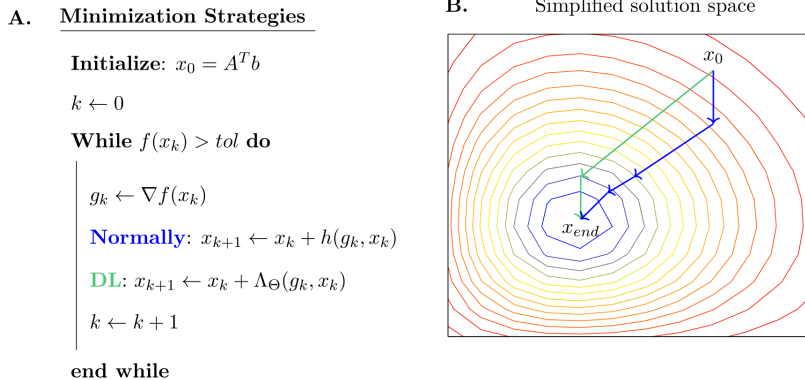


Figure 8.1: The algorithm on the left shows how the costfunction is minimized. Where the choice can be made to compute a descent direction and stepsize using tradition method, $h(g_k, x_k)$, or with the help of a neural network, $\Lambda_{\Theta}(g_k, x_k)$. On the right is a hugely simplified visualization of a solution space. However, it clearly depicts where the potential gain for a deep learning solution would be, i.e. fewer iterations are required.

matrix inverse would be calculated faster, resulting in even more acceleration for this method compared to traditional simulation techniques.

8.3 Electrical properties tomography

To accurately calculate the RF electric field enhancement it would be ideal to have the patient-specific electrical properties distribution. These electrical properties affect both the background RF field distribution and the interaction of the implant with the RF field. However, obtaining the patient-specific electrical properties distribution is a difficult task. Therefore, the final tool that we have worked on is a method to retrieve the conductivity and permittivity of the patient anatomy from MRI measurable quantities. These electrical properties are also considered a potential biomarker in oncology.

In this work, we focussed on the contrast source inversion electrical properties tomography (CSI-EPT) method. This is an integral-based method that uses the B_1^+ distribution to retrieve the electrical properties. Both the magnitude and phase of the B_1^+ field are required. The problem is that the phase component is not directly measurable with MRI. The phase that can be measured is the transceive phase, the sum of the B_1^+ and B_1^- phases. This problem was solved by calculating the B_1^- phase at each iteration of the minimization process, rather than using the transceive phase assumption.

While the presented work here exploits the RF field structure in the center-plane of a birdcage coil it will also extend towards a fully three-dimensional implementation of CSI-EPT. The downside with solving the full three-dimensional problem is that it takes hours to run a single reconstruction. To alleviate this the problem could be solved using a GPU where, due to the hardware architecture, a significant speedup can be expected. The implementation of the functions is very similar to the update method shown before, which already supports GPU acceleration for those specific functions (i.e. Green's functions). Therefore, this reconstruction time problem is not the main limiting factor for the implementation of the presented method.

A more pressing problem is the requirement of the RF field distributions that are generated inside the MRI when it is unloaded, i.e. RF incident fields [136]. It would be possible to simulate this RF field if the current distributions on the RF coil were available, but they are not easily accessible. The closest proxy that is available is the power that is delivered to the ports of the RF coil. However, the resulting current distribution between a loaded and unloaded coil is significantly different and will affect the conductivity and permittivity maps.

While this remains a problem it is more likely that a different reconstruction method would work better to find the electrical properties. A very promising candidate here is a deep learning approach, that given the B_1^+ distribution retrieves the electrical properties in a single forward pass [140, 141]. This is both very fast and such a network can learn the behavior of a specific RF coil. This has already been demonstrated and shows great potential. However, as with all deep learning solutions, they should be as generalizable as possible. Entailing it should work on any measured B_1^+ distribution using any RF coil.

To benefit the generalization of a deep learning solution, the network should only solve the part that is not understood by humans or that which cannot be measured. In the case of electrical properties tomography, the latter is true. Therefore, a deep learning solution that uses as much information about the physics behind the problem would result in the most robust, general, and easy-to-train neural network. Therefore, the work presented here using CSI-EPT is still very useful as it can perfectly complement a deep learning solution [142, 143].

Ultimately, the tools that we have shown in this work should serve as a stepping stone towards a better understanding of the RF field distributions inside the MRI system. For the RF safety assessment of implants or the RF safety of MRI in general.

Bibliography

- [1] Robert A. Bell. Economics of MRI technology. *Journal of Magnetic Resonance Imaging*, 6(1):10–25, 1996.
- [2] M.F. Dempsey, B Condon, and D.M. Hadley. MRI safety review. *Seminars in Ultrasound, CT and MRI*, 23(5):392–401, 2002.
- [3] Winter L, Seifert F, Zilberti L, Murbach M, and Ittermann B. MRI-related heating of implants and devices: A review. *J Magn Reson Imaging*, 2020.
- [4] R. Srinivasan, C.W. So, N. Amin, D. Jaikaransingh, F. D’Arco, and R. Nash. A review of the safety of MRI in cochlear implant patients with retained magnets. *Clinical radiology*, 74(12):972–e9, 2019.
- [5] Erhardt JB, Fuhrer E, Gruschke OG, et al. Should patients with brain implants undergo MRI? *J Neural Eng*, 15(4):041002, may 2018.
- [6] J.A. Nyenhuis, Sung-Min Park, R. Kamondetdacha, A. Amjad, F.G. Shellock, and A.R. Rezai. MRI and implanted medical devices: basic interactions with an emphasis on heating. *IEEE Transactions on Device and Materials Reliability*, 5(3):467–480, 2005.
- [7] Jana G. Delfino, Daniel M. Krainak, Stephanie A. Flesher, and Donald L. Miller. MRI-related fda adverse event reports: A 10-yr review. *Medical Physics*, 46(12):5562–5571, 2019.
- [8] R.E. Watson. Lessons learned from MRI safety events. *Curren Radiology Reports*, 3, 2015.
- [9] J.A. Nyenhuis, A.V. Kildishev, J.D. Bourland, K.S. Foster, G. Graber, and T.W. Athey. Heating near implanted medical devices by the MRI RF-magnetic field. *IEEE Transactions on Magnetics*, 35(5):4133–4135, 1999.

- [10] Peter Nordbeck, Florian Fidler, Ingo Weiss, Marcus Warmuth, Michael T. Friedrich, Philipp Ehses, Wolfgang Geistert, Oliver Ritter, Peter M. Jakob, Mark E. Ladd, Harald H. Quick, and Wolfgang R. Bauer. Spatial distribution of RF-induced e-fields and implant heating in MRI. *Magn Reson Med*, 60(2):312–319, 2008.
- [11] A Arduino, U Zanovello, J Hand, L Zilberti, R Brühl, M Chiampi, and O Bottauscio. Heating of hip joint implants in MRI: The combined effect of RF and switched-gradient fields. *Magnetic Resonance in Medicine*, 85(6):3447–3462, 2021.
- [12] J Wooldridge, A Arduino, L Zilberti, U Zanovello, M Chiampi, V Clementi, and O Bottauscio. Gradient coil and radiofrequency induced heating of orthopaedic implants in MRI: influencing factors. *Physics in Medicine & Biology*, 66(24):245024, dec 2021.
- [13] Ron Kalin and Marshall S. Stanton. Current clinical issues for MRI scanning of pacemaker and defibrillator patients. *Pacing and Clinical Electrophysiology*, 28(4):326–328, 2005.
- [14] ISO TS 10974. Assessment of the safety of magnetic resonance imaging for patients with an active implantable medical device. *International Organization for Standardization*, 2018.
- [15] ASTM F2182-19e2. Standard test method for measurement of radio frequency induced heating on or near passive implants during magnetic resonance imaging. *ASTM International*, 2019.
- [16] Park SM, Kamondetdacha R, and Nyenhuis JA. Calculation of MRI-induced heating of an implanted medical lead wire with an electric field transfer function. *J Magn Reson Imaging*, 26(5):1278–1285, 2007.
- [17] Tokaya JP, Raaijmakers AJE, Luijten PR, and van den Berg CAT. MRI-based, wireless determination of the transfer function of a linear implant: Introduction of the transfer matrix. *Magn Reson Med*, 2018.
- [18] Janot P. Tokaya, Alexander J.E. Raaijmakers, Peter R. Luijten, Alessandro Sbrizzi, and Cornelis A.T. van den Berg. MRI-based transfer function determination through the transfer matrix by jointly fitting the incident and scattered field. *Magn Reson Med*, 83(3):1081–1095, 2020.
- [19] C.E. McElcheran, L. Golestanirad, M.I. Iacono, P.S. Wei, B. Yang, K.J.T. Anderson, G. Bonmassar, and S.J. Graham. Numerical simulations of realistic lead trajectories and an experimental verification support the efficacy of parallel radiofrequency transmission to reduce heating of deep brain stimulation implants during MRI. *Scientific Reports*, 9, 2019.

-
- [20] Bastien Guerin, Peter Serano, Maria Ida Iacono, Todd M. Herrington, Alik S. Widge, Darin D. Dougherty, Giorgio Bonmassar, Leonardo M. Angelone, and Lawrence L. Wald. Realistic modeling of deep brain stimulation implants for electromagnetic MRI safety studies. *Physics in Medicine & Biology*, 63, 2018.
- [21] Golestanirad L, Iacono MI, Keil B, et al. Construction and modeling of a reconfigurable MRI coil for lowering SAR in patients with deep brain stimulation implants. *Neuroimage*, 147:577–88, 2017.
- [22] Panych LP and Madore B. The physics of MRI safety. *J Magn Reson Imaging*, 47(1):28–43, 2018.
- [23] Rezai AR, Finelli D, Nyenhuis JA, et al. Neurostimulation systems for deep brain stimulation: In vitro evaluation of magnetic resonance imaging-related heating at 1.5 Tesla. *J Magn Reson Imaging*, 15(3):241–250, 2002.
- [24] Henderson JM, Phillips M, Tkach J, Rezai AR, Baker K, and Shellock FG. Permanent neurological deficit related to magnetic resonance imaging in a patient with implanted deep brain stimulation electrodes for parkinson’s disease: Case report. *Neurosurgery*, 57(5):E1063–E1063, 11 2005.
- [25] Bhusal B, Bhattacharyya P, Baig T, Jones S, and Martens M. Measurements and simulation of RF heating of implanted stereo-electroencephalography electrodes during MR scans. *Magn Reson Med*, 80(4):1676–1685, 2018.
- [26] Zastrow E, Capstick M, Cabot E, and Kuster N. Piece-wise excitation system for the characterization of local RF-induced heating of AIMD during MR exposure. In *2014 International Symposium on Electromagnetic Compatibility, Tokyo*, pages 241–244, May 2014.
- [27] Missoffe A and Aissani S. Experimental setup for transfer function measurement to assess RF heating of medical leads in MRI: Validation in the case of a single wire. *Magn Reson Med*, 79(3):1766–1772, 2018.
- [28] Tokaya JP, Raaijmakers AJE, Luijten PR, Bakker JF, and van den Berg CAT. MRI-based transfer function determination for the assessment of implant safety. *Magn Reson Med*, 78(6):2449–2459, 2017.
- [29] Kozlov M, Horner M, and Kainz W. Modeling radiofrequency responses of realistic multi-electrode leads containing helical and straight wires. *Magn Reson Mater Phy*, 11 2019.

- [30] Kozlov M and Kainz W. Effect of temperature sensor location and measurement time on evaluation of the calibration factor of the lead electromagnetic model. In *2019 IEEE International Symposium on Antennas and Propagation and USNC-URSI Radio Science Meeting*, pages 765–766, 2019.
- [31] Yao A, Zastrow E, and Kuster N. Test field diversification method for the safety assessment of RF-induced heating of AIMDs during 1.5-T MRI. In *25th International Society for Magn Reson Med (ISMRM); Conference Location: Honolulu, HI, USA; Conference Date: April 22-27, 2017; Conference lecture*, 2017.
- [32] van Gemert J, Brink W, Webb A, and Remis R. An efficient methodology for the analysis of dielectric shimming materials in magnetic resonance imaging. *IEEE Trans Med Imaging*, 2017.
- [33] Webb AG. Dielectric materials in magnetic resonance. *Concept Magn Reson A*, 38A(4):148–184, 2011.
- [34] Overall WR, Pauly JM, Stang PP, and Scott GC. Ensuring safety of implanted devices under MRI using reversed RF polarization. *Magn Reson Med*, (3):823–33, 2010.
- [35] Eryaman Y, Akin B, and Atalar E. Reduction of implant RF heating through modification of transmit coil electric field. *Magn Reson Med*, 65(5):1305–1313, 2011.
- [36] McElcheran CE, Yang B, Anderson KJ, Golestanirad L, and Graham SJ. Investigation of parallel radiofrequency transmission for the reduction of heating in long conductive leads in 3 Tesla magnetic resonance imaging. *PLoS One*, 10(8), 2015.
- [37] Roemer RB. The local tissue cooling coefficient: A unified approach to thermal washout and steady-state ‘perfusion’ calculations. *Int J Hyperthermia*, 6(2):421–430, 1990.
- [38] Arlinghaus S. *Practical handbook of curve fitting*. CRC press, 1994.
- [39] Neufeld E, Kühn S, Szekely G, and Kuster N. Measurement, simulation and uncertainty assessment of implant heating during MRI. *Phys Med Biol*, 54(13):4151–4169, 2009.
- [40] Erik Morre Pedersen, Erling Falk, Firat Duru, Peter Boesiger, Peter Mortensen, Reto Candinas, Roger Luechinger, and Volkert A. Zeijlemaker. In vivo heating of pacemaker leads during magnetic resonance imaging. *European Heart Journal*, 26(4):376–383, 11 2004.

- [41] Harald Kugel, Christoph Bremer, Marco Püschel, Roman Fischbach, Horst Lenzen, Bernd Tombach, Hugo Van Aken, and Walter Heindel. Hazardous situation in the MR bore: induction in ECG leads causes fire. *European Radiology*, 13(4):690–694, Apr 2003.
- [42] M. Kozlov and W. Kainz. Sensitivity of the transfer function of a helix lead on the dielectric properties of the surrounding media: A case study. In *2017 IEEE International Conference on Microwaves, Antennas, Communications and Electronic Systems (COMCAS)*, pages 1–6, Nov 2017.
- [43] Robert W. Gray, W. Timothy Bibens, and Frank G. Shellock. Simple design changes to wires to substantially reduce MRI-induced heating at 1.5 T: implications for implanted leads. *Magnetic Resonance Imaging*, 23(8):887 – 891, 2005.
- [44] Paul A. Bottomley, Ananda Kumar, William A. Edelstein, Justin M. Allen, and Parag V. Karmarkar. Designing passive MRI-safe implantable conducting leads with electrodes. *Medical Physics*, 37(7Part1):3828–3843, 2010.
- [45] Ali R. Rezai, Kenneth B. Baker, Jean Tkach, John D. Hall, John A. Nyenhuis, and Frank G. Shellock. Reduction of magnetic resonance imaging-related heating in deep brain stimulation leads using a lead management device. *Operative Neurosurgery*, 57(4):392–97, 10 2005.
- [46] Peter Nordbeck, Ingo Weiss, Philipp Ehse, Oliver Ritter, Marcus Warmuth, Florian Fidler, Volker Herold, Peter M. Jakob, Mark E. Ladd, Harald H. Quick, and Wolfgang R. Bauer. Measuring RF-induced currents inside implants: Impact of device configuration on MRI safety of cardiac pacemaker leads. *Magn Reson Med*, 61(3):570–578, 2009.
- [47] Torsten Sommer, Christian Vahlhaus, Gerhard Lauck, Alexander v. Smekal, Marcus Reinke, Ulrich Hofer, Wolfgang Block, Frank Träber, Christian Schneider, Jürgen Gieseke, Werner Jung, and Hans Schild. MR imaging and cardiac pacemakers: In vitro evaluation and in vivo studies in 51 patients at 0.5 T. *Radiology*, 215(3):869–879, 2000.
- [48] Eugenio Mattei, Michele Triventi, Giovanni Calcagnini, Federica Censi, Wolfgang Kainz, Gonzalo Mendoza, Howard I. Bassen, and Pietro Bartolini. Complexity of MRI induced heating on metallic leads: Experimental measurements of 374 configurations. *BioMedical Engineering OnLine*, 7(1):11, Mar 2008.

- [49] Lukas Winter, Peter Kellman, Wolfgang Renz, Andreas Gräßl, Fabian Hezel, Christof Thalhammer, Florian von Knobelsdorff-Brenkenhoff, Valeriy Tkachenko, Jeanette Schulz-Menger, and Thoralf Niendorf. Comparison of three multichannel transmit/receive radiofrequency coil configurations for anatomic and functional cardiac MRI at 7.0t: implications for clinical imaging. *European Radiology*, 22(10):2211–2220, Oct 2012.
- [50] Allen Taflove, Susan C. Hagness, and Melinda Picket-May. *Computational Electromagnetics: The Finite-Difference Time-Domain Method*. Elsevier Inc, 12 2005.
- [51] Eugenia Cabot, Tom Lloyd, Andreas Christ, Wolfgang Kainz, Mark Douglas, Gregg Stenzel, Steve Wedan, and Niels Kuster. Evaluation of the RF heating of a generic deep brain stimulator exposed in 1.5 T magnetic resonance scanners. *Bioelectromagnetics*, 34(2):104–113, 2013.
- [52] Yacine Noureddine, Oliver Kraff, Mark E. Ladd, Karsten H. Wrede, Bixia Chen, Harald H. Quick, Gregor Schaefer, and Andreas K. Bitz. In vitro and in silico assessment of RF-induced heating around intracranial aneurysm clips at 7 Tesla. *Magnetic Resonance in Medicine*, 79(1):568–581, 2018.
- [53] C.A. Balanis. *Advanced engineering electromagnetics*. John Wiley & Sons, Inc., 2nd edition edition, 2012.
- [54] Eugenia Cabot, Earl Zastrow, and Niels Kuster. "safety assessment of AIMDs under MRI exposure: Tier3 vs. tier4 evaluation of local RF-induced heating". *Electromagnetic Compatibility proceedings*, 2014.
- [55] Gene H. Golub and Charles F. van Loan. *Matrix Computations*. John Hopkins Universtiy Press, 4th edition edition, 2013.
- [56] Jeff Bezanson, Stefan Karpinski, Viral B. Shah, and Alan Edelman. Julia: A fast dynamic language for technical computing. *CoRR*, abs/1209.5145, 2012.
- [57] Kezhong Zhao, M.N. Vouvakis, and Jin-Fa Lee. The adaptive cross approximation algorithm for accelerated method of moments computations of emc problems. *IEEE Transactions on Electromagnetic Compatibility*, 47(4):763–773, 2005.
- [58] José M. Tamayo, Alexander Heldring, and Juan M. Rius. Multilevel adaptive cross approximation (mlaca). *IEEE Transactions on Antennas and Propagation*, 59(12):4600–4608, 2011.
- [59] OECD. Magnetic resonance imaging MRI exams (indicator), 2021.

- [60] Harry G. Mond and Ian Crozier. The Australian and New Zealand cardiac implantable electronic device survey: Calendar year 2017. *Heart, Lung and Circulation*, 28(4):560–566, 2019.
- [61] Steven M. Kurtz, Jorge A. Ochoa, Edmund Lau, Yakov Shkolnikov, Behzad B. Pavri, Daniel Frisch, and Arnold J. Greenspon. Implantation trends and patient profiles for pacemakers and implantable cardioverter defibrillators in the United States: 1993–2006. *Pacing and Clinical Electrophysiology*, 33(6):705–711, 2010.
- [62] A. John Camm and Seah Nisam. European utilization of the implantable defibrillator: has 10 years changed the ‘enigma’? *EP Europace*, 12(8):1063–1069, 08 2010.
- [63] Massimo Zecchin, Marina Torre, Eugenio Carrani, Letizia Sampaolo, Enrico Ciminello, Benedetta Ortis, Renato Ricci, Alessandro Proclemer, Gianfranco Sinagra, and Giuseppe Boriani. Seventeen-year trend (2001–2017) in pacemaker and implantable cardioverter-defibrillator utilization based on hospital discharge database data: An analysis by age groups. *European Journal of Internal Medicine*, 84:38–45, 2021.
- [64] Zachary A. Mosher, Jeffrey R. Sawyer, and Derek M. Kelly. MRI safety with orthopedic implants. *Orthopedic Clinics of North America*, 49:455–463, 2018.
- [65] Jorg Spiegel, Gerhard Fuss, Martin Backens, Wolfgang Reith, Tim Magnus, Georg Becker, Jean-Richard Moringlane, and Ulrich Dillmann. Transient dystonia following magnetic resonance imaging in a patient with deep brain stimulation electrodes for the treatment of parkinson disease. *Journal of Neurosurgery*, 99(4):772 – 774, 2003.
- [66] C. P. Naehle, H. Litt, T. Lewalter, and T. Sommer. Do we need pacemakers resistant to magnetic resonance imaging? *EP Europace*, 8(5):388–388, 05 2006.
- [67] N. J. Ferris, H Kavnoudias, C Thiel, and S Stuckey. The 2005 australian MRI safety survey. *American Journal of Roentgenology*, 188:1388–1394, 2007.
- [68] J. G. Nutt, V. C. Anderson, J. H. Peacock, J. P. Hammerstad, and K. J. Burchiel. DBS and diathermy interaction induces severe CNS damage. *Neurology*, 56(10):1384–1386, 2001.
- [69] U.S. food and drug administration. Benefits and risks. <https://www.fda.gov/radiation-emitting-products/MRI-magnetic-resonance-imaging/benefits-and-risks>. Accessed: 2021-05-3.

- [70] Jeroen H. F. Van Gemert, Wyger Brink, Andrew Webb, and Rob F. Remis. An efficient methodology for the analysis of dielectric shimming materials in magnetic resonance imaging. *IEEE transactions on medical imaging*, 36(2):666–673, 2016.
- [71] Peter R. S. Stijnman, Janot P. Tokaya, Jeroen van Gemert, Peter R. Luijten, Josien P. W. Pluim, Wyger M. Brink, Rob F. Remis, Cornelis A. T. van den Berg, and Alexander J. E. Raaijmakers. Accelerating implant RF safety assessment using a low-rank inverse update method. *Magnetic Resonance in Medicine*, 83(5):1796–1809, 2020.
- [72] M. Kruglyakov and A. Kuvshinov. Using high-order polynomial basis in 3-D EM forward modeling based on volume integral equation method. *Geophysical Journal International*, 213(2):1387–1401, 02 2018.
- [73] S.N. Shabunin and V.A. Chechetkin. Green’s functions application for computer modeling in electromagnetics. 2274:62–74, 2018.
- [74] G. Gabriadze, G. Chiqovani, E. Yavolovskaya, L. Svanidze, D. Karkashadze, and R. Jobava. Novel VIE solution for low frequency EM fields induced inside human body voxel models. In *2017 International Symposium on Electromagnetic Compatibility - EMC EUROPE*, pages 1–6, 2017.
- [75] Shao Ying Huang, Zu-Hui Ma, Luo Wan, Wenwei Yu, and J Thomas Vaughan. Fast full-wave calculation of electromagnetic fields based on weak-form volume integral equation for MRI applications. *The Journal of Engineering*, 2018(9):762–767, 2018.
- [76] Jeff Bezanson, Alan Edelman, Stefan Karpinski, and Viral B Shah. Julia: A fresh approach to numerical computing. *SIAM review*, 59(1):65–98, 2017.
- [77] Tim Besard, Christophe Foket, and Bjorn De Sutter. Effective extensible programming: Unleashing Julia on GPUs. *IEEE Transactions on Parallel and Distributed Systems*, 2018.
- [78] Anandhan Dhanasingh and Claude Jolly. An overview of cochlear implant electrode array designs. *Hearing Research*, 356:93–103, 2017.
- [79] Thomas Lenarz. Cochlear implant - state of the art. *GMS Curr Top Otorhinolaryngol Head Neck Surg*, 16:Doc04, 2018.
- [80] F.G. Shellock and A. Spinazzi. MRI safety update 2008: part 2, screening patients for MRI. *American Journal of Roentgenology*, 191(4):1140–1149, 2008.

-
- [81] L. Golestanirad, E. Kazemivalipour, D. Lampman, H. Habara, E. Atalar, J. Rosenow, J. Pilitsis, and J. Kirsch. RF heating of deep brain stimulation implants in open-bore vertical MRI systems: A simulation study with realistic device configurations. *Magnetic resonance in medicine*, 83(6):2284–2292, 2020.
- [82] P.R.S. Stijnman, B.R. Steensma, C.A.T. van den Berg, and A.J.E Raaijmakers. A perturbation approach for ultrafast calculation of RF field enhancements near medical implants in MRI. *Nature scientific reports*, (0):0–0, 2021.
- [83] A. Christ, W. Kainz, E.G. Hahn, K. Honegger, M. Zefferer, E. Neufeld, W. Rascher, R. Janka, W. Bautz, and J. Chen. The virtual family—development of surface-based anatomical models of two adults and two children for dosimetric simulations. *Physics in Medicine & Biology*, 55(2):N23, 2009.
- [84] S.A. Taghanaki, K. Abhishek, J.P. Cohen, J. Cohen-Adad, and G. Hamarneh. Deep semantic segmentation of natural and medical images: a review. *Artificial Intelligence Review*, 54(1):137–178, 2021.
- [85] T. Zhou, S. Ruan, and S. Canu. A review: Deep learning for medical image segmentation using multi-modality fusion. *Array*, 3:100004, 2019.
- [86] X. Zhou, K. Yamada, T. Kojima, R. Takayama, S. Wang, X. Zhou, T. Hara, and H. Fujita. Performance evaluation of 2D and 3D deep learning approaches for automatic segmentation of multiple organs on ct images. In *Medical Imaging 2018: Computer-Aided Diagnosis*, volume 10575, page 105752C. International Society for Optics and Photonics, 2018.
- [87] D. García-Lorenzo, S. Francis, S. Narayanan, D.L. Arnold, and D.L. Collins. Review of automatic segmentation methods of multiple sclerosis white matter lesions on conventional magnetic resonance imaging. *Medical image analysis*, 17(1):1–18, 2013.
- [88] M. Oberweger, M. Rad, and V. Lepetit. Making deep heatmaps robust to partial occlusions for 3D object pose estimation. In *Proceedings of the European Conference on Computer Vision (ECCV)*, pages 119–134, 2018.
- [89] C. Lin, C. Kong, and S. Lucey. Learning efficient point cloud generation for dense 3D object reconstruction. In *proceedings of the AAAI Conference on Artificial Intelligence*, volume 32, 2018.

- [90] Z. Qin, J. Wang, and Y. Lu. Monogrnet: A geometric reasoning network for monocular 3D object localization. In *Proceedings of the AAAI Conference on Artificial Intelligence*, volume 33, pages 8851–8858, 2019.
- [91] W. Wang and G.G. Grinstein. A survey of 3D solid reconstruction from 2D projection line drawings. In *Computer Graphics Forum*, volume 12, pages 137–158. Wiley Online Library, 1993.
- [92] Katscher U and van den Berg C. Electric properties tomography: Biochemical, physical and technical background, evaluation and clinical applications. *NMR Biomed*, 30(8):e3729, 2017.
- [93] Holder D. *Electrical Impedance Tomography: Methods, History and Applications*, volume 32. 2005.
- [94] Kim SY, Shin J, and Kim DH et al. Correlation between electrical conductivity and apparent diffusion coefficient in breast cancer: effect of necrosis on magnetic resonance imaging. *EUR Radiol*, 28(8):3204–3214, 2018.
- [95] Shin J, Kim MJ, and Lee J et al. Initial study on in vivo conductivity mapping of breast cancer using MRI. *J Magn Reson Im*, 42(2):371–378, 2015.
- [96] Kim SY, Shin J, and Kim DH et al. Correlation between conductivity and prognostic factors in invasive breast cancer using magnetic resonance electric properties tomography (MREPT). *EUR Radiol*, 26(7):2317–2326, 2016.
- [97] Tha KK, Katscher U, and Yamaguchi S et al. Noninvasive electrical conductivity measurement by MRI: a test of its validity and the electrical conductivity characteristics of glioma. *EUR Radiol*, 28(1):348–355, 2018.
- [98] van Lier A, van der Kolk A, and Brundel M et al. Electrical conductivity in ischemic stroke at 7.0 Tesla: A case study. proceedings ISMRM 2012. page 3484, 2012.
- [99] Jensen-Kondering U, Böhm R, and Shu L et al. Electric properties tomography in a rodent model of ischemic stroke: Results of a combined ex-vivo and in-vivo pilot study. proceedings ISMRM 2017. page 4627, 2017.
- [100] Carluccio G, Bruno M, and Collins C. Predicting long-term temperature increase for time-dependent SAR levels with a single short-term temperature response. *Magn Reson Med*, 75(5):2195–2203, 2016.

-
- [101] Balidemaj E, Kok H, and Schooneveldt G et al. Hyperthermia treatment planning for cervical cancer patients based on electrical conductivity tissue properties acquired in vivo with ept at 3 T MRI. *Int J Hyperther*, 32(5):558–568, 2016.
- [102] Homann H. *SAR prediction and SAR management for parallel transmit MRI*, volume 16. KIT Scientific Publishing, 2012.
- [103] Martin R, Vazquez J, and Marrufo O et al. SAR of a birdcage coil with variable number of rungs at 300 mhz. *Measurement*, 82:482–489, 2016.
- [104] Katscher U, Findekle C, and Vernickel P et al. Determination of Electric Conductivity and Local SAR Via B1 Mapping. *IEEE T Med Imaging*, 28(9):1365–1374, 2009.
- [105] Lee J, Shin J, and Kim DH. MR-based conductivity imaging using multiple receiver coils. *Magn Reson Med*, 76(2):530–539, 2016.
- [106] Van Lier A, Raaijmakers A, and Voigt T et al. Electrical properties tomography in the human brain at 1.5, 3, and 7T: A comparison study. *Magn Reson Med*, 71(1):354–363, 2014.
- [107] Lee S, Bulumulla S, and Wiesinger F et al. Tissue electrical property mapping from zero echo-time magnetic resonance imaging. *IEEE T Med Imaging*, 34(2):541–550, 2015.
- [108] Marques J, Sodickson D, and Ipek O et al. Single acquisition electrical property mapping based on relative coil sensitivities: A proof-of-concept demonstration. *Magn Reson Med*, 74(1):185–195, 2015.
- [109] Mandija S, Sbrizzi A, and Katscher U et al. Error analysis of Helmholtz-based MR-electrical properties tomography. *Magn Reson Med*, 80(1):90–100, 2018.
- [110] Lee SK, Bulumulla S, and Hancu I. Theoretical Investigation of Random Noise-Limited Signal-to-Noise Ratio in MR-Based Electrical Properties Tomography. *IEEE T Med Imaging*, 34(11):2220–2232, 2015.
- [111] Liu J, Zhang X, Schmitter S, Van de Moortele P, and He B. Gradient-based electrical properties tomography (gEPT): A robust method for mapping electrical properties of biological tissues in vivo using magnetic resonance imaging. *Magn Reson Med*, 74(3):634–646, 2015.
- [112] Yildiz G and Ider YZ. Use of dielectric padding to eliminate low convective field artifact in cr-MREPT conductivity images. *Magn Reson Med*, 81(5):3168–3184, 2019.

- [113] Balidemaj E, Van Den Berg C, and Trinks J et al. CSI-EPT: A Contrast Source Inversion Approach for Improved MRI-Based Electric Properties Tomography. *IEEE T Med Imaging*, 34(9):1788–1796, 2015.
- [114] Hong R, Li S, and Zhang J et al. 3-d MRI-based electrical properties tomography using the volume integral equation method. *IEEE T Microw Theory*, 65(12):4802–4811, 2017.
- [115] Abubaker A and van den Berg P. Total variation as a multiplicative constraint for solving inverse problems. *IEEE T Image Process*, 10(9):1384–1392, 2001.
- [116] Liu J, Wang Y, and Katscher U et al. Electrical properties tomography based on b_1 maps in MRI: Principles, applications, and challenges. *IEEE T Bio-Med Eng*, 64(11):2515–2530, 2017.
- [117] Li L, Zheng H, and Li F. Two-dimensional contrast source inversion method with phaseless data: TM case. *IEEE T Geosci Remote*, 47(6):1719–1736, 2009.
- [118] Arduino A, Bottauscio O, and Chiampi M et al. Magnetic resonance-based imaging of human electric properties with phaseless contrast source inversion. *Inverse Probl*, 34, 2018.
- [119] Van Lier A, Brunner D, and Pruessmann K et al. B1+ phase mapping at 7 T and its application for in vivo electrical conductivity mapping. *Magn Reson Med*, 67(2):552–561, 2012.
- [120] Nocedal J and Wright S. *Numerical optimization*. Springer Science & Business Media, 2006.
- [121] Chong E and Zak S. *An introduction to optimization*. John Wiley & Sons, 2013.
- [122] Arduino A, Zilberti L, and Chiampi M et al. CSI-EPT in presence of RF-shield for MR-coils. *IEEE T Med Imaging*, 2017.
- [123] Jin J. *Electromagnetic Analysis and Design in Magnetic Resonance Imaging*. Biomedical Engineering. Taylor & Francis, 1998.
- [124] Collins C and Smith M. Signal-to-noise ratio and absorbed power as functions of main magnetic field strength, and definition of “90°” RF pulse for the head in the birdcage coil. *Magn Reson Med*, 45(4):684–691, 2001.
- [125] Haacke E, Petropoulost L, and Nilges E et al. Extraction of conductivity and permittivity using magnetic resonance imaging. *Phys Med Biol*, 36(6):723–734, 1991.

- [126] Stogryn A. Equations for calculating the dielectric constant of saline water (correspondence). *IEEE T Microw Theory*, 19(8):733–736, 1971.
- [127] Yarnykh V. Actual flip-angle imaging in the pulsed steady state: A method for rapid three-dimensional mapping of the transmitted radiofrequency field. *Magn Reson Med*, 57(1):192–200, 2007.
- [128] Prisco M and Mansi L. Gary liney (ed): MRI from a to z: a definitive guide for medical professionals. *Eur J Nucl Med Mol I*, 40:C38, 2013.
- [129] Griffiths DJ. *Introduction to electrodynamics*. Pearson, third edition, 2008.
- [130] Brink W, Remis R, and Webb A. A theoretical approach based on electromagnetic scattering for analysing dielectric shimming in high-field MRI. *Magn Reson Med*, 75(5):2185–2194, 2016.
- [131] Leijssen R, Fuchs P, and Brink W et al. Developments in electrical-property tomography based on the contrast-source inversion method. *J Imaging*, 5:25, 2019.
- [132] Leijssen R, Brink W, and van den Berg C et al. Three-dimensional contrast source inversion-electrical properties tomography: 3D CSI-EPT. *IEEE T Med Imaging*, 37(9):2080–2089, 2018.
- [133] Leijssen R, van den Berg C, and Webb A et al. Combining deep learning and 3D contrast source inversion in MR-based electrical properties tomography. *NMR Biomed*, page e4211, 2019.
- [134] S. Wolf, D. Diehl, M. Gebhardt, J. Mallow, and O. Speck. SAR simulations for high-field MRI: How much detail, effort, and accuracy is needed? *Magnetic Resonance in Medicine*, 69(4):1157–1168, 2013.
- [135] T.M. Fiedler, M.E. Ladd, and A.K. Bitz. SAR simulations & safety. *NeuroImage*, 168:33–58, 2018. Neuroimaging with Ultra-high Field MRI: Present and Future.
- [136] R Leijssen, W Brink, C van den Berg, A Webb, and R Remis. Electrical properties tomography: A methodological review. *Diagnostics*, 11(2), 2021.
- [137] A. Hauptmann et al. Model-based learning for accelerated, limited-view 3-d photoacoustic tomography. *IEEE Transactions on Medical Imaging*, 37(6):1382–1393, June 2018.
- [138] Jonas Adler et al. Solving ill-posed inverse problems using iterative deep neural networks. *Inverse Problems*, 33(12):124007, nov 2017.

-
- [139] Marcin Andrychowicz et al. Learning to learn by gradient descent by gradient descent. *arXiv*, 2016.
- [140] S Mandija, E.F. Meliado, N.R.F. Huttinga, P.R. Luijten, and C.A.T. van den Ber. Opening a new window on MR-based electrical properties tomography with deep learning. *Scientific Reports*, 9, 2019.
- [141] N Hampe, U Katscher, C.A.T. Van den Berg, K.K. Tha, and S. Mandija. Investigating the challenges and generalizability of deep learning brain conductivity mapping. *Physics in Medicine & Biology*, 65(13):135001, 2020.
- [142] R Leijssen, C van den Berg, A Webb, R Remis, and S Mandija. Combining deep learning and 3D contrast source inversion in MR-based electrical properties tomography. *NMR in Biomedicine*, page e4211, 2019.
- [143] A.J.G. Inda, S.Y. Huang, N. İmamoğlu, and W. Yu. Physics-coupled neural network magnetic resonance electrical property tomography (MREPT) for conductivity reconstruction. *arXiv preprint arXiv:2109.12873*, 2021.

List of Publications

9.1 Journal publications

1. Stijnman, PRS, Mandija, S, Fuchs, PS, van den Berg, CAT, Remis, RF. Transceive phase corrected 2D contrast source inversion-electrical properties tomography. *Magn Reson Med.* 2021; 85: 2856– 2868. doi: 10.1002/mrm.28619.
2. Stijnman, PRS, Tokaya, JP, van Gemert, J, Luijten, PR, Pluim, JMW, Brink, WM, Remis, RF, van den Berg, CAT, Raaijmakers, AJE. Accelerating implant RF safety assessment using a low-rank inverse update method. *Magn Reson Med.* 2020; 83: 1796– 1809. doi: 10.1002/mrm.28023.
3. Stijnman, PRS, Erturk, MA, van den Berg, CAT, Raaijmakers, AJE. A single setup approach for the MRI-based measurement and validation of the transfer function of elongated medical implants. *Magn Reson Med.* 2021; 86: 2751– 2765. doi: 10.1002/mrm.28840.
4. Stijnman, PRS, Steensma, BR, van den Berg, CAT, Raaijmakers, AJE. Perturbation Approach for Ultrafast Calculation of RF Field Enhancements near Medical Implants in MRI.
5. Stijnman, PRS, Steensma, BR, Melis, G, van den Berg, CAT, Raaijmakers, AJE. Workflow for Subject-Specific RF Safety Assessment of patients with Orthopedic Implants in MRI.
6. Fuchs, PS, Mandija, S, Stijnman, PRS, Brink, WM, van den Berg, CAT, Remis, RF. First-Order Induced Current Density Imaging and Electrical Properties Tomography in MRI, 4, 4, 624-631, *IEEE Trans on Comp Im* 2018, doi: 10.1109/TCL.2018.2873407.

9.2 Conference Proceedings

1. Stijnman, PRS, Tokaya, JP, van den Berg, CAT, Raaijmakers, AJE. The transfer function for implanted wires when a second wire is near. ISMRM.
2. Stijnman, PRS, Mandija, S, Fuchs, PS, van den Berg, CAT, Remis, RF. Transceive phase corrected contrast source inversion-electrical properties tomography. ISMRM.
3. Stijnman, PRS, Tokaya, JP, van den Berg, CAT, Raaijmakers, AJE. Alleviating Impact of Perfusion on RF induced Heating due to Artificial Cardiac Valves. ISMRM.
4. Stijnman, PRS, Tokaya, JP, van Gemert, J, Luijten, PR, Pluim, JMW, Brink, WM, Remis, RF, van den Berg, CAT, Raaijmakers, AJE. Efficient Methodology for Implant Safety Assessment. ISMRM.
5. Stijnman, PRS, Tokaya, JP, van den Berg, CAT, Raaijmakers, AJE. Phase Enhancement Factor. MRI safety conference Utrecht.
6. Stijnman, PRS, van den Berg, CAT, Raaijmakers, AJE. Learned Unrolled Optimization for Rapid Computation of Local RF field Enhancement Near Implants. ISMRM.
7. Tokaya, JP, Stijnman, PRS, Luijten, PR, van den Berg, CAT, Raaijmakers, AJE. Explaining current patterns on implantable medical devices during MRI using the transfer matrix. ISMRM
8. Stijnman, PRS, Steensma, BR, van den Berg, CAT, Raaijmakers, AJE. GPU accelerated calculations of the scattered RF-field due to a dielectric update without extensive pre-calculated data. ISMRM.
9. Stijnman, PRS, Steensma, BR, van den Berg, Melis, G, CAT, Raaijmakers, AJE. Workflow for Personalized RF Safety Assessment of Orthopedic Implants in MRI, a Proof of Concept. ISMRM.
10. Zumbo, S, Bevacqua, MT, Meliado, EF, Stijnman, PRS, Meerbothe, T, Isernia, T, van den Berg, CAT, Mandija, S. Unrolled iterative MR-Electrical Properties Tomography using physics-based deep learning. ISMRM.
11. Meerbothe, T, Florczak, S, Stijnman, PRS, van den Berg, CAT, Levato, R, Mandija, S. A semi-realistic and reusable 3D printed brain phantom for MR-based Electrical Properties Tomography. ISMRM.

Curriculum Vitae

Peter Ruben Sebastiaan was born on 18-02-1994 in Arnhem and grew up in Huissen. After finishing bilingual VWO in 2012 at "het Lorentz Lyceum" in Arnhem, he studied Microelectronics at the technical university of Delft in Delft, Netherlands. In 2017 he graduated within the Circuits & Systems group on electrical properties tomography in magnetic resonance imaging. From 2017 he started a PhD project at the Eindhoven University of Technology in Eindhoven, the Netherlands, in collaboration with the university medical center Utrecht of which the results are presented in this dissertation. Since 2022 he is employed at the university medical center Utrecht.

Dankwoord

Beargumenteerbaar het belangrijkste stuk tekst van dit proefschrift: het dankwoord. Voor alle mensen die er voor gezorgd hebben dat ik nu überhaupt dit kan schrijven. Om de spits af te bijten, als eerste wil ik Dr.ir. Alexander Raaijmakers en Prof.dr.ir. Cornelis van den Berg bedanken. Zonder jullie was er geen project geweest waar ik mij vier jaar lang op vast heb kunnen bijten. Nico, wij hadden al een proefjaar gedraaid met mijn master afstudeerproject, in die tijd leerde ik veel mensen kennen in het UMC en wilde ik graag langer blijven en dieper de onderzoekswereld induiken. Jouw kritische blik op het onderzoek en de kennis van het landschap eromheen hielpen enorm bij het goed wegzetten van de resultaten die we hebben behaald. Verder hielpen de spontane ideeën en jouw passie ook erg bij de motivatie over de jaren. Alexander, in de afgelopen 4 jaar van de kennismaking voor de onderzoekspositie tot de lange scansessies, het lesgeven in Eindhoven, en uiteindelijk het schrijven van dit proefschrift hebben we toch veel meegemaakt en bereikt. Jouw resultaat gerichte aanpak was goed om snel op een punt te komen waar we werkbare resultaten kregen. Daarna konden details gefinetuned worden en het onderzoek duidelijk gecommuniceerd worden met de rest van de MRI community. Zo kwam het bij de mensen die minder diep in de stof zaten toch nog goed over wat voor magie wij aan het beoefenen waren. Verder was er altijd een goede sfeer, of het nou met tentamens nakijken was of een biertje in the basket na de groepsmeeting. Ik heb van jullie beide veel mogen leren, maar hopelijk hebben jullie ook wat van mij opgestoken al is het maar dat jullie wat vaker op één lijn moeten zitten.

Prof.dr. Josien Pluim, bedankt dat ik in jouw afdeling mocht promoveren. Hoewel ik veel van mijn tijd in het UMC Utrecht doorbracht waren de momenten dat ik in Eindhoven was altijd leerzaam. Er werd weer vanuit een ander oogpunt naar mijn onderzoek gekeken. Verder bedankt voor alle feedback tijdens het traject en zeker ook bij het afronden ervan.

Ook wil ik mijn promotiecommissie bedanken; Prof.dr.ir Martijn van Beurden, Prof.dr. Andrew Webb, Prof.dr Bas Raaymakers, en Dr.ir Rob Remis. De feedback op het proefschrift is heel erg gewaardeerd en het is altijd leuk om mensen te vinden die de tijd willen nemen of hebben genomen om mijn onderzoek te lezen en daar over te discussiëren. In het bijzonder wil ik ook Rob Remis bedanken voor het aanwakkeren van mijn gevoel voor het onderzoek tijdens mijn master afstudeerproject.

Dan wil ik mijn collega's op hetzelfde project bedanken voor het bevorderen van elkaars onderzoek. Janot, toen ik op het project kwam was jij er als enige andere PhD-er ermee bezig. Je hebt me door de beginselen van het onderwerp heen geleid. Het was echt heel waardevol om dagelijks met jou te kunnen sparren, en hopelijk heb ik je niet teveel van het werk gehouden daarmee. Verder zien we elkaar gelukkig nog regelmatig met het (zaal)voetballen of met de "all-in". Mike, jij kwam nadat ik een klein jaartje bezig was ook op het project. Jou wil ik graag bedanken voor het altijd grondig uitzoeken hoe alles precies in elkaar zit en dat ook van andere te verwachten. Dat heeft er toegeleid dat ikzelf ook weer mijn behaalde resultaten tegen het licht ging houden om te zien waarom het precies werkte. Als laatste bij het project gekomen wil ik Bart bedanken. Voordat je bij het project kwam konden we al sparren tijdens de RF-meetings en toen je er bij kwam heb ik veel gehad aan je feedback op mijn manuscripten. Het was vooral ook handig om er een extra iemand bij te hebben om te sparren over de betekenis van resultaten en hoe die te visualiseren.

Daarna wil ik mijn overige mede-auteurs bedanken voor de fijne samenwerking, feedback, en sparringsessies; Jeroen, Peter, Wyger, Gerrit, Patrick, en Stefano. Zonder jullie inspanningen voor data verzameling, feedback, en uitleg was het niet gelukt om de resultaten te behalen die we nu hebben. Jullie kennis en enthousiasme heeft mij geholpen om nu hier te kunnen staan.

Verder de mensen die dagelijks met mijn waren opgescheept, mijn kamergenoten, Wieke, Lieke, Ria, Bernhard, Oscar, Tim, Arjan, Miha. Bedankt voor alle steun in de afgelopen paar jaar doormiddel van koffie, hulp bij debuggen, gezelligheid, potjes tafelfootbal, en de biertjes na het werk.

Dan de rest van de Q2-groep en de computational imaging-groep, letterlijk teveel mensen om op te noemen. Jullie zijn één van de redenen geweest dat ik bij het UMC wou beginnen. Door de goede sfeer die jullie creëerde ging ik met plezier naar het UMC. Met z'n alle in de lunchtrein, naar congressen, de switch-avondjes, en het vieren van iedereen's successen, zonder jullie was het een stuk minder leuk geweest. Gelukkig zit ik tegenwoordig maar één verdieping naar beneden en kunnen we hiermee gewoon doorgaan. In het speciaal wil ik nog Sylvia en Judith bedanken voor de organisatorische hulp, zonder jullie zou er weinig gebeuren op de afdeling.

Over tegenwoordig gesproken, wil ik graag mijn nieuw verkregen collega's,

Pim, Cornell, Alexis, Anette, Gijs, Maureen, en Bas bedanken voor de gezelligheid en de goede opvang in de afsluitende fase van mijn onderzoek. Ook bedank ik graag alle radiotherapie-zaalvoetballers voor de sportieve uitdagingen en de uitstekende derde helften.

De laatste twee mensen van werk die ik nog speciaal wil bedanken zijn mijn paranimfen, Niek en Sander. Bedankt dat jullie je tijdens deze speciale dag voor mij extra willen inzetten. Verder houden we de whisky-avondjes er gewoon in, waar we ook maar mogen werken of heen verhuizen.

Buiten het werk zijn er natuurlijk ook veel mensen die mij geholpen hebben om hier te komen. Deze wil ik uiteraard ook bedanken. Met als eerste de "Footfellas", elke dinsdag is het weer een spektakel op het veld en daarbuiten. Bedankt voor de afleiding en de sportieve uitdaging elke week.

Alex, Wendy, Danillo, Tu, Niels, en Wouther ik heb jullie leren kennen tijdens de studie en hoewel we druk mogen zijn met onze eigen dingen blijft het altijd goed om elkaar te zien en spreken. David, bedankt voor de dagelijkse chillings. De games en poolavondjes zijn slechts iets om te doen terwijl we elkaar kunnen bijpraten over hoe het gaat. Ik wacht in ieder geval met smart op het moment dat ik jouw boekje in mijn handen heb.

Dan de leukste (sinds kort) burens, Wessel en Marlies. Jullie ken ik nu ookal weer een aantal jaar en ik hoop dat daar nog veel jaren bij komen zeker nu we allemaal een goed stekkie hebben. Marlies bedankt voor de movienights en het hardlopen, beide zijn zeer effectief geweest om het hoofd te legen en weer helder te beginnen aan de volgende dag. Wessel bedankt voor alle discussies over de onderzoekswereld en een kijkje te geven in hoe het er in een ander vakgebied aan toegaat. Verder ook bedankt voor het gedeelde enthousiasme voor Julia en whisky.

Verder wil ik de "Party peeps", bedanken voor de steun door de jaren heen. Alle feestjes, borrels en weekendjes weg waren altijd een highlight van de week en een zeer welkome afleiding. We hebben misschien iets teveel meegemaakt in de afgelopen jaren, maar dat heeft wel een band geschept die niet velen hebben! Weet in ieder geval dat we op elkaar kunnen rekenen ookal kiest iedereen zijn eigen weg. In het speciaal wil ik nog Koen bedanken voor letterlijk alles. We kennen elkaar al sinds we een aantal maanden jong waren en ik denk dat dat meer zegt dan ik nu in woorden kan opschrijven.

Dan wil ik nog de bonus families de Mermansjes en van Dijkjes & Co bedanken voor het warme welkom, de gezellige feest- en verjaardagen. Jullie lieten het gelijk als thuis voelen.

Bijna klaar, Mam, Eva "klein" zusje, en Geert bedankt voor het zorgen voor mij. Ik denk dat zonder jullie hulp er weinig terecht was gekomen van dit avontuur. We zijn maar een klein clubje, maar dat maakt ons wel heel erg hecht! Meer ga ik niet schrijven want dan wordt het *te* waarschijnlijk.

Manouk, we kennen elkaar nu iets meer dan drie jaar en in die tijd is er veel

veranderd. Eerst heb jij je eigen appartement gescoord en sinds kort wonen we samen. Verder zijn we meerdere keren weekendjes weggegaan en op vakantie geweest, lekker relaxen in Malta of touren door Italië, het kan allemaal. Van 1 paper in mijn onderzoek tot het proefschrift dat nu is afgerond, jij zorgde er elke keer weer voor dat ik ook de tijd nam om de successen te vieren. Maar je was er niet alleen bij met de highlights, maar ook bij de dagelijkse struggles als het niet mee zat en de zware tijden in de afgelopen jaren. Weet dat ik daarom van je hou!

